TECHNICAL REPORT ON

"THE DETERMINATION OF RADIATION HARDNESS OF SEMICONDUCTOR MATERIALS AND DEVICES WITH ION BEAMS"

WHICH IS PART OF THE IAEA's COORDINATED RESEARCH PROJECT "F11016", ENTITLED

"UTILIZATION OF ION ACCELERATORS FOR STUDYING AND MODELLING OF RADIATION INDUCED DEFECTS IN SEMICONDUCTORS AND INSULATORS"

FOREWORD

Semiconductor materials in electronic devices are being used in harsh radiation environments in many fields of research and technology. The high-energy physics facilities, remote control systems in nuclear reactors, radiation therapy facilities and the aerospace sectors are being among the most significant areas where electronic devices are being exposed to increased levels of detrimental ionizing radiation.

The long-term operating performance, reliability and lifetime of these electronic materials and devices are strictly related to their resistance to various types and levels of ionizing radiation, which induce a progressive degradation of their performances. The evaluation of the material radiation hardness, i.e. the material resistance to accumulated damage caused by ionizing radiation, is a key requirement for an effective design of electronic devices. Therefore, the development of reliable and widely applicable test methodologies [ASTM2006] suitable for the determination of the radiation hardness (measure of non-vulnerability or of the resistance to accumulated level of radiation damage in variety of experimental conditions) is required to facilitate the optimal design of materials for the design of electronic devices.

Ion accelerator based techniques provide unique tools to gain insight into the phenomena underlying the formation of defects induced by energetic particles in semiconductor materials and their effects on the electronic features of the device.

In recognition of the potential of these techniques, with the aim of enhancing the understanding of the mechanisms underlying the degradation of the performances of semiconductor devices induced by ionizing radiation, the IAEA established a Research Project, coordinated by the Physics Section (CRP F11016) entitled "Utilization of ion accelerators for studying and modelling of radiation induced defects in semiconductors and insulators" at the end of 2011.

The objective of this IAEA Coordinated Research Project (CRP) was to enhance the capabilities of the interested Member States by facilitating their collective efforts to use accelerator-based ion irradiation of electronic materials in conjunction with available advanced characterization techniques to gain a deeper understanding of how different types of radiation influences the electronic properties of materials and devices, leading to an improved radiation hardness.

A dynamic and productive research was stimulated by this CRP among collaborating partners, resulting in publications in scientific journals [CRP2016], educational and scientific software packages [W8, Forneris2014], and a number of collaborations among the participating research groups.

Two of the most significant outcomes of this project are i) the experimental protocol, which rationalizes the use of the many existing characterization techniques adopted to investigate radiation effects in semiconductor devices and ii) the relevant theoretical approach to interpret the experimental data [Vittone2016 and references therein].

This publication integrates output of research articles published by the partners of the CRP and is aimed to provide an exhaustive description of the experimental protocol, the theoretical model with the relevant limits of application, the data analysis procedure, and the physical observables which can be effectively measured and which can be used for assessment of the radiation hardness of semiconductor devices.

Ettore Vittone, Torino 4 August 2017   2

The intended audience of this report includes all those professionals and technologists working in ion beam functional analysis of semiconductor materials, solid-state physicists and engineers involved in the design of electronic devices working in radiation harsh environments.
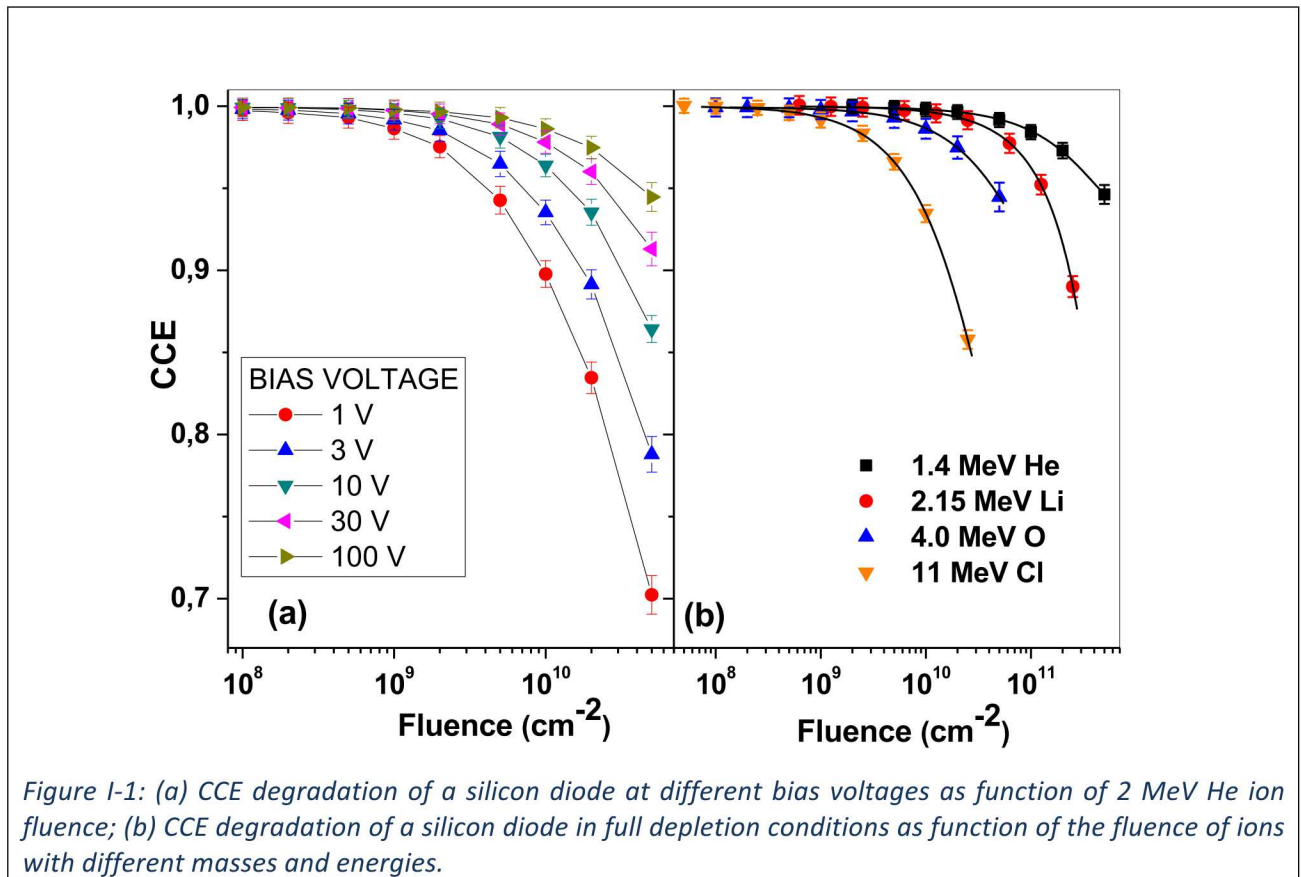
CONTENTS

I. INTRODUCTION

The useful lifetime of semiconductor electronic devices working in harsh radiation environments is limited by the structural defects induced by the exposure to ionizing radiation, whose long-term accumulation can lead to a significant degradation of their electronic performances. A deep understanding of what types of defects are formed and what are their effects on the electronic properties is therefore of paramount importance for the development of new devices with improved radiation hardness.

Intensive studies have been carried out in different industrial contexts and international scientific collaborations [Schwank2013, Moll2013, W9]. However, these tests are often tailored to specific problems (e.g. the certification procedure of devices for space applications) and it is hard to generalize the results to different devices and/or to different irradiation conditions. Several studies showed that the effects of different radiations could be correlated to the Non Ionizing Energy Loss (NIEL) value [Messenger1999, 2005], which has been found useful for characterizing displacement damage effects in electronic materials. However, the NIEL approach takes into account the creation of structural defects (vacancies), but does not consider their effects on the transport properties in semiconductor, whereas, the degradation of the overall performance depends both on the amount of the radiation damage and on the device operative conditions.

Figure I-1: (a) CCE degradation of a silicon diode at different bias voltages as function of 2 MeV He ion fluence; (b) CCE degradation of a silicon diode in full depletion conditions as function of the fluence of ions with different masses and energies.

As an example [Pastuovic2011, 2013], Fig. 1 shows the charge collection efficiency (CCE) degradation of silicon photodiodes irradiated with different ions in full depletion regime (b) and at different bias conditions (a). It is apparent that the CCE depends on both the mass and energy of the ions and on the damage profile generated along the ion tracks, with respect to the active region extension as determined by the applied bias voltage.

It is therefore desirable to develop the standardized procedure to quantify the radiation hardness of semiconductor devices in general.

This need has been recently recognized by the International Atomic Energy Agency (IAEA), which has promoted a Coordinated Research Project (CRP F11016; 2011-2016) entitled "Utilization of ion accelerators for studying and modelling of radiation induced defects in semiconductors and insulators", which involved 14 institutions from 13 countries worldwide.

The project provided significant contributions in enhancing the capabilities of techniques based on the use of energetic (MeV) ions, both as damaging agents and as probes of the radiation damage, and to elucidate the mechanisms underlying the radiation-induced degradation of the electronic performances of semiconductor devices.

The focus of the research activity was the development of an experimental protocol for a comprehensive characterization of the effects of radiation damage and an optimized theoretical approach to model the effects of radiation-induced defects on the electronic properties of semiconductors.

The experimental protocol emerged from this CRP is the development of a methodology proposed by A. Simon et al. [Simon2005] and Z. Pastuovic et al. [Pastuovic2009, 2011] and further refined both from the experimental and theoretical aspects.

The experimental methodology is based on the Ion Beam Induced Charge (IBIC) technique [Breese2007], in which the charge induced by the motion of carriers generated by each ion within a rarefied (a few thousand ions per second) focused ion beam is detected. This technique is well-suited here, as the same experimental geometry, and frequently the same ions, are used both to damage the material under investigation and also to detect the effects of damage by the reduced charge pulse height produced by each subsequent ion. Moreover, the analytical potential of this experimental methodology is further enhanced by the possibility of measuring the Charge Collection Efficiency (CCE) degradation in different polarization conditions of the device under study. Another advantage offered by the use of IBIC as the basic characterization technique is given by the availability of a robust theoretical formalism, based on the fundamentals of electrostatics, for the modelling of IBIC experiments. The refined model developed during the CRP integrates the ionization and non-ionization ion energy loss in solids [Ziegler2010], the theory of charge induction in semiconductors [Vittone2008, Vizkelethy2011] and the electron/hole generation-recombination model of Shockley–Read–Hall [Shockley1952] to fully exploit the wealth of information contained in the combination of the CCE degradation curves obtained in different experimental conditions.

The effectiveness of the protocol was assessed and the interpretative model was validated through different types of ion beam irradiations and characterizations. These experiments were performed on silicon as a reference semiconducting material [Pastuovic2013, Vizkelethy2013, Vittone2016]. Later the methodology proven on silicon diodes was successfully applied to study radiation effects on other materials of high technological interest and with the potential of high radiation tolerance, as silicon carbide [Pastuovic2015, Lopez2016] and diamond [Grilj2016]. The introduction to the methodology and some of the key results were published in a special issue of the journal "Nuclear Instruments and Methods in Physics Research B", [CRP2016].

This document integrates the information contained in previous articles and intends to provide an exhaustive description of an experiment implementing the experimental, theoretical and data analysis methodologies resulting from the CRP, to analyse commercially available silicon photodiodes. This case of study was chosen because this silicon device is commonly used as a nuclear detector in IBA experiments. These type of experiments for the studies of radiation damage in semiconductor materials and the assessment of the radiation hardness of materials can be easily implemented in any ion microbeam laboratory equipped with standard instrumentation for ionizing radiation detection.

This report should then be regarded as a guidance document to measure key parameters, which are indicators of the radiation hardness of a semiconductor material.

II.   AN OVERVIEW OF THE EXPERIMENTAL PROCEDURE.

II.i   Features of the sample under study

In the following, we will apply the protocol for evaluation of the radiation hardness of a commercial silicon photo-diode, Hamamatsu S1223 (in the following indicated as DUS1) commonly used in IBA laboratories [Simon2005, Spemann2011]; its main features are described in the datasheet of the supplier [W1]. Figure II-1 shows optical images of DUS1. The TO-5 package allows a comfortable housing in standard sample holders. The metal can package has to be opened by gently sawing or grinding away the can top [Breese1996a] and to remove the borosilicate glass window on top in order to expose the frontal surface of the photodiode to incident MeV ions. Since the photodiode is a photon-sensitive, it was essential to perform all the measurements in dark conditions to avoid the contribution of the photocurrent to the electronic noise.
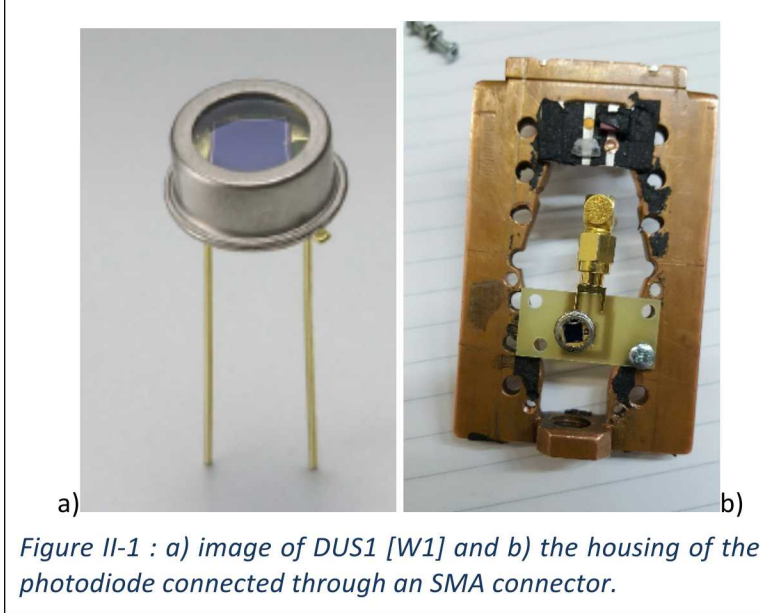

a)   b)

Figure II-1 : a) image of DUS1 [W1] and b) the housing of the photodiode connected through an SMA connector.

A second type of diodes (DUS2) will be occasionally considered in this report. They refer to n-type FZ silicon detectors developed at the Helsinki Institute of Physics and described in [Vittone2016].

II.i.a   Electronic characterization

In order to perform IBIC measurements, a charge sensitive preamplifier is commonly used, whose voltage output is proportional to the induced charge. However, before the connection of the DUS to the nuclear electronic chain, it is a good practice to evaluate the maximum reverse bias voltage, under which the leakage current can still be considered a negligible source of noise, which can significantly degrade the IBIC spectral resolution [Knoll2010]. As a rule of thumb, for a commercial charge sensitive preamplifier, it should not be larger than fractions of microampere. In case of DUS1, the leakage current is maintained below 100 nA at a reverse bias voltage of 100 V. It is worth noticing that the large bias protection resistor R_L (of the order of $10^8\,\Omega$) can lead to a substantial dc voltage drop across R_L. Consequently, the voltage actually applied to the detector is less than the supply voltage. For this case of study, at 100 V, a leakage current of 100 nA, the voltage bias applied to the detector is 90 V.

Similar remarks can be extended also to the measurement of the capacitance: the high value of C, occurring mainly at low reverse bias voltages, can significantly contribute to limit the spectral resolution of the detector. Capacitance can also influence the gain of the electronic chain; however, the high open loop gain of the preamplifier (typically 10^4) renders the effective gain insensitive to changes of the sample capacitance [Breese1996a].

Furthermore, the capacitance-voltage (C-V) characterization is the commonly used technique to evaluate the doping profile of the diode. The doping profile is used in the protocol to provide input information for calculation of the electrostatics of the diode and, accordingly, for evaluation of the charge carrier transport (mobility) parameters. The capacitance voltage (C-V) technique relies on the fact that the width of a reverse-biased space-charge region of a semiconductor junction device depends on the applied voltage [Schroder1990]. Assuming a diode with plane parallel electrodes and a one side p-n abrupt junction, the expression with relates the donor profile in the n-type region to the extension of the depletion region (w) is given by:

$$(1) \quad N_D(w) = \frac{2}{q \cdot \epsilon \cdot A^2 \cdot \frac{d\left(\frac{1}{C^2}\right)}{dV}}$$

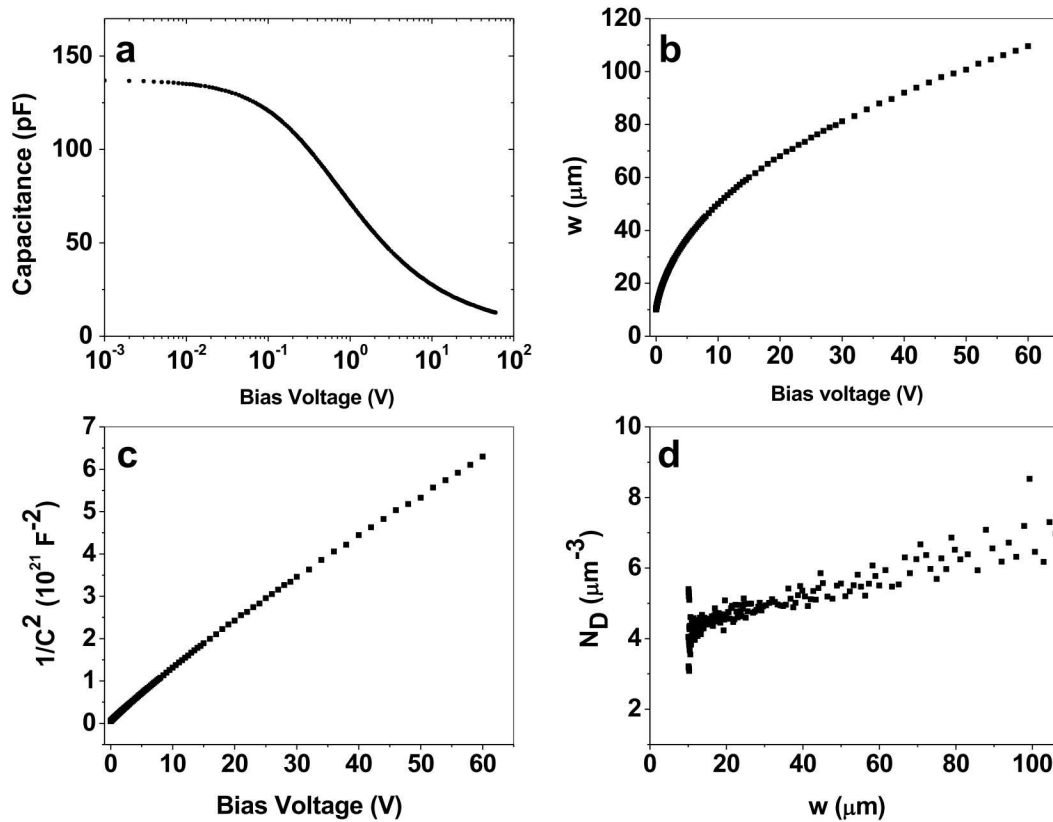Where

$$(2) \quad w = \frac{\epsilon \cdot A}{C}$$

Figure II-2 : a) Capacitance-voltage curve of DUS1 ; b) depletion layer extension vs. bias voltage calculated from eq. (2); c) 1/C² vs. bias voltage; d) doping profile calculated from eq. (1), assuming an electrode area of 13.8 mm². The origin of the horizontal axis corresponds to the position of the junction (courtesy of Z. Pastuovic).

SR-CV-PIB-DIB.opj[CV]gCV

According to eq. (1) it is very important that the area of the active region of the device (A) is precisely measured for the accurate calculation of the doping profile. The adopted procedure for the calculation of the doping profile in the n-type region of DUS1 through eqs. (1) and (2) is shown step by step in Figures II-2a-d.

It is worth noticing that both the electrical characterization and IBIC measurements were carried out at room temperature.
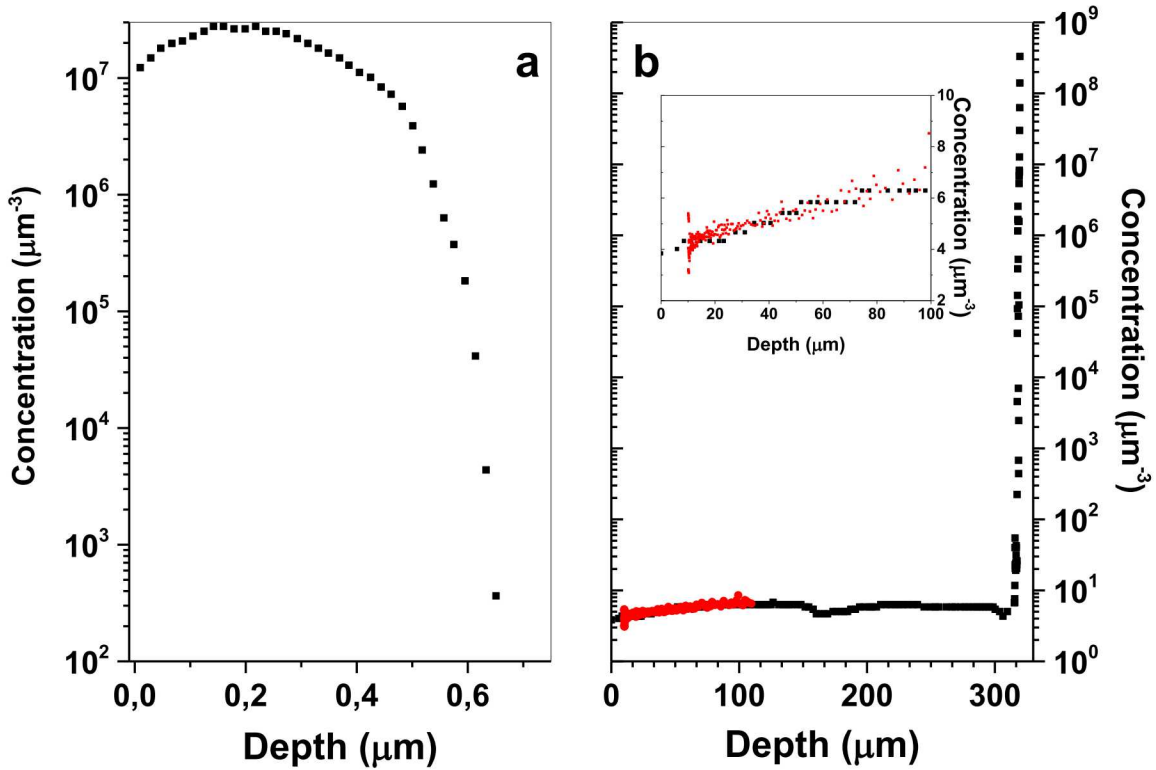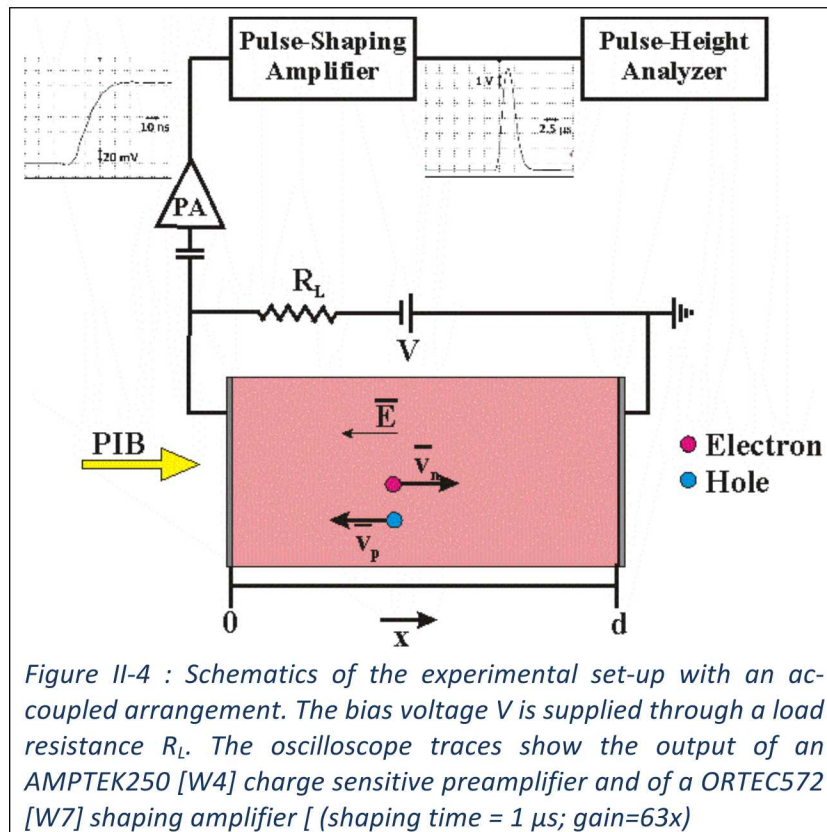

Figure II-3 : a) acceptor and b) donor concentration profile of DUS1 from SR measurement (courtesy of G. Vizkelethy). In the inset a comparison between the donor doping profile evaluated by SR (black markers) and C-V (red markers), assuming an effective electrode area of 13.8 mm².

SR-CV-PIB-DIB.opj[SR]gNP

An alternative method to evaluate the doping profile is the spreading resistance (SR) technique [Schroder1990]. Unlike the C-V technique, the spreading resistance is a destructive technique in sense that a sample is destroyed after the measurement. Moreover, the conversion of the measured spreading resistance data to the doping concentration profile depends very much on the algorithm. However, it provides profiles of any combination of layers (in our case, of both the p- and n- type regions) with very high resolution and no depth limitation. The spreading resistance measurements are commercially available and can be used to verify the profiles emerging from the C-V characterization. Figure II-3 shows the doping profiles of the two regions evaluated by the SR technique. The SR profile in the n-type region corresponds to the donor concentration profile evaluated by SR, if an effective area of 13.8 mm² is assumed.

II.ii   Assembly and electronics

The ion induced charge pulses are measured using standard electronics for charge particle detection, similar to those used for other IBA technique as RBS or NRA. Each pulse is fed to a low noise charge sensitive preamplifier, which integrates the induc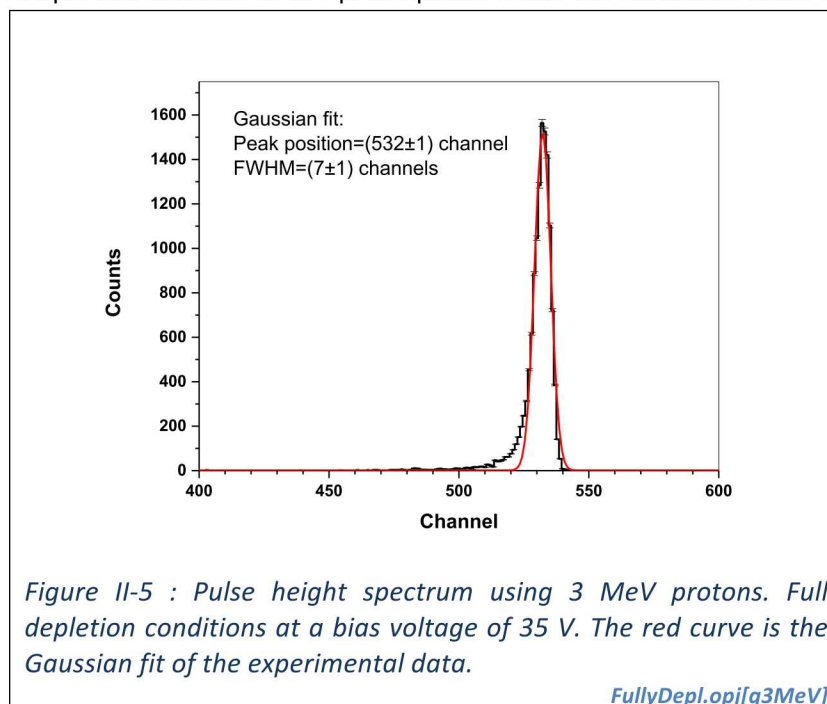ed charge on a feedback capacitor. Details on the principles of operation of the charge sensitive preamplifier can be found in many textbooks (e.g. [Knoll2010, Bertolini1968]) or instruction manuals from suppliers [W2, W3].

An ideal solution for the coupling of the preamplifier to the sample was adopted at the LIPSION laboratory [Jakob2011, Spemann2011], where a charge sensitive preamplifier [W4] is integrated into the sample holder and directly connected to the DUS. The electronic board is embedded in a metal box and shielded against electromagnetic radiation.

Figure II-4 : Schematics of the experimental set-up with an ac-coupled arrangement. The bias voltage V is supplied through a load resistance R_L. The oscilloscope traces show the output of an AMPTEK250 [W4] charge sensitive preamplifier and of a ORTEC572 [W7] shaping amplifier [(shaping time = 1 μs; gain=63x)

Coaxial cables are commonly used to couple the detector to the preamplifier. Since the electronic noise increases with the input capacitance, leads between the DUS and the preamplifier should be as short as possible. The sample should be isolated from earth loops, circulating currents and radio frequency pick-up from other electronic components of the experimental set-up [Breese1996a].

The small output pulses from the preamplifier are then fed into a shaping amplifier with shaping times typically of the order of 0.5 or 1 μs for the best signal/noise ratio. Finally, the pulses from the shaping amplifier are fed into the data acquisition system, which stores every event detected from the

Figure II-5 : Pulse height spectrum using 3 MeV protons. Full depletion conditions at a bias voltage of 35 V. The red curve is the Gaussian fit of the experimental data.

FullyDepl.opj[g3MeV]

sample, along with its spatial coordinate generating the so-called event-by-event (or occasionally list) files [Breese1996a].

Figure II-4 shows a scheme of the experimental set-up [Vittone2016]: ions hit the frontal electrode and generate by ionization electron/hole pairs, whose drift induce an electrical current, which is integrated by the charge sensitive preamplifier. The scheme can represent a p-n junction, where the cathode is located at x=0 and the anode located at x=d is grounded.

A typical charge pulse height spectrum measured for detection of mono-energetic ions (within the energy resolution limits of accelerating system) using the IBIC experimental set-up (Fig. II-4) is shown in Figure II-5. The peak position is usually evaluated through a Gaussian fit of the experimental data. More elaborated algorithms can be found in literature (e.g. [Pommé2015]) to fit the full shape of the peak, but they do not bring any further information for the purpose of this work.

In order to calibrate the electronic chain, it is important to define the full depletion conditions. This evaluation can be effectively carried out by plotting the peak posit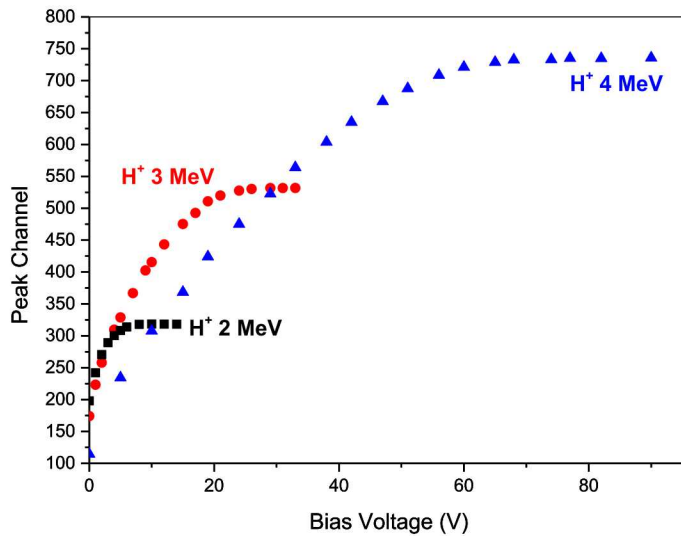ion as function of the applied bias voltage, as shown in Figure II-6. In this case, the saturation of the signals indicates that the carrier generation occurs entirely within the depletion region.

Figure II-6 : Peak position vs. applied bias voltage using protons at different energies.

ChvsV.opj

Energy=(0.466±0.04)+(4.80±0.07)*Channel
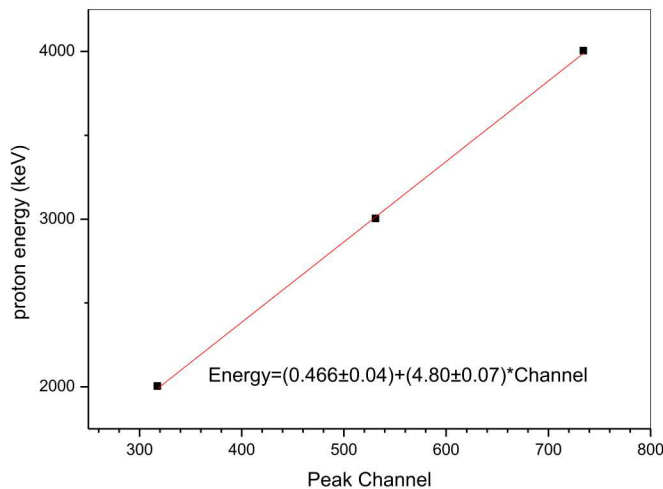
Figure II-7: Energy calibration of the electronic chain.

EnergyPeakPosition.ogg

In saturation conditions, the slope of the linear fit of the peak position as function of the ion energy is (4.80±0.07) keV/channel. The charge sensitivity is (1330±20) electrons/channel and was evaluated assuming the

total collection efficiency (100%) and an average energy to create and electron/hole pair in silicon of 3.6 eV [Martini1965].

Finally, the FWHM of the peak in Figure II-5 is 7 channels, and, from the previous calibration, it corresponds to (33.6±0.4) keV in silicon, i.e. a spectral resolution of 9300 electrons

II.iii   Effective Entrance Window or Dead layer thickness measurement

The effective entrance window (or dead layer) thickness can be evaluated by the angle resolved IBIC analysis [Knoll2010, LoGiudice2005, 2006]. In full depletion conditions, and using weakly penetrating ions, the diode response at different angle of incidence θ decreases due to the increase in ion path length in the dead layer. The energy loss of the incident ion in the active region, is given by the following equation

$$(3) \quad E(\theta) = E_0 - \frac{dE}{dx}\bigg|_0 \frac{t}{\cos(\theta)}$$

Where E_0 is the energy of the incident ion and $\frac{dE}{dx}\big|_0$ is the energy loss at the surface. In full depletion conditions, assuming that all the carriers generated in the depletion region induce a charge, which is totally collected and measured, the difference of the measured pulse height $Q(\theta)$ for angle of incidence θ and for angle 0 (Q_0), normalized to Q_0 is given by:

$$(4) \quad \frac{\Delta Q(\theta)}{Q_0} = \frac{Q(\theta) - Q(\theta=0)}{Q(\theta=0)} = \frac{1}{E_0} \frac{dE}{dx}\bigg|_0 t \cdot \left(1 - \frac{1}{\cos(\theta)}\right)$$

Figure II-8: Scheme of the Angle-Resolved IBIC experiment to evaluate the entrance window thickness.
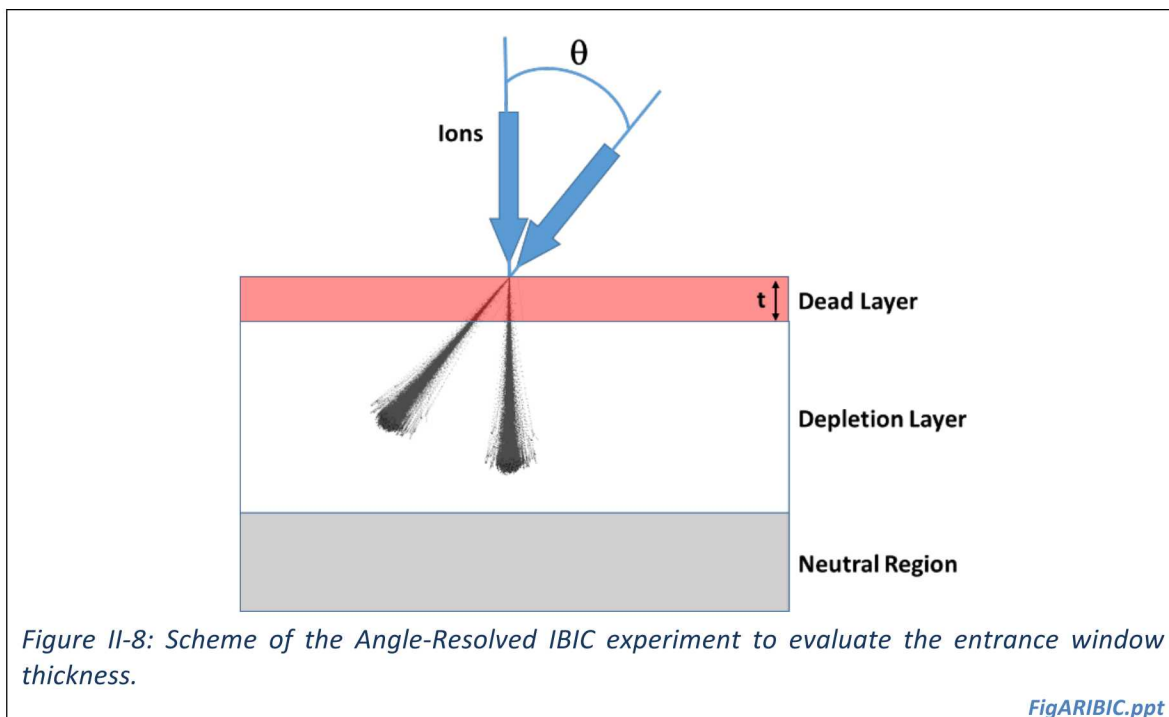
FigARIBIC.ppt

Figure II-8 shows a scheme of the experimental set-up. To evaluate the effective dead layer thickness of DUS1, 2.28 MeV Li ions were used and the sample was reverse biased at 20 V. Being the ion range of Li ions of 5.2 μm and the depletion layer width of about 60 μm, the full depletion conditions are effectively met.

Figure II-9: A): Peak channel vs. tilting angle. B): experimental data and linear fit by means of eq. (4).
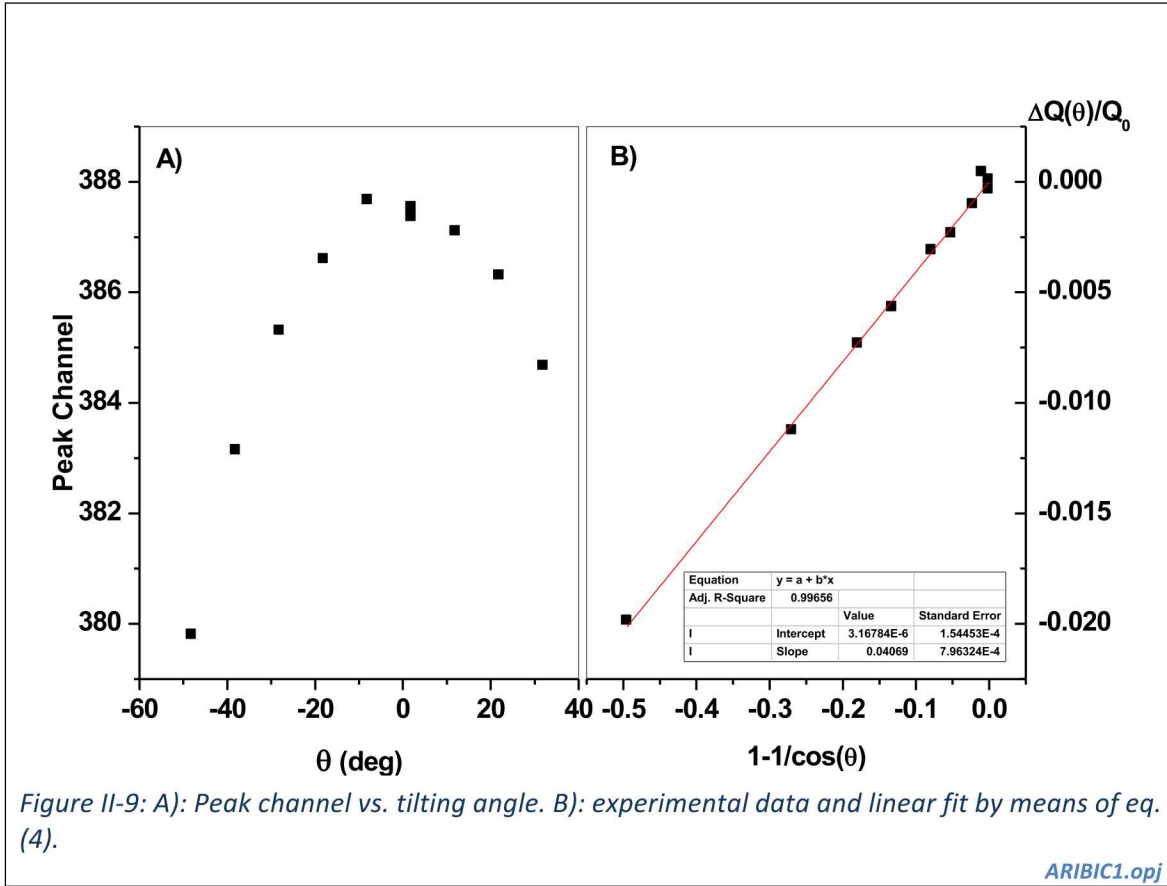
ARIBIC1.opj

Figure II-9A) shows the results of a series of IBIC measurements as the angle of incidence is varied; the same data reported as function of $\left(1 - \frac{1}{cos(\theta)}\right)$ is shown in Figure II-9B). From eq. (4), the slope of the linear fit (0.0407±0.0008) is equal to $\frac{1}{E_0}\frac{dE}{dx}\Big|_0 t$. From SRIM2013 simulation, the electronic stopping power of 2.28 MeV Li ions in silicon is $\frac{dE}{dx}\Big|_0 = 513 \; eV/nm$; therefore the effective thickness of the dead layer is t=180 nm. This value is to be considered an effective thickness in silicon, which includes both the top oxide layer (around 110 nm, as measured by RBS) and the thickness in silicon immediately beneath the electrode (p+ layer), in which charge collection is inefficient, i.e. the generated charge carriers don't contribute to the CCE.

II.iv Ion micro-beam

Figure II-10 shows a schematic representation of a typical microbeam set-up: a MeV ion beam from an accelerator is focused by a system of electro-magnetic quadrupole lenses and scanned over the sample surface using two sets of magnetic or electrostatic plates. The inset on the right side shows the irradiation and IBIC measurements performed in frontal IBIC geometry. Each incident ion generates a measurable charge pulse, which is amplified and processed by a standard charge sensitive electronic chain. The data acquisition system acquires and stores every event along with the coordinates of the ion beam [Breese1996a].
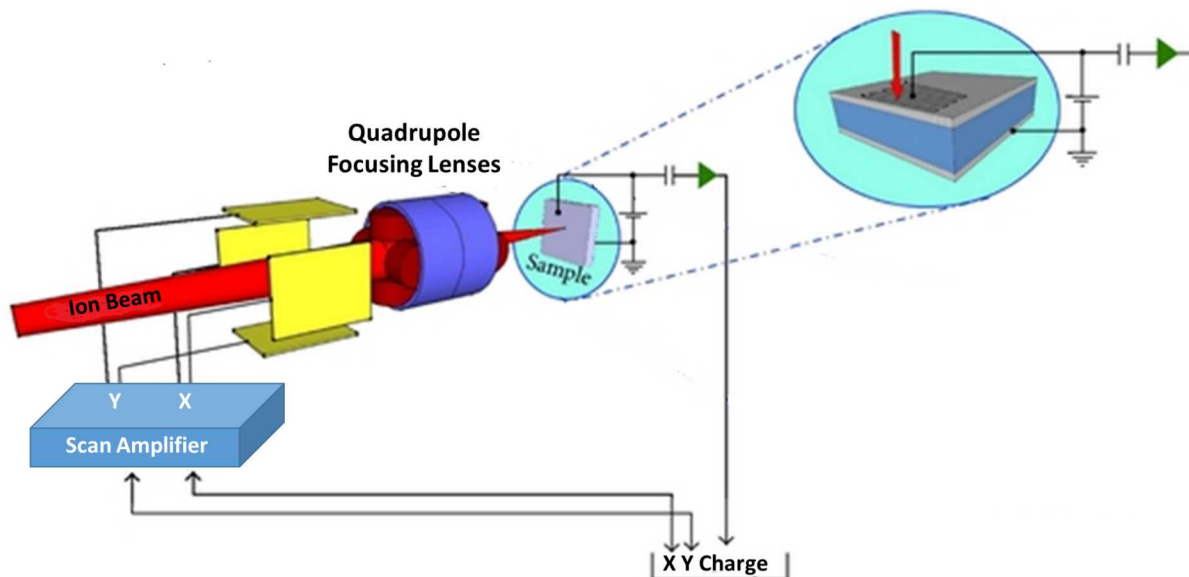
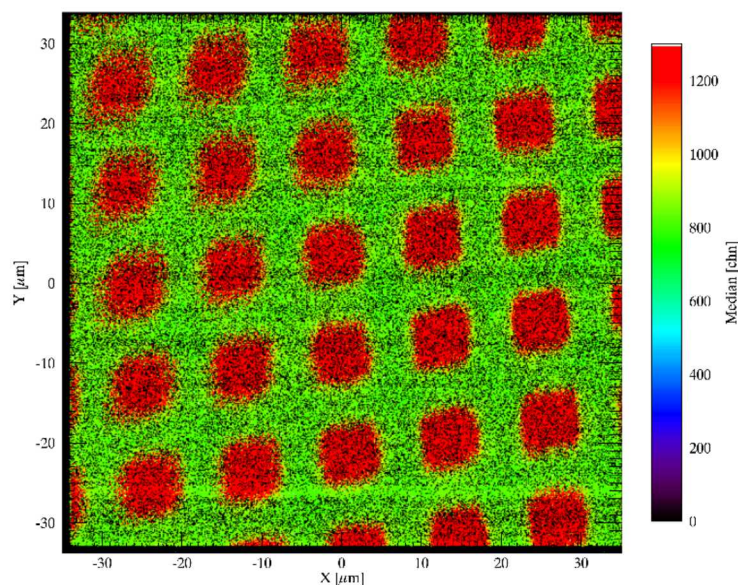*Figure II-10: Schematic representation of a typical ion microbeam set-up.*

Figure II-11 : STIM image of a 2000 mesh TEM grid using 8 MeV He ions [Vizkelethy2016]

In IBIC experiments, typical ion currents are of the order of fA (corresponding to a rate of less than 10^4 ions/s), which are compatible with the maximum data acquisition rate available with most microprobes [Breese1996, Bogovac2009]. The usual procedure to determine the spatial resolution as well as the dimensional scale of the scanning region is to acquire the on-axis STIM image of a TEM grid with known period, mounted on a reference detector.

Figure II-11 shows the on axis STIM image of a 2000 mesh (period 12.5 µm) TEM grid mounted on DUS1 using 8 MeV He ions.

The scan area and beam spot size is calculated by fitting a line scan of the high-energy peak to the theoretical profile. Figure II-12 shows the line profile in one direction with the fit; the inset shows the IBIC spectrum where

the lower energy peak corresponds to the wires (green in Figure II-11) and the higher energy peak corresponds to the holes (red in Figure II-11) in the grid. The counts between the two peaks are due to the walls are not exactly vertical but slightly tapered. The scan area determination with this method gives an error of about 2%. The beam spot size is about 1x2 μm^2 as calculated by the slope of the line scans (in both the horizontal and vertical directions).
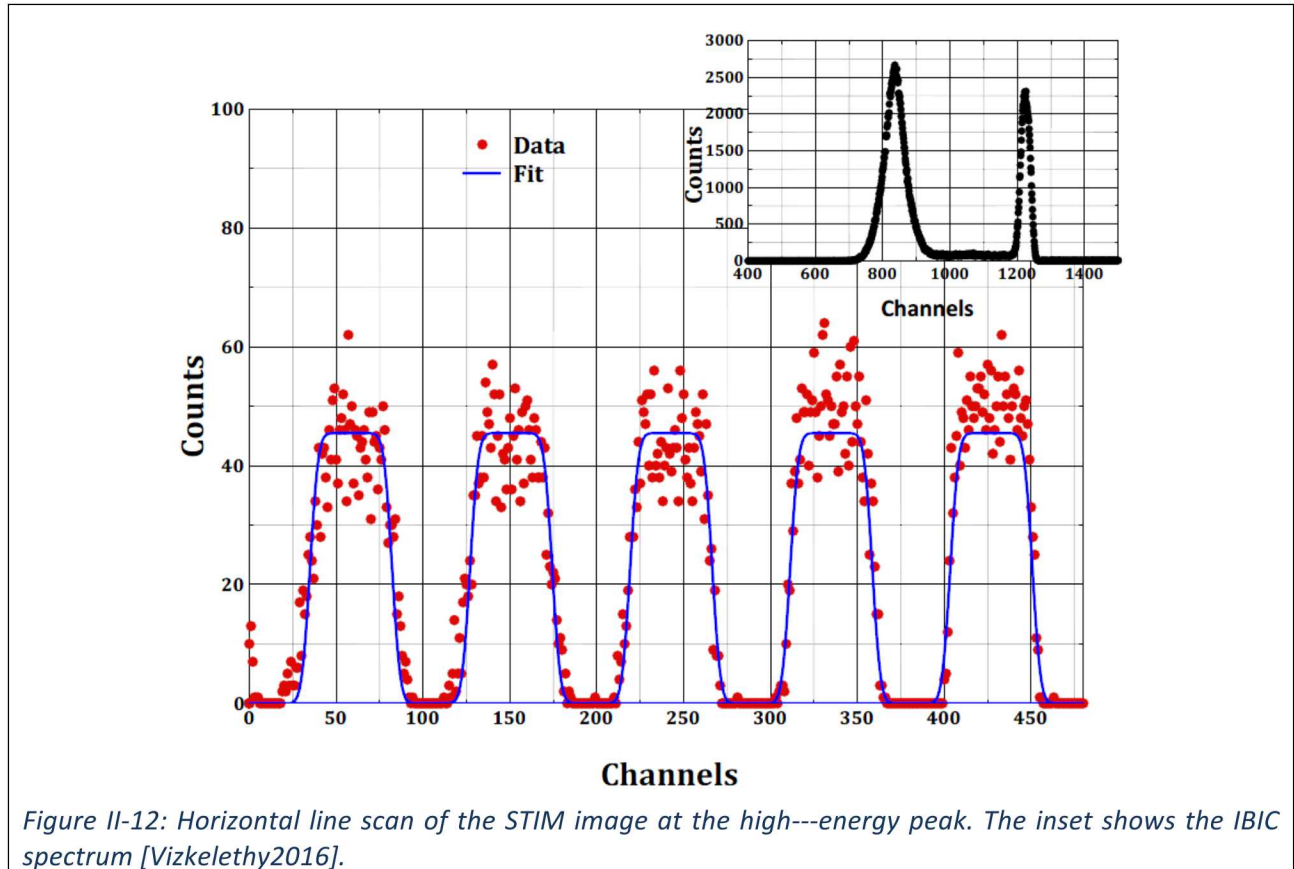

Figure II-12: Horizontal line scan of the STIM image at the high---energy peak. The inset shows the IBIC spectrum [Vizkelethy2016].

II.v   The experimental protocol

The experimental protocol is based on the use of (1) accelerated ions to induce damage by displacing lattice atoms in collision cascades in selectively irradiated regions of a device and (2) ions with the same or different range to probe the induced damage. In the following, these ions are named DIBs (damaging ion beams) and PIBs (probing ion beam), respectively. The protocol is organized in three steps:

a) IBIC map of regions of the pristine diode to assess the uniformity of the areas to be irradiated
b) Irradiation of N (typically N=9) regions at different fluences with DIBs (preferably at zero bias or bias as low as possible, which is sufficient for DIB particle discrimination/detection)
c) IBIC maps from PIBs of the irradiated regions recorded for different polarization conditions (biases).

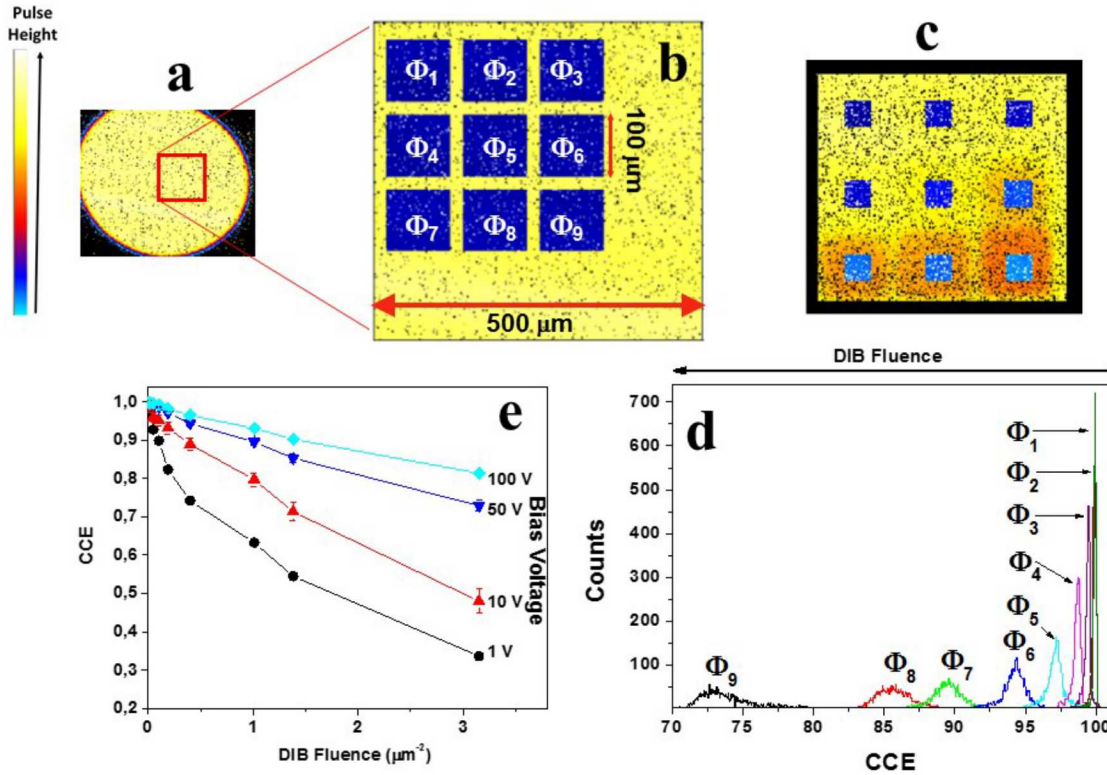Figure II-13 shows a scheme of the whole procedure.

Figure II-13: schematics of the experimental protocol: the diode (a) was first raster scanned with PIBs in order to individuate a region with uniform CCE. (b) Nine regions were selected and irradiated with DIBs at different fluences (U1 . . .U9). (c) PIBs were then used to probe the CCE degradation in the damaged regions and pulse height spectra were then extracted from the central zones of the damaged regions (d). Similar IBIC maps and spectra are obtained at different bias voltage and, finally, the centroids (median value) of the spectra were plotted as function of the DIBs fluence (e).

II.v.a   Preliminary IBIC map on pristine sample

This step is required in order to select uniform regions providing uniform IBIC response and determine the CCE value of the pristine sample. The extension of this region is evaluated in order to select N non-overlapping smaller areas to be irradiated by DIBs at different fluences. In the experiments carried out on DUS1, the region under study has (500x500) μm^2 area.

The IBIC mapping follows the established protocol presented in several publications [Breese1996a, Breese2007, Vittone2013]. Light ion beams of the reduced particle current (fractions of fA) are focussed by a system of quadrupole lenses down to the micrometre scale and scanned over the region of interest of the DUS. The current induced at the sensing electrode by the motion of charge carriers generated by ionization by each ion-projectile is integrated and amplified by the low noise electronic chain already described in a previous section (see Figure II-4).

II.v.b   Ion induced damage in selected regions

Typically, these regions have a constant area of 100x100 μm^2 (DUS1). DIBs scan these regions at increasing fluences (in the example reported in Figure II-13, the fluences are $\Phi_{1,..,9}$ = 85, 165, 1020, 1880, 3990, 10100,

13800, 31500 ions/ μm^2). Since the model is valid in the low damage conditions, the maximum DIB fluence should not induce the CCE degradation smaller than 70%.

The ion fluence is calculated by dividing the number of pulses by the surface area of the irradiated region. If standard IBIC conditions are adopted (ion currents of the order of 1 fA), the irradiation can be unacceptably slow; for example, with an ion current of 1 fA (corresponding to an ion rate of 6250 ions/s) with singly ionized DIBs, the time required to irradiate 100x100 μm^2 with a fluence of 10^4 ions/ μm^2 exceeds 4 h.

However, the pulse height analysis and acquisition of IBIC spectra is necessarily not required during irradiation at higher ion counting rates, which may overflow capability of the data acquisition system (induce a significant dead time and consequently the loss in number recorded events) increasing the inaccuracy of the total ion irradiation fluence. The ion counting accuracy at high ion rates (comparable with the inverse of shaping time causing the pile-up events) can be improved by using the logic TTL signal extracted from the shaping amplifier connected to a pulse discriminator set above the noise level and fed into a pulse counter. In this case, ion rates higher than 20 kHz can be easily achieved. The fluence of the abovementioned example can therefore be achieved in about 90 min; this duration is scaled down to 20 min if the irradiated area is 50x50 μm^2.

The uncertainty of the calculated fluence values is mainly dominated by the calibration of the scanning system (of the order of 1%).

The criteria to be adopted to choose the most suitable combination of probing and damaging ions can be inferred from Figure II-14, which shows, as an example, both the vacancy profile of 11.25 MeV He ions in silicon calculated by SRIM simulations [W5, Ziegler2010], assuming a displacement energy of 21 eV [Corbett1965] and the extension (w) of the depletion region as function of the applied bias voltage evaluated through eq. (2). At reverse bias voltages larger than 40 V, the whole vacancy profile is within the depletion region, whereas, for lower voltages, the highly damaged region is located in the neutral region of the diode. These facts have important implications on the CCE degradation behaviours: in the former case, recombination occurs in presence of high electric field, where drift transport dominates. In the latter case, the generation mainly affects the diffusion length of minority carriers. As a rule of thumb, it is convenient to choose ion species and energies so that the relevant vacancy profiles fall within the depletion region in correspondence of the allowed highest voltages.
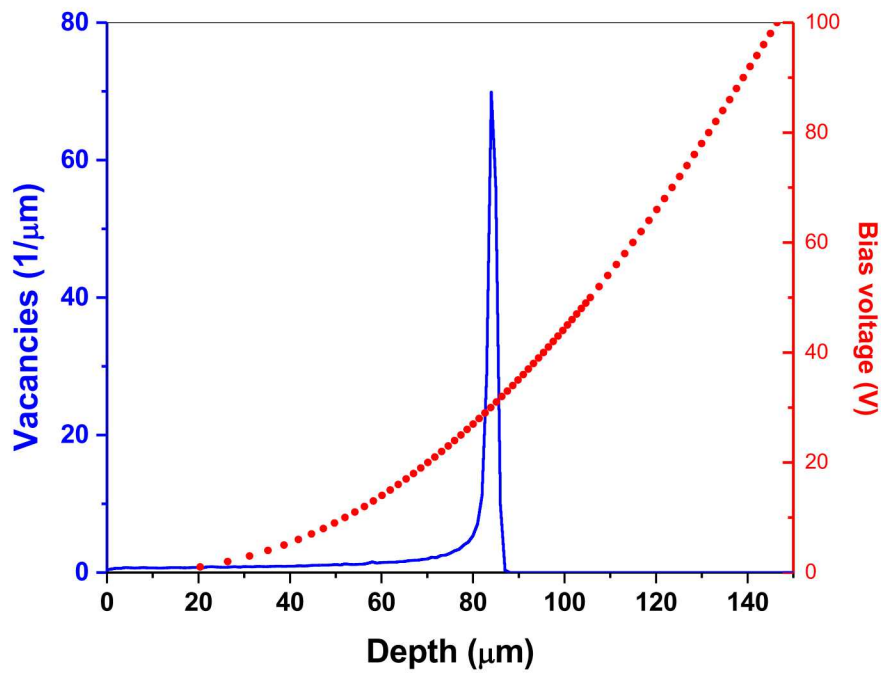
Figure II-14: Left-blu scale: vacancy profile of 11.25 MeV He ions in Si calculated by SRIM2013 simulation; right-red scale: depletion layer width vs. applied bias voltage (exchanged axes);
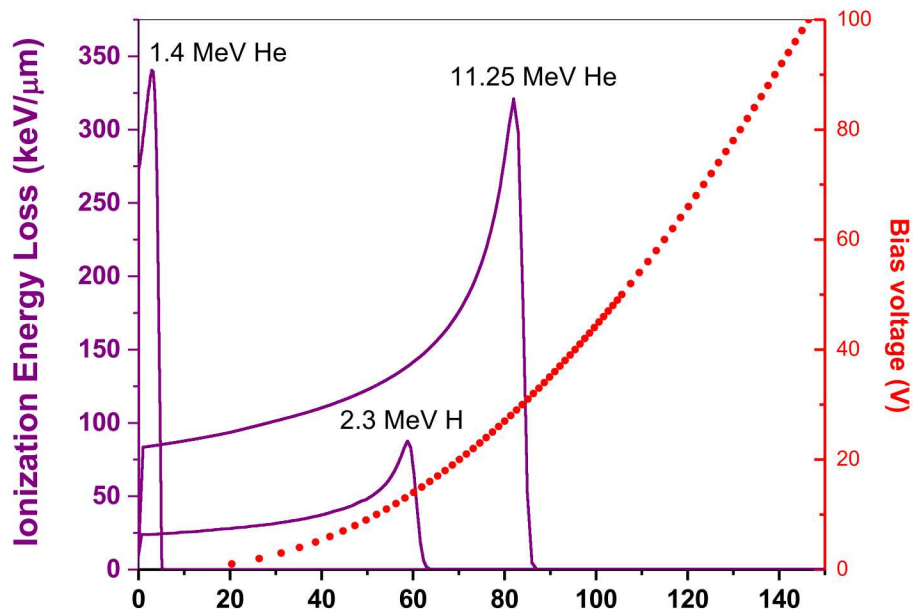
SR-CV-PIB-DIB.opj-gDIBgw

Figure II-15: Left-purple scale: ionization energy loss for different PIBs in silicon calculated by SRIM simulations; right-red scale: depletion layer width vs. applied bias voltage (exchanged axes)

SR-CV-PIB-DIB.opj-gPIBgw

II.v.c   IBIC maps of the damaged regions

The irradiated regions of the diode are then probed by PIBs using the same protocol adopted in step a). The criteria adopted for a choice of the suitable PIBs can be inferred from a comparison of the vacancy profile (Figure II-14) and the ionization profile (Figure II-15).
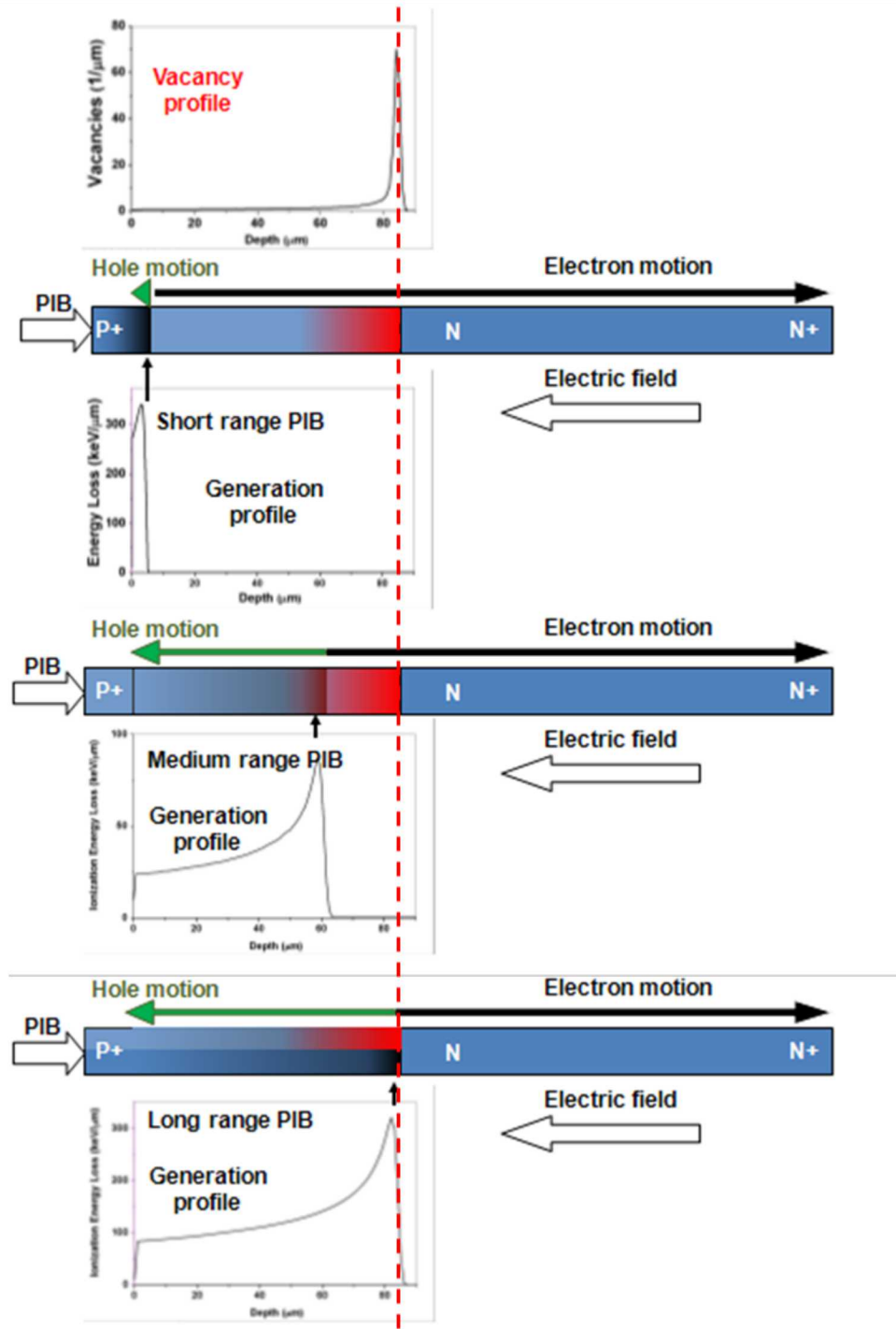

Figure II-16 : sketches of carrier motion in the depletion region with respect to the generation profile referred to the vacancy profile (top graph).

If PIB range is shallower than DIB (i.e. the PIB Bragg curve in Figure II-15 is shallower than the vacancy profile of DIB in Figure II-14, e.g. PIB=1.3 MeV He ions, DIB=11.25 MeV He ions) only one kind of carriers (majority carriers: electrons for n-type diodes) crosses the highly damaged region and the CCE degradation is dominated by the majority carriers recombination. When the ionization profile cover the whole DIB range (as with 11.25 MeV He ions), both the carriers suffer of recombination induced by DIB damage; if the PIB range is larger than the DIB range the CCE degradation is dominated by minority carriers (see for example [Vittone2016]). In the case of 2.3 MeV protons, the ionization profile covers part of the vacancy profile curve, excluding the vacancy peak; therefore, a dominant, but not exclusive, role of majority carrier recombination is expected. Figure II-16 summarizes the different situations occurring in fully depleted devices.

IBIC maps as shown in Figure II-13c allow the damaged regions to be easily localized. The halo visible in proximity of the highest damaged regions can indicate that the DIB irradiation has remarkably perturbed the effective doping of the diode. It was already observed that this effect induces a no negligible perturbation of the electric field, which can modify the carrier trajectories [Barbero2015]. If this effect occurs, the theoretical model described in the following sections cannot be rigorously applied, and the analysis has to be conducted only in regions with smaller DIB fluence.
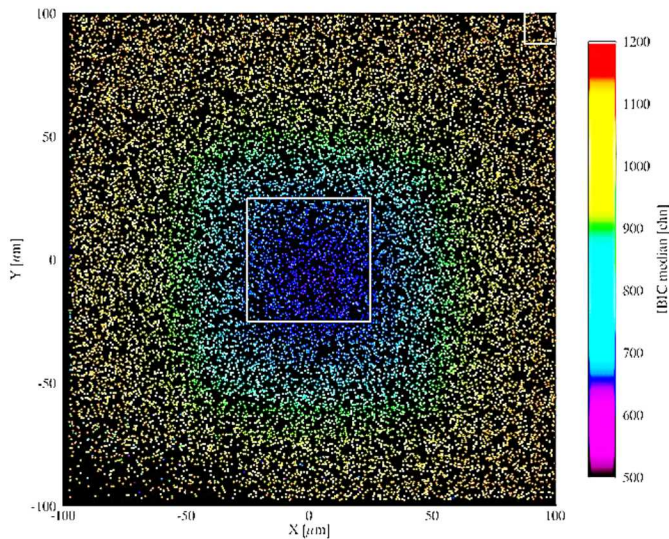

Figure II-17: IBIC median map of 4 MeV He irradiated DUS2 at 0 V [Vizkelethy2016].
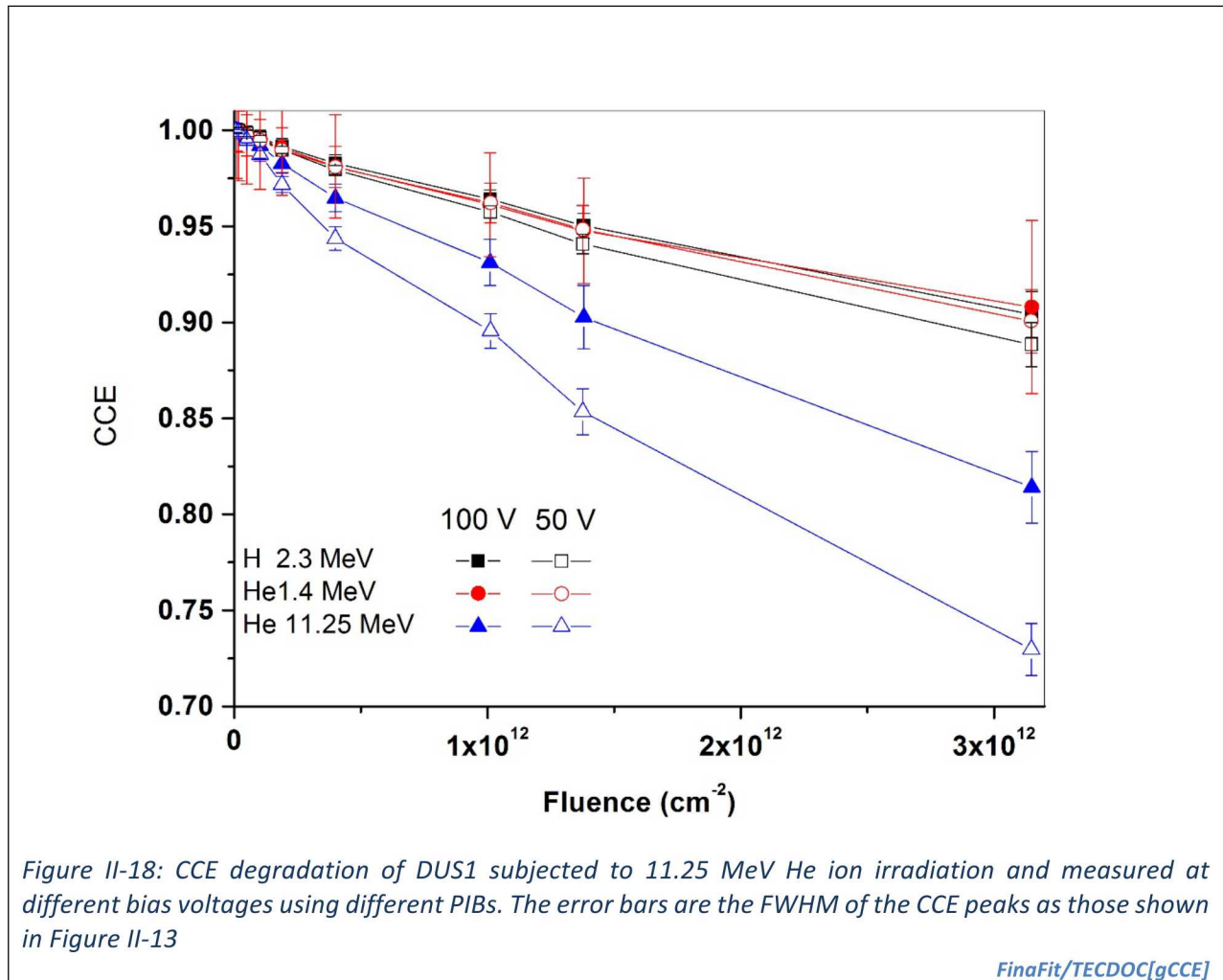
IBIC maps have to be acquired at different bias voltage. This introduces an additional variable, i.e. a modulation of the electric field strength, which is included in the interpretative model and provides further information on the transport/recombination mechanisms. Again, graphic representations of the vacancy profile (Figure II-14) and the ionization profile (Figure II-15) combined with the extent of depletion region as a function of bias can be useful to select the appropriate bias voltage. If, for example, 2.3 MeV protons are considered as PIBs, bias voltages larger than 15 V generate depletion layers larger than the PIBs range. This means that the dominant transport mechanism is the carrier drift, whereas, if lower bias voltages are applied, the diffusion of minority carriers generated in the neutral region has to be taken into account. Since diffusion of free carriers is in general a slower transport mechanism than drift, the recombination of free carriers is more effective at low bias voltage. This fact suggests that the best practice to identify the damaged area is to carry out IBIC mapping at low bias voltages, in order to enhance the contrast as shown in Figure II-17, which represents the IBIC median map of a damaged region acquired at 0 V. The image clearly shows the 100x100 μm^2 irradiation (the shape is square) and the circular region, which is due to carriers diffusing into the damaged region [Breese1993b, Doyle2000]. It also shows that free carriers created close to the edge of the

scanned area produce full CCE. The two white squares indicate the regions where the damaged and undamaged IBIC spectra are extracted.

II.v.d   CCE degradation curves

From each spectrum, the median value is evaluated and normalized with the median value of the spectrum relevant to the pristine region (Figure II-13d). Assuming a total induced charge collection of the pristine diode, this ratio gives the CCE value, and in the following text will be regarded as just the CCE.

Figure II-18: CCE degradation of DUS1 subjected to 11.25 MeV He ion irradiation and measured at different bias voltages using different PIBs. The error bars are the FWHM of the CCE peaks as those shown in Figure II-13

FinaFit/TECDOC[gCCE]

Finally, the measured CCE for any applied bias voltage are plotted as function of the DIB fluence (Figure II-13e).

A complete set of measurements carried out on DUS1 is shown in Figure II-18; similarly, the CCE degradation curves relevant to DUS2 are reported in [Vittone2016].

The stabilization of radiation induced defects, i.e. the removal of transient defects in order to leave only permanent defects, can be achieved by adopting the annealing procedure prescribed by [ASTM2007] (annealing at 80° for two hours in air). However, measurements carried out 10 days after irradiation (DIB= 8 MeV He ions with fluences ranging from 1 to 1000 ions/µm^2) of the CCE degradation of DUS2 before and after annealing did not show remarkable changes and curves overlap within errors [Vizkelethy2016].

III. THE INTERPRETATIVE MODEL

III.i Semiconductor device modeling: electrostatics

The continuity equations for electrons and holes[1]:

$$(5) \quad \begin{cases} \frac{\partial n}{\partial t} = \nabla \cdot [D_n \cdot \nabla n - v_n \cdot n] - R_n + G_n \\ \frac{\partial p}{\partial t} = \nabla \cdot [D_p \cdot \nabla p - v_p \cdot p] - R_p + G_p \end{cases}$$

and the Poisson's equation,

$$(6) \quad \nabla^2 \varphi = -\nabla \cdot E = -\frac{\rho}{\varepsilon} = -\frac{q \cdot (N_D - N_A + p - n)}{\varepsilon}$$

are the basic equations, which describe charge transport phenomena occurring in semiconductor devices [Grove1967].

The solution of this system of differential equations provides the electron (n) and hole (p) concentrations, and hence the current density ($J_{n,p}$), the electrostatic potential and electric field as function of the semiconductor doping (N_A, N_D), of the carrier recombination mechanisms ($R_{n,p}$), of the transport parameters (mobility $\mu_{n,p}$, diffusivity $D_{n,p}$), of the applied bias voltage, of the built-in potential and, in general, of the boundary and initial conditions.

In the studied case of a semiconductor device with a planar geometry, we can further simplify the problem by reducing it to only one dimension (depth) by the perpendicular irradiation of the front contact electrode and assuming the trajectories of high energy ion projectiles (MeV energy range) in a material are nearly straight lines [Vittone2016].

As described in the introduction, the model is based on an accurate knowledge of the device electrostatics, induced by a constant applied bias potential to the electrodes of DUS. This means that steady state conditions can be considered (**Assumption I**)

In the following, we restrict the analysis to an one-dimensional device of length d, i.e. the integration domain is [0,d] (**Assumption II**). Under these assumptions, the continuity and Poisson's equations become:

$$(7) \quad \begin{cases} \frac{\partial}{\partial x}\left[D_n \cdot \frac{\partial n}{\partial x} - v_n \cdot n\right] - R_n + G_n = 0 \\ \frac{\partial}{\partial x}\left[D_p \cdot \frac{\partial p}{\partial x} - v_p \cdot p\right] - R_p + G_p = 0 \\ \frac{\partial^2 \varphi}{\partial x^2} = -\frac{\partial E}{\partial x} = -\frac{\rho}{\varepsilon} = -\frac{q \cdot (N_D - N_A + p - n)}{\varepsilon} \end{cases}$$

In order to determine the electrostatics of the device, we assume that the terminal at x=d is grounded and at x=0, at the applied bias voltage V (**Assumption III**) and that the contacts are ohmic (**Assumption IV**); the relevant boundary equations are then:

---

[1] In the text a standard notation used text on semiconductor physics is adopted. The definition of the parameters is listed in Section VII,

$$\varphi(x = 0) = V + V_{bi} \; ; \; \varphi(x = d) = 0$$

$$(8) \quad n(x = 0) = n_0(x = 0) \; ; \; n(x = d) = n_0(x = d)$$

$$p(x = 0) = p_0(x = 0) \; ; \; p(x = d) = p_0(x = d)$$

where V_{bi}, n_0 and p_0 are the built in potential and the carrier concentrations in thermal equilibrium conditions, respectively. The built-in potential V_{bi} is given by:

$$(9) \quad V_{bi} = \varphi(x = d) - \varphi(x = 0) = \frac{k_B \cdot T}{q} \ln\left(\frac{p_0(x=0) \cdot n_0(x=d)}{n_i^2}\right)$$

To solve the equation system (7), it is convenient to adopt the following functions:

$$(10) \quad \varphi_N = \frac{q}{k_B \cdot T} \varphi = \frac{\varphi}{V_{th}} \; ; \; f_p = \varphi_N + \ln\left(\frac{p}{n_i}\right) \; ; \; f_n = \varphi_N - \ln\left(\frac{n}{n_i}\right)$$
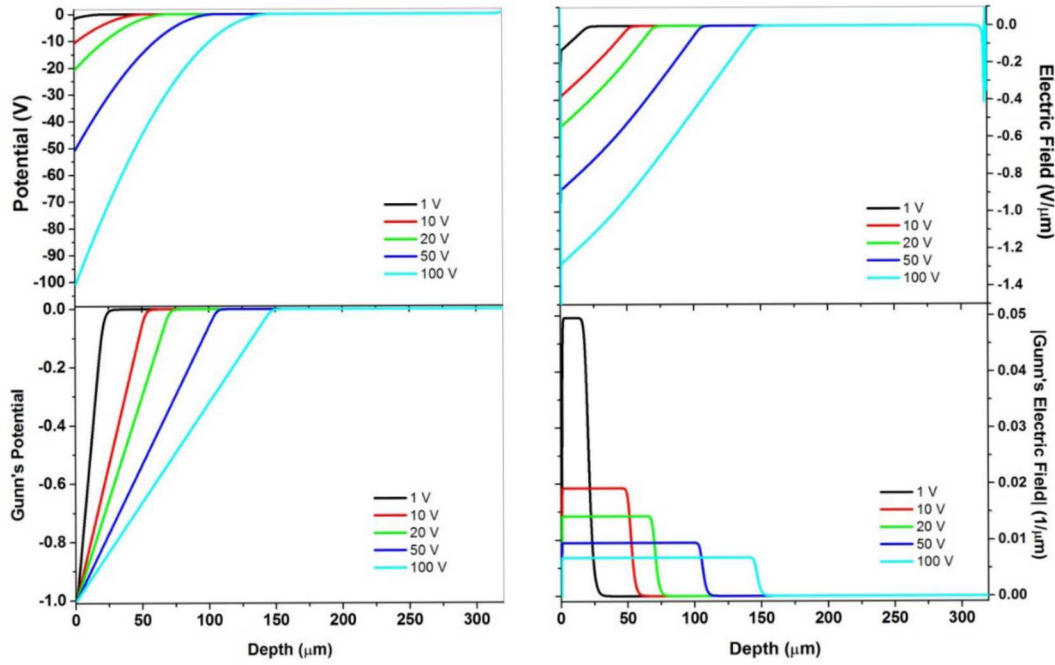
Figure III-1: electrical features of DUS1: a) electrostatic potential profile; b) electric field profile; c) Gunn's potential profile; d) Gunn's electric field profile.

Electrical-features.ogg

The relevant continuity and Poisson's equations can then be written as:

$$(11) \quad \begin{cases} -n_i \cdot V_{th} \cdot \dfrac{\partial}{\partial x}\left[\mu_n \cdot \left(e^{\varphi_N - f_n}\right)\left(\dfrac{\partial f_n}{\partial x}\right)\right] - R_n = 0 \\[2mm] n_i \cdot V_{th} \cdot \dfrac{\partial}{\partial x}\left[\mu_p \cdot \left(e^{-\varphi_N + f_p}\right)\left(\dfrac{\partial f_p}{\partial x}\right)\right] - R_p = 0 \\[2mm] \dfrac{\partial^2 \Phi}{\partial x^2} = -\dfrac{q}{V_{th} \cdot \varepsilon} \cdot \left(N_D - N_A + n_i \cdot e^{-\varphi_N + f_p} - n_i \cdot e^{\varphi_N - f_n}\right) \end{cases}$$

With the following boundary conditions:

$$f_{n,p}(x=0) = \frac{V}{V_{th}} \; ; \; f_{n,p}(x=d) = 0$$

$$(12) \quad \varphi_N(x=0) = \frac{V}{V_{th}} - \ln\left(\frac{p(x=0)}{n_i}\right) \; ; \; \varphi_N(x=d) = \ln\left(\frac{n(x=d)}{n_i}\right)$$

Figure III-1 a) and b) show the electrostatic potential and the electric field profiles, respectively, of DUS1, at different bias voltages; Gunn's potential and electric field will be defined in Section III.iii . The carrier drift velocity profiles (i.e. v_n= -μ_n ·E for electrons and v_p= μ_p ·E for holes) is shown in Figure III-2.

For silicon, a widely used expression for mobility was proposed by Scharfetter and Gummel [Scharfetter1969, Selbehrerr1984];

$$(13) \quad \mu_{n,p}(E) = \frac{\mu_{0,n,p}}{\left[1 + \dfrac{CI}{C_{n,è}^{ref} + CI/S_{n,p}} + \dfrac{\left(E/A_{n,p}\right)^2}{E/A_{n,p} + F_{n,p}} + \left(\dfrac{E}{B_{n,p}}\right)^2\right]^{1/2}}$$

Where CI is the ionized impurity concentration and all the other parameters relevant to silicon at 300 K are listed in Table III-1.

Symbol	Recommended values for silicon at 300 K [Selbehrerr1984]		
	Electrons	Holes	Unit
μ_0	1400	480	cm^2/(V·s)
C^{ref}	$3\cdot10^{16}$	$4\cdot10^{16}$	cm^{-3}
S	350	81	
A	3500	6100	V/cm
F	8.8	1.6	
B	7400	25000	V/cm

Table III-1: Coefficients for carrier mobility of (11)

III.ii Semiconductor device modeling: quasi-state conditions.

The continuity equations can be used to determine the steady-state conditions within a semiconductor device and to model transients caused by radiation interactions. In most applications, semiconductor devices operate in a quasi-steady-state mode for which the assumption that excess charge produced by radiation interactions doesn't significantly perturb the field within the detector. Consequently, the continuity equations can be de-coupled from Poisson's equation. We will further assume that the electron and hole continuity equations can be decoupled and that the generation— recombination terms can be linearized. These assumptions have been used routinely in the analysis of semiconductor detectors [Barrett1995, Prettyman1999a,b]:

Assumption V: The semiconductor device operates in a quasi-steady-state mode. The excess charge produced by radiation interactions does not significantly perturb the field within the detector. Consequently, the continuity equations can be de-coupled from Poisson's equation.

Assumption VI: Linearization of the generation-recombination terms:

$$(14) \quad \begin{aligned} R_n &= \frac{n}{\tau_n} \\ R_p &= \frac{p}{\tau_p} \end{aligned}$$

This approximation is valid when (1) the excess carrier concentration is small compared to the number of available trapping and recombination centres and (2) the de- trapping time is small compared to the transit time. In this case, the rate of removal of carriers is proportional to the carrier concentration.

The parameters of the excess carrier equation, including the mobility (see eq. (13), diffusion coefficient ($D=V_{th}\cdot\mu$), vary with position and electric field. Similarly, free-carrier lifetime is also space-dependent, through the following expression:

$$(15)\ \tau_n = \frac{3.94\cdot10^{-4}}{1+\frac{N_A+N_D}{N^{ref}}}\ ;\ \tau_p = \frac{3.94\cdot10^{-5}}{1+\frac{N_A+N_D}{N^{ref}}}$$

Where $N^{ref} = 7.1\cdot10^3\ \mu m^{-3}$ [Selbehrerr1984]
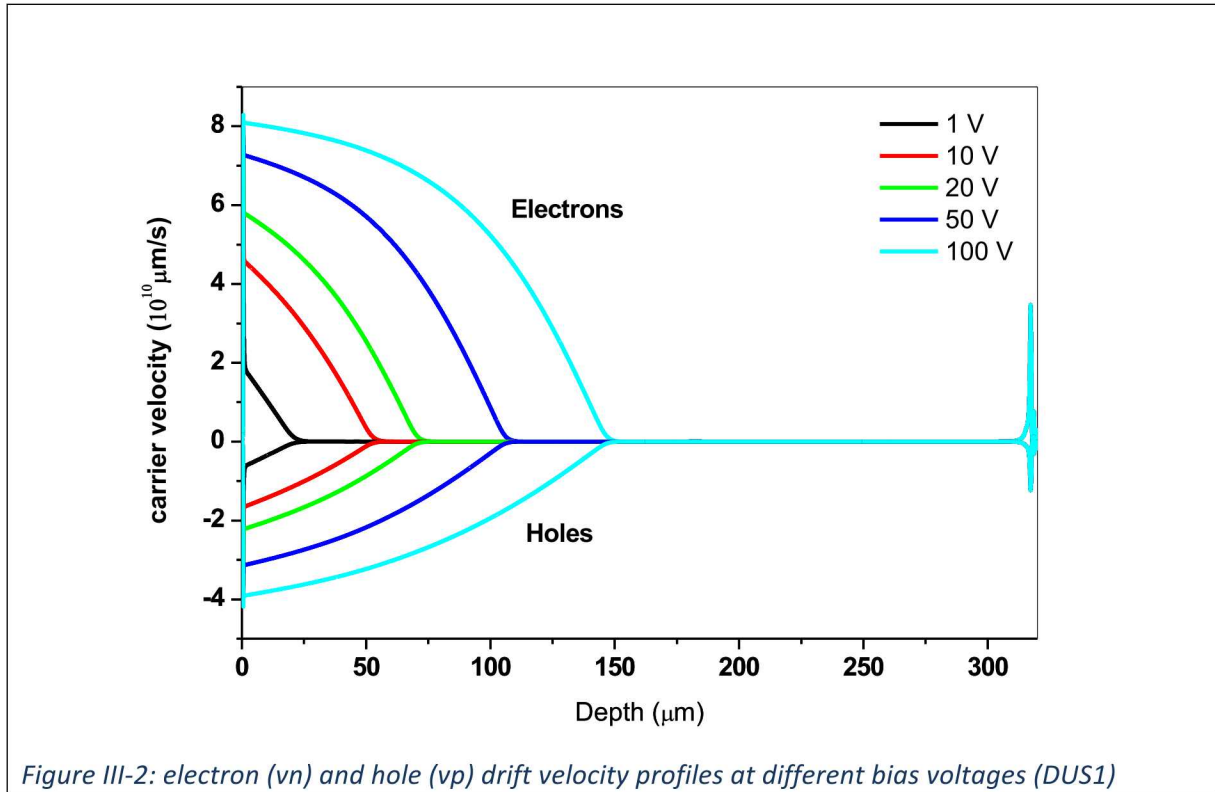
Figure III-2: electron (vn) and hole (vp) drift velocity profiles at different bias voltages (DUS1)

The Assumptions V and VI lead to the following spatial - temporal equation for the concentration of excess carriers within the semiconductor:

$$(16)\begin{cases}\frac{\partial n}{\partial t} = \nabla \cdot [D_n \cdot \nabla n - v_n \cdot n] - \frac{n}{\tau_n} + G \\ \frac{\partial p}{\partial t} = \nabla \cdot [D_p \cdot \nabla p - v_p \cdot p] - \frac{p}{\tau_p} + G\end{cases}$$

In these last equations, n and p have to be intended as the concentration of excess electron and hole concentrations, respectively.

The initial condition for the problem is

$(17)\, n(x, 0) = 0$

where $x \in \Omega$, where Ω is the set of points within the semiconductor. For mapping charge pulses, the generation term is selected to be an impulse of unit charge: $G = \delta(x-x_0) \cdot \delta(t)$.

III.iii Semiconductor device modelling: induced charge.

The current induced in electrodes by the motion of charge carriers can be estimated using the weighting potential method adopting the formulation proposed by J. Gunn [Gunn1964, Vittone2004], which is an extension of the well-known Shockley-Ramo theorem [Shockley1938, Ramo1938]. Using this method, the charge induced on individual electrode connected to a common circuit can be determined. Here, the analysis is confined to cases in which the electrode potential is not influenced by charge motion, which is consistent with the assumptions used to decouple the semiconductor equations.

The total charge $Q_{n,p}$ induced at the sensing electrode at time t by the motion of electrons and holes generated in a certain positon x_0, is given by:

$$(18)\, Q(t) = Q_n(t) + Q_p(t) = -q \cdot \int_0^t dt' \int_\Omega dx [n \cdot v_n + p \cdot v_p] \cdot \frac{\partial E}{\partial V}$$

where n and p are the excess charge concentrations of electrons and holes, respectively, whose spatial-temporal evolution can be calculated by solving the electron/hole continuity equations with the initial conditions: $n(x, t = 0) = p(x, t = 0) = \delta(x - x_0)$, where δ is the Dirac delta function. Details on the theory leading to eq. (18) are given in numerous publications [Manfredotti2003, Vizkelethy2009, Vittone2016].

The term $E^+ = \frac{\partial E}{\partial V}$ is the Gunn's weighting field which is defined as the partial derivative of the actual electric field (E) with respect to the bias voltage V applied to the sensing electrode, while the voltage is kept constant on all the other electrodes.

It is important to understand that decoupling of the electron and hole contributions in Eq. (18) implies not only the negligible interaction of electrons and holes, but also the linear superposition of the electron/hole recombination/trapping processes.

The Gunn's weighting potential $\phi^+ = \frac{\partial \phi}{\partial V}$ and the Gunn's weighting field $E^+ = \frac{\partial E}{\partial V}$ profiles of DUS1 at different bias voltages are shown in Figure III-1c,d , respectively. The calculation of these terms can be effectively carried out by solving the following differential equations, which can be extracted from the continuity and Poisson's equations (11):
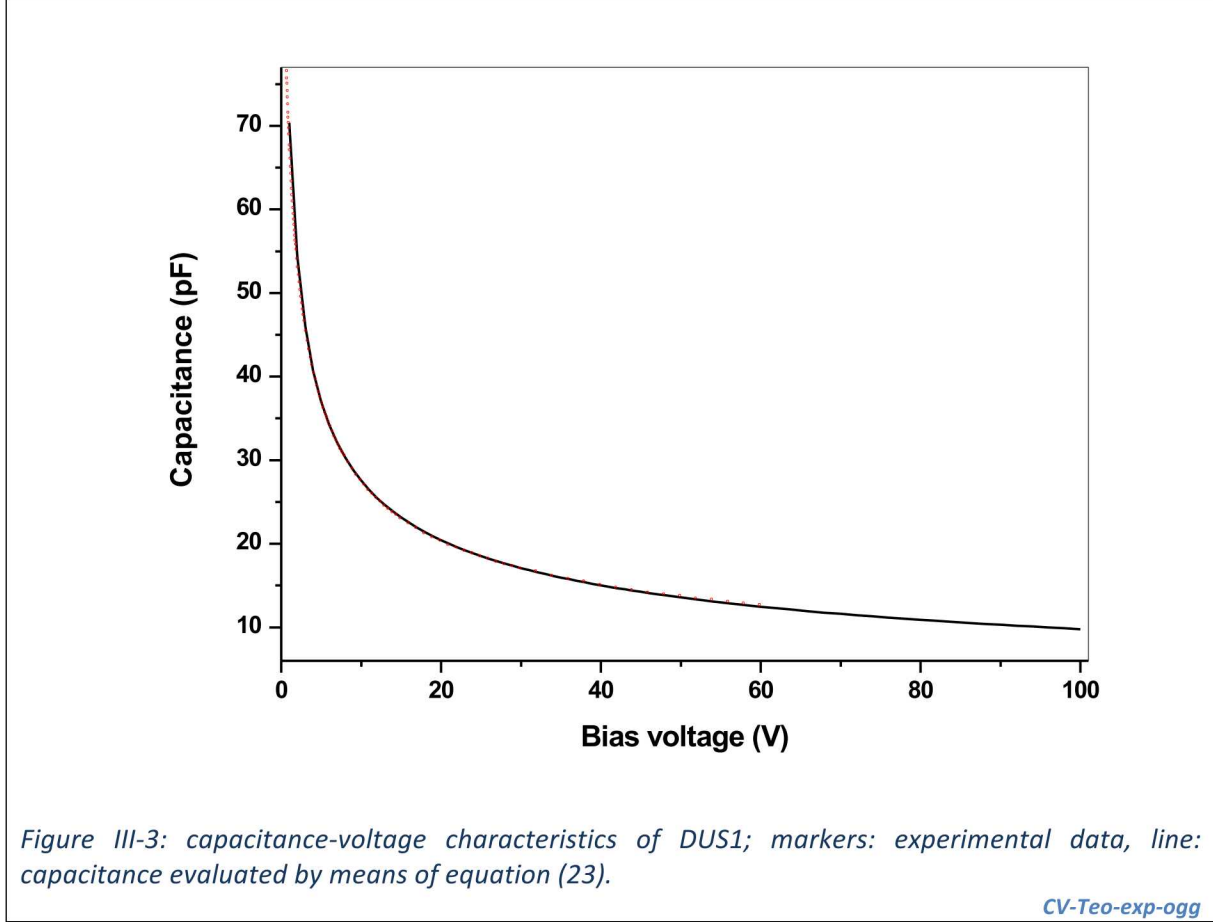
$$(19)\, \begin{cases} \frac{\partial}{\partial x}\left\{\mu_n \cdot n \cdot \left[\frac{\phi^+}{V_{th}} \cdot \frac{\partial f_n}{\partial x} - f_n^+ \cdot \frac{\partial f_n}{\partial x} + \frac{\partial f_n^+}{\partial x}\right]\right\} = 0 \\ \frac{\partial}{\partial x}\left\{\mu_p \cdot p \cdot \left[-\frac{\phi^+}{V_{th}} \cdot \frac{\partial f_p}{\partial x} + f_p^+ \cdot \frac{\partial f_p}{\partial x} + \frac{\partial f_p^+}{\partial x}\right]\right\} = 0 \\ \frac{\partial^2 \phi^+}{\partial x^2} = -\frac{q}{\varepsilon} \cdot \left[p \cdot \left(f_p^+ - \frac{\phi^+}{V_{th}}\right) + n \cdot \left(f_n^+ - \frac{\phi^+}{V_{th}}\right)\right] \end{cases}$$

where we assumed

$$(20)\, \frac{\partial \mu_{n,p}}{\partial V} = 0 \; ; \frac{\partial R}{\partial V} = 0$$

The boundary conditions are easily derived from eq. (12):

$$(21) \quad f^+_{n,p}(x = 0) = \frac{1}{V_{th}} \; ; \; f^+_{n,p}(x = 0) = 0$$

$$\varphi^+(x = 0) = 1 \; ; \; \varphi^+(x = d) = 0$$

Figure III-3: capacitance-voltage characteristics of DUS1; markers: experimental data, line: capacitance evaluated by means of equation (23).

CV-Teo-exp-ogg

It is worth noticing that, from the calculus of the Gunn's weighting field $E^+ = \frac{\partial E}{\partial V}$, through the Gauss law $\text{div}(E) = \frac{\rho}{\epsilon}$, we can easily evaluate the capacitance of the diode if a complete depletion is assumed:

$$(22) \quad \text{div}(E) = \frac{\rho}{\epsilon} \Rightarrow \text{div}(E^+) = \frac{1}{\epsilon}\frac{\partial \rho}{\partial V} \Rightarrow E^+(w) - E^+(0) = \frac{A}{\epsilon}\frac{\partial}{\partial V}\int_0^w dx \cdot \rho = \frac{A}{\epsilon}\frac{\partial q_T}{\partial V} = \frac{A}{\epsilon} \cdot C$$

where q_T is the total space charge within the depletion region of extension w and area A.

Therefore,

$$(23) \quad C(V) = \frac{\epsilon}{A} \cdot [E^+(w(V)) - E^+(0)]$$

Figure III-3 shows a comparison of the experimental capacitance - voltage characteristics of DUS1 with the curve evaluated through eq. (23).

The excellent agreement of the experimental and simulated data was obtained by solving eqs. (11)and (19) and using the doping profile extracted from SR profiling and shown Figure II-3. The area of the electrode (term A in eq. (23)) was set to 13.8 mm^2 as previously stated.

III.iv Semiconductor device modelling: the adjoint equation method.

An efficient method to evaluate the induced charge is based on the solution of the adjoint continuity equation, which can be constructed from eq. (16), since it involves only linear operators [Prettyman1999a,b, Vittone2016 and references therein].

Actually, if the free carrier generation terms are defined in the following manner

$$(24) \begin{cases} G_n^+ = -v_n \cdot \mathrm{E}^+ - \nabla \cdot [D_n \cdot \mathrm{E}^+] \\ G_p^+ = v_p \cdot \mathrm{E}^+ + \nabla \cdot [D_p \cdot \mathrm{E}^+] \end{cases}$$

the two terms in eq. (18) are the Green's function of the carrier (electron or hole) continuity equations.

Consequently, the contribution of electrons and holes to the induced charge can be evaluated by solving the adjoint equations of the relevant continuity equations, i.e.

$$(25) \begin{cases} \dfrac{\partial n^+}{\partial t} = \nabla \cdot [D_n \cdot \nabla n^+] + v_n \cdot \nabla n^+ - \dfrac{n^+}{\tau_n} + G_n^+ \\ \dfrac{\partial p^+}{\partial t} = \nabla \cdot [D_p \cdot \nabla p^+] + v_p \cdot \nabla p^+ - \dfrac{p^+}{\tau_p} + G_p^+ \end{cases}$$

The solution of these adjoint equations yields spatial and temporal map of the charge induced at the sensing electrode as a consequence of the motion of free electrons and holes generated in x∈Ω, namely:

$$(26)\, Q(x,t) = Q_n(x,t) + Q_p(x,t) = q \cdot [n^+(x,t) + p^+(x,t)]$$

In many applications, the physical observable is the total induced charge; therefore, we can furtherly consider the steady state adjoint equations (25) :

$$(27) \begin{cases} \nabla \cdot [D_n \cdot \nabla n^+] + v_n \cdot \nabla n^+ - \dfrac{n^+}{\tau_n} + G_n^+ = 0 \\ \nabla \cdot [D_p \cdot \nabla p^+] + v_p \cdot \nabla p^+ - \dfrac{p^+}{\tau_p} + G_p^+ = 0 \end{cases}$$

With the following homogeneous boundary conditions:

$$(28) \begin{cases} n^+(x = 0) = n^+(x = d) = 0 \\ p^+(x = 0) = p^+(x = d) = 0 \end{cases}$$

Therefore, both the electron and hole contributions to the total induced charge profiles can be calculated by solving these equations. Figure III-4 shows the electron and hole contributions to the induced charge evaluated by solving eqs. (27), considering an applied reverse bias voltage of 50 V (see Figure III-1 and Figure III-2 for the relevant electrostatic and transport profiles) and carrier lifetimes given by eq.(15). Since the lifetime is much longer than the drift time, almost all the free carriers generated into the depletion region are collected. This is the origin of the plateaux extending all through the extension of the depletion region (to be intended as the region where the Gunn's weighting potential is not null, as shown in Figure III-1). Outside the depletion region, i.e. in the neutral region where no electric field occurs, the n+ profile is null because electrons (majority carriers) hardly enter the depletion region because of the opposite electric field. On the other hand, hole contribution follow a typical exponential profile, which is due to their injection by diffusion into the depletion region, resulting in an induced signal by virtue of eq. (26) [Vittone2016].

Figure III-4: electron (n^+) and hole (p^+) adjoint concentrations of DUS1. applied bias voltage: 50 V. The dashed region indicate the depletion layer.
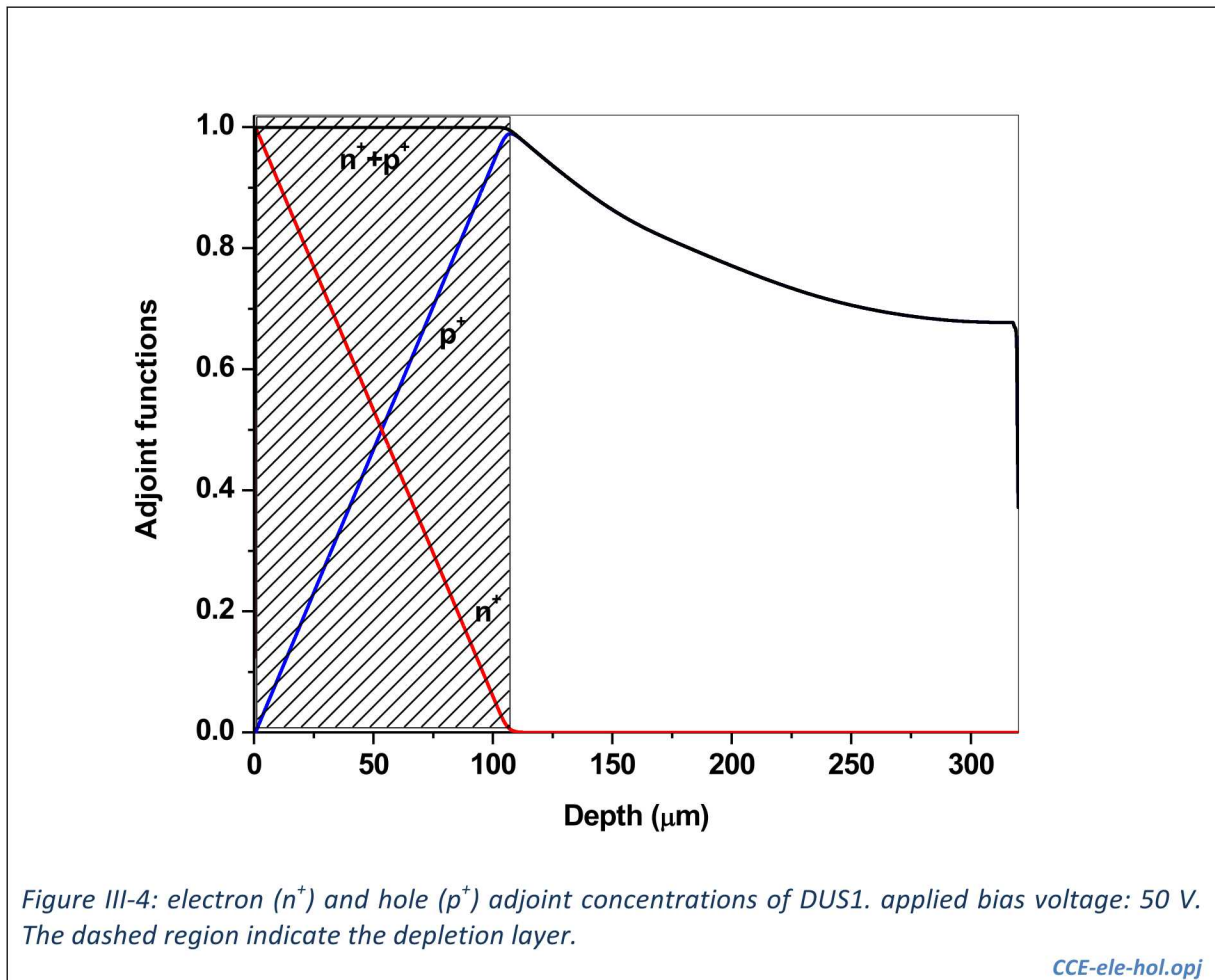
III.v   Modeling of radiation induced recombination mechanism

According to the Shockley-Read-Hall (SRH) model, the carrier lifetime is related to the concentration of recombination centres N^T through the following expression [Shockley1952, Chih1991]:

$$(29) \quad \frac{1}{\tau_{n,p}} = N_{n,p}^T \cdot \sigma_{n,p} \cdot v_{n,p}^{th}$$

where $v_{n,p}^{th}$ and $\sigma_{n,p}$ are the carrier thermal velocities and the carrier capture cross sections, respectively.

Eq. (29) allows the effect of radiation damage to be integrated in the unique radiation damage model by assuming the proportionality of the recombination centre concentration N^T and the concentration of vacancy-interstitial Frenkel pairs (FP) as created immediately after irradiation as can be calculated from Binary Collision Approximation codes, such as SRIM [W5].

It follows that the (**Assumption VII)** carrier lifetime distributions can be related to the recombination parameters using the following equation [Vittone2016 and references therein]:

$$(30) \quad \frac{1}{\tau_{n,p}} = N_{n,p}^{T0} \cdot \sigma_{n,p}^{0} \cdot v_{n,p}^{th} + N_{n,p}^{T} \cdot \sigma_{n,p} \cdot v_{n,p}^{th} = \frac{1}{\tau_{n,p}^{0}} + K_{n,p} \cdot \Phi$$

where the superscript *"0"* denotes terms corresponding to the pristine material, $\tau_{n,p}$ is the lifetime after the irradiation with the fluence Φ of damaging ions, which generate the concentration $N^T(x)$ of recombination centres with capture cross section $\sigma_{n,p}$; $K_{n,p}$ is the (recombination) lifetime damage coefficient defined as

$$(31) \quad K_{n,p}(x) = \frac{N_{n,p}^{T}(x) \cdot \sigma_{n,p} \cdot v_{n,p}^{th}}{\Phi}$$

Furthermore, under the previous assumption that N^T to FP ratio is constant in depth, the concentration of active recombination centres $N_{n,p}^{T}$ scales with the damaging ion fluence Φ. The product of the vacancy concentration distribution per ion, i.e. the vacancy distribution profile Vac(x) (which can be calculated by the SRIM code), and the average number of active defects (carrier recombination centre) generated by a single vacancy (k), gives the proportionality factor:

$$(32) \quad N_{n,p}^{T}(x) = k_{n,p} \cdot Vac(x) \cdot \Phi \Rightarrow K_{n,p}(x) = k_{n,p} \cdot \sigma_{n,p} \cdot v_{n,p}^{th} \cdot Vac(x) = \alpha_{n,p} \cdot Vac(x).$$

Where the electron and hole capture coefficients $\alpha_{n,p}$ are defined as follows:

$$(33) \quad \alpha_{n,p} = k_{n,p} \cdot \sigma_{n,p} \cdot v_{n,p}^{th}.$$

As already mentioned, the one-dimensionality of the model remarkably simplifies the formalism. Moreover, it is compatible with the actual experimental protocol. Using a raster-scanned ion microbeam with micrometre spatial resolution for the vacancy production (ion projectiles entering the surface of a device within a pixel of about 1μm size with maximum angular deviation from normal incidence ±1°), the vacancy distribution generated along the ion cascade by secondary recoils deviating from the straight line direction of the projectile is averaged. It is important that due to irradiation conditions with the average ion beam rate up to 10 kHz and the pixel dwell time of 500μs, we can assume that defects formed in the individual cascades are well separated both in time and space. In other words, the finally formed defects (or electrically active trapping or recombination centers) are the results of a single ion hit and interplay of primary or point defects created in successive or neighbouring ion cascades is negligible considering (1) the characteristic time of particle interactions formulated in the ion spike model developed by F. Seitz [Seitz1954], (2) the average time between two ion impacts of the reduced ion rate (order of 10 or 100 μs) and (3) the pixel dwell time of rapidly scanning ion microbeam (order of 100 μs).

The cumulative effect of multiple scanning the region of interest to create each damage structure is the uniform cross sectional areal distribution of finally formed defects.

Therefore, we need to consider the generation of vacancies occurring mainly along the ion track, which develops along the direction normal to the irradiated electrode (i.e. x-direction).

The vacancy profile shown in Figure II-14 can then be used to evaluate the lifetime profiles. Figure III-5 shows the electron lifetime in DUS1 as function of the fluence Φ of DIB (11.25 MeV He ions), assuming a recombination coefficient $\alpha_n = 2500$ $\mu m^3/s$.

Figure III-5: electron lifetime in DUS1 in the pristine diode ($\Phi=0$) and irradiated with 11.25 MeV He ions at fluences of $\Phi=10\mu m^{-2}$ and $\Phi=100$ μm^{-2}.

Lifetime.opj
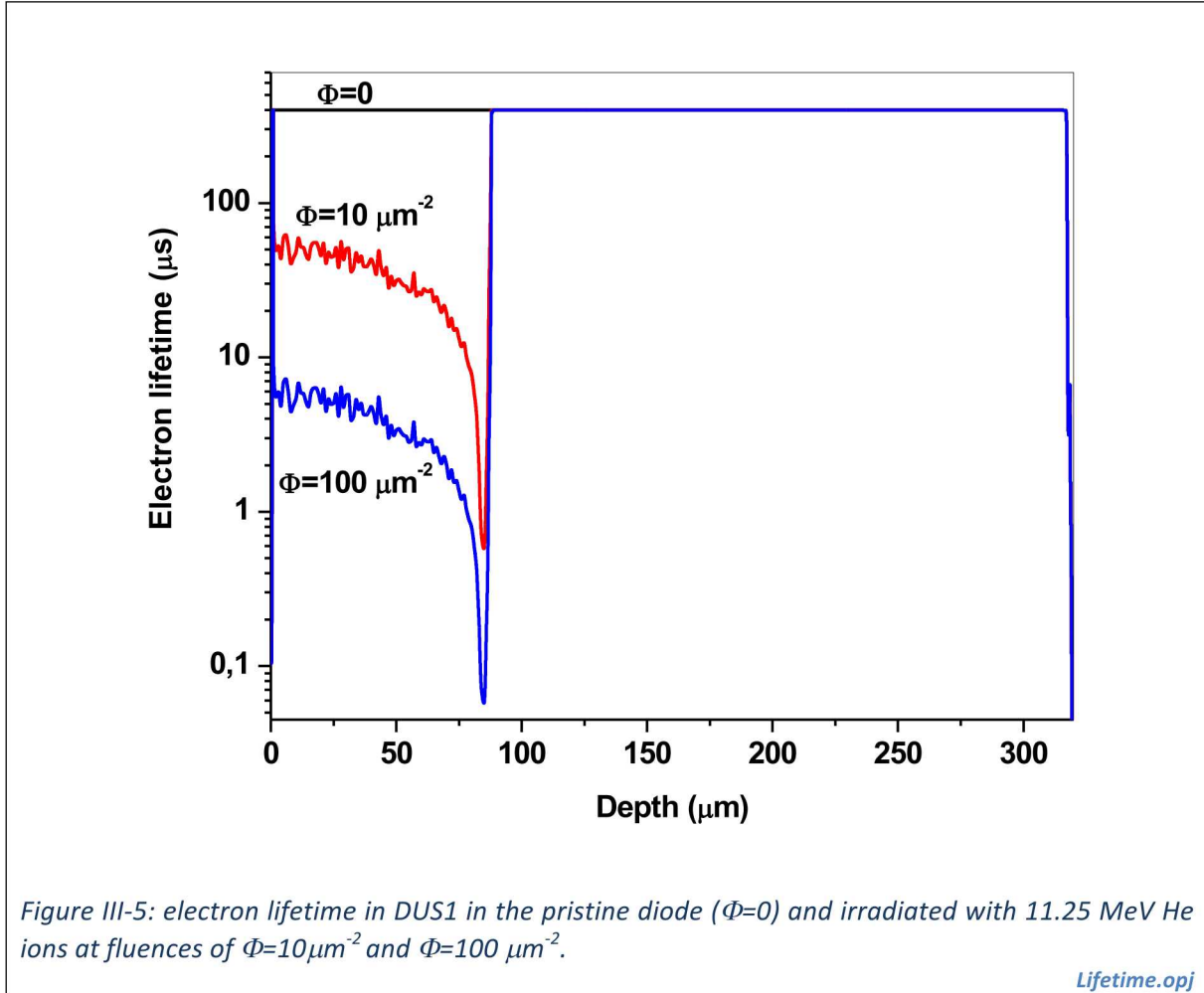
III.vi A general model for the CCE degradation in low damage conditions

The abovementioned equations relate to the induced charge generated by a single elementary charge moving within the semiconductor. However, to model the experiment described in Chapter II, we have to account for the generation profile of the PIB, which follow the Bragg curve as shown for example in Figure II-15. The nuclear energy loss of MeV light ions is small, thus the energy spent by the ion in electronic collisions results in the creation of electron-hole pairs and the carrier generation volume can be assumed as a function only of the x coordinate, being nearly cylindrical with a diameter of tens of nanometres [Breese2007].

The specific ion energy loss is then equivalent to the electronic stopping power, i.e. the amount of energy lost by the particle per unit-length of its track, which is related to the generation profile by the average energy ε_{np} (in silicon is 3.6 eV [Martini1965]) necessary to create an electron-hole pair in a given semiconductor at a given temperature and is almost independent of the type and the energy of the ionizing radiation.

$$(34)\ \Gamma = \frac{1}{\varepsilon_{np}} \frac{dE_I}{dx}$$

Where Γ is the generation profile, i.e. average number of electron/hole pairs generated by ionization per unit path.

The total induced charge at the sensing electrode produced by a single probing ion of energy E_I is then given by the superposition of the contributions of any carrier generated along the ion trajectory, i.e. by the convolution of the generation profile $\Gamma(x)$ and the charge induced by a single carrier moving within the semiconductor described by eq. (26):

$$(35)\ Q = q \int_0^d dx \cdot \Gamma(x) \cdot [n^+(x) + p^+(x)]$$

The charge collection efficiency (CCE) is given by the ratio of the induced charge Q and the total charge generated by ionization

$$(36)\ \text{CCE} = \frac{Q}{Q_0} = \frac{\int_0^d dx \cdot \Gamma(x) \cdot [n^+(x) + p^+(x)]}{\int_0^d dx \cdot \Gamma(x)} = \frac{\int_0^d \frac{1}{\varepsilon_{np}} \frac{dE_I}{dx} \cdot [n^+(x) + p^+(x)]}{\int_0^d \frac{1}{\varepsilon_{np}} \frac{dE_I}{dx}} = \int_0^d dx \cdot \gamma(x) \cdot [n^+(x) + p^+(x)]$$

Where $\gamma(x)$ is the normalized generation profile:

$$(37)\ \gamma = \frac{1}{E_I} \frac{dE_I}{dx}$$

In conclusion, eq. (36) is the final expression resulting from this model, which is suitable to interpret and fit the experimental CCE degradation shown for example in Figure II-18.

In summary, it requires

    I.   The solution of the continuity and Poisson's equations (11) to evaluate the electrostatics of the device (i.e. the electric field E and the Gunn's field E$^+$) and the drift velocity profiles (v_n and v_p) through eq. (13).

    II.   The solution of the adjoint continuity equations (27) to evaluate the CCE from a single electron/hole pair:

$$(38) \begin{cases} \frac{d}{dx} \cdot \left[D_n \cdot \frac{d}{dx} n^+ \right] + v_n \cdot \frac{d}{dx} n^+ - n^+ \cdot \left[\frac{1}{\tau_n^0} + \alpha_n \cdot \text{Vac} \cdot \Phi \right] - v_n \cdot E^+ - \frac{d}{dx} \left[D_n \cdot E^+ \right] = 0 \\ \frac{d}{dx} \cdot \left[D_p \cdot \frac{d}{dx} p^+ \right] + v_p \cdot \frac{d}{dx} p^+ - p^+ \cdot \left[\frac{1}{\tau_p^0} + \alpha_p \cdot \text{Vac} \cdot \Phi \right] + v_p \cdot E^+ + \frac{d}{dx} \left[D_p \cdot E^+ \right] = 0 \end{cases}$$
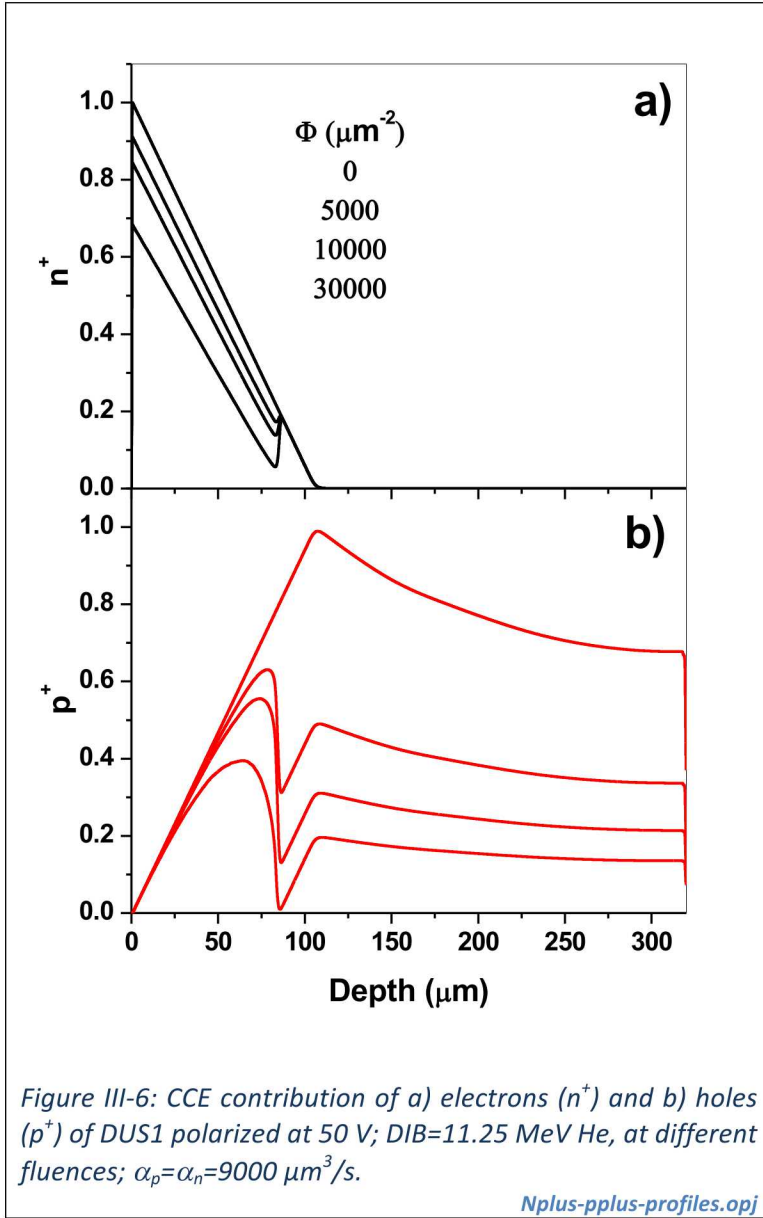
Figure III-6: CCE contribution of a) electrons (n⁺) and b) holes (p⁺) of DUS1 polarized at 50 V; DIB=11.25 MeV He, at different fluences; $\alpha_p=\alpha_n=9000\ \mu m^3/s$.

Nplus-pplus-profiles.opj

with the relevant homogeneous boundary conditions (28). For example, Figure III-6 shows the CCE profiles of electrons (n⁺) and holes (p⁺) in DUS1, biased at 50 V for different level of damage induced by DIB=11.25 MeV He ions, assuming $\alpha_n=\alpha_p=9000$ cm³/s. It is apparent that with increasing fluence, the recombination rate increases, resulting in a drop in the CCE profiles in proximity of the vacancy peak (see Figure II-14).

III.   The knowledge of the vacancy profile Vac(x) resulting, from example, from SRIM simulation (as in Figure II-14)

IV.   The knowledge of the normalized generation profile γ(x) resulting, from example, from SRIM simulation (as in Figure II-15).

The capture coefficients $\alpha_{n,p}$ are therefore the free parameter, which can be extracted by fitting the CCE experimental data with eq. (36).

III.vi.a   Case A. full depletion conditions

If we consider that in our experimental conditions all carrier generation and recombination processes occur within the depletion region of a device (**Assumption VIII**: Full depletion conditions), the dominant charge transport mechanism is the carrier drift caused by the applied electric field whose direction is perpendicular to the electrodes. As a consequence of the carrier generation, transport and recombination occurs only within the depleted region, the diffusion of charge carriers is reasonably assumed to be negligible and the "Gunn's weighting potential" assumes a form of the conventional weighting potential as defined by the "Shockley-Ramo" theorem [Vittone2004], i.e.

$$(39)\ E^+ = \frac{1}{w}$$

In the specific case of a diode, reverse biased, with a depletion layer width of w.

In the following, we will consider only the one-dimensional geometry outlined in Figure II-4. The cathode is located at x=0 and the anode located at x=d is grounded.

In these conditions the stationary adjoint equations (27) can be re-written as follows:

$$(40)\begin{cases} v_n \cdot \dfrac{dn^+}{dx} - n^+ \cdot \left[\dfrac{1}{\tau_n^0} + \alpha_n \cdot \text{Vac} \cdot \Phi\right] - v_n \cdot E^+ = 0 \\ v_p \cdot \dfrac{dp^+}{dx} - p^+ \cdot \left[\dfrac{1}{\tau_p^0} + \alpha_p \cdot \text{Vac} \cdot \Phi\right] + v_p \cdot E^+ = 0 \end{cases}$$

With the following homogeneous boundary conditions:

$$(41)\begin{cases} n^+ (x=0) = n^+ (x=d) = 0 \\ p^+ (x=0) = p^+ (x=d) = 0 \end{cases}$$

Their solution is given by the following expressions [Vittone2016]:

$$(42)\begin{cases} n^+(x) = \int_x^d dy \cdot E^+(y) \cdot \exp\left[-\int_x^y dz \cdot \left(\dfrac{1}{v_n(z)\cdot\tau_n^0(z)} + \alpha_n \cdot \dfrac{\text{Vac}(z)}{v_n(z)} \cdot \Phi\right)\right] \\ p^+(x) = \int_0^x dy \cdot E^+(y) \cdot \exp\left[-\int_y^x dz \cdot \left(\dfrac{1}{v_p(z)\cdot\tau_p^0(z)} + \alpha_p \cdot \dfrac{\text{Vac}(z)}{v_p(z)} \cdot \Phi\right)\right] \end{cases}$$

The total induced charge collected at the sensing electrode is the given by eq. (35)

$$(43)\, Q = q \cdot \int_0^d dx \cdot \Gamma(x) \cdot$$
$$\left\{ \begin{array}{c} \int_x^d dy \cdot E^+(y) \cdot \exp\left[-\int_x^y dz \cdot \left(\dfrac{1}{v_n(z)\cdot\tau_n^0(z)} + \alpha_n \cdot \dfrac{\text{Vac}(z)}{v_n(z)} \cdot \Phi\right)\right] \\ + \\ \int_0^x dy \cdot E^+(y) \cdot \exp\left[-\int_y^x dz \cdot \left(\dfrac{1}{v_p(z)\cdot\tau_p^0(z)} + \alpha_p \cdot \dfrac{\text{Vac}(z)}{v_p(z)} \cdot \Phi\right)\right] \end{array} \right\}$$
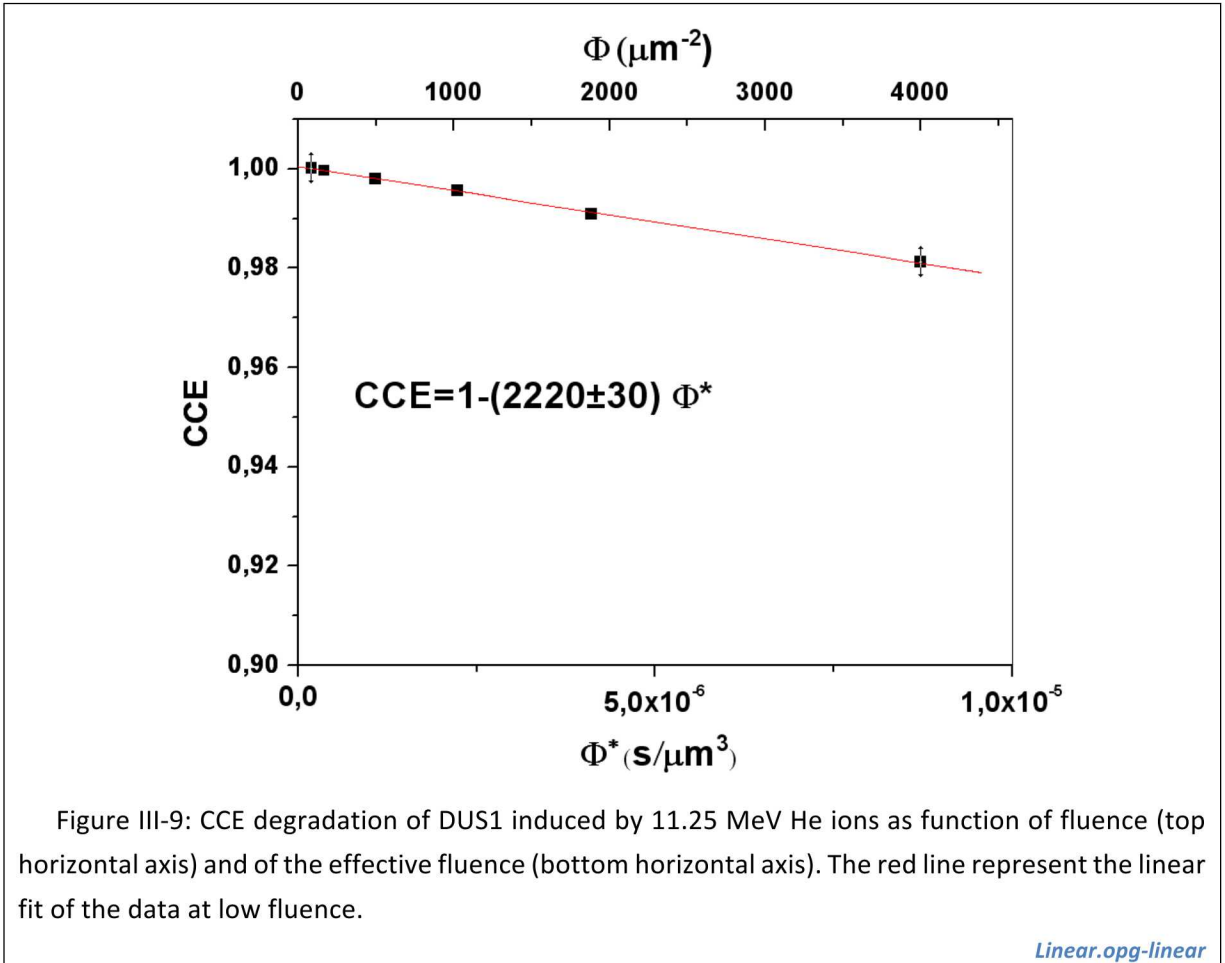
and, the charge collection efficiency is given by (36):

$$(44)\, \text{CCE} = \int_0^d dx \cdot \gamma(x) \cdot \left\{ \begin{array}{c} \int_x^d dy \cdot E^+(y) \cdot \exp\left[-\int_x^y dz \cdot \left(\dfrac{1}{v_n(z)\cdot\tau_n^0(z)} + \alpha_n \cdot \dfrac{\text{Vac}(z)}{v_n(z)} \cdot \Phi\right)\right] \\ + \\ \int_0^x dy \cdot E^+(y) \cdot \exp\left[-\int_y^x dz \cdot \left(\dfrac{1}{v_p(z)\cdot\tau_p^0(z)} + \alpha_p \cdot \dfrac{\text{Vac}(z)}{v_p(z)} \cdot \Phi\right)\right] \end{array} \right\}$$

Furtherly, if the pristine diode (i.e. $\Phi=0$) is assumed (**ASSUMPTION IX**) to have a 100% collection efficiency (i.e. the drift time is much shorter than the carrier lifetime: $\dfrac{1}{v_{n,p}(z)\cdot\tau_{n,p}^0(z)} \rightarrow 0$), the CCE expression reduces to:

$$(45)\, \text{CCE} = \int_0^d dx \cdot \gamma(x) \cdot \left\{ \begin{array}{c} \int_x^d dy \cdot E^+(y) \cdot \exp\left[-\int_x^y dz \cdot \left(\alpha_n \cdot \dfrac{\text{Vac}(z)}{v_n(z)} \cdot \Phi\right)\right] \\ + \\ \int_0^x dy \cdot E^+(y) \cdot \exp\left[-\int_y^x dz \cdot \left(\alpha_p \cdot \dfrac{\text{Vac}(z)}{v_p(z)} \cdot \Phi\right)\right] \end{array} \right\}$$
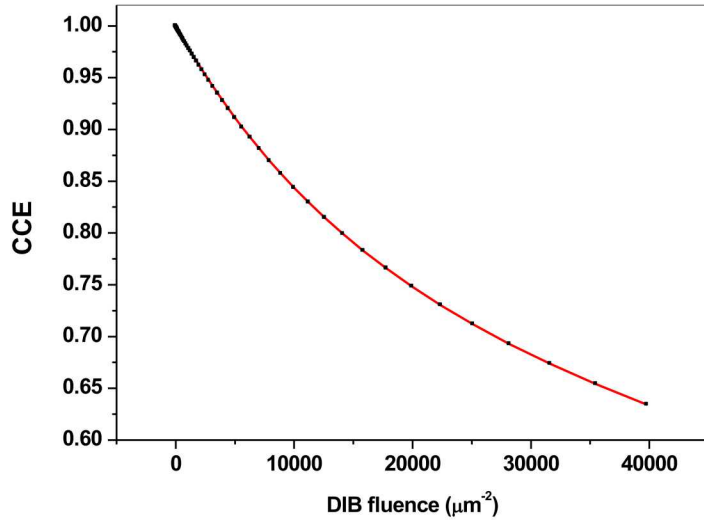
Figure III-7: comparison of the numerical solution (markers) of eq. (36) with the semi-analytical (continuous line) expression (45). DUS1, DIB=11.25 MeV He, PIB=1.4 MeV He, V=50 V, $\alpha_n=\alpha_p$=9000 $\mu m^3/s$.

Comparison-teo-num.ogg

performed with a Finite Element code [COMSOL].

Where E^+ and $v_{n,p}$ are given by the electrostatic analysis of the device (see for example Figure III-1 and Figure III-2) the vacancy (Vac(x)) and the normalized generation ($\gamma(x)$) profiles can be extracted from (for example) SRIM simulations (see Figure II-14 and Figure II-15).

Equation (45) provides the solution of eq. (36) if Assumptions VIII and IX are met.

The validity of the expression can be noticed in Figure III-7, which shows a comparison of the analytical solution given by Equation (45) and the numerical solution of the adjoint equation

Figure III-8: a) Vacancy profile generated by 11.25 MeV He ions in DUS1; b) electron drift velocity in DUS1 at an applied bias voltage of 100 V; c) Gunn's weighting potential in DUS1 at the same applied bias voltage.

Vac-vel-Gunn.opj

III.vi.a Case B. low level of damage

In the case of very low level of damage (**ASSUMPTION X**), which we define as the DIB fluence range in which the CCE degradation follows a linear trend, the exponentials in eq. (45) can be expanded in Taylor series, providing the following approximate expression:

$$(46)\ \text{CCE} = \int_0^d dx \cdot \gamma(x) \cdot \left\{ \begin{array}{c} \int_x^d dy \cdot E^+(y) \cdot \left[1 - \int_x^y dz \cdot \left(\alpha_n \cdot \frac{\text{Vac(z)}}{v_n(z)} \cdot \Phi\right)\right] \\ + \\ \int_0^x dy \cdot E^+(y) \cdot \left[1 - \int_y^x dz \cdot \left(\alpha_p \cdot \frac{\text{Vac(z)}}{v_p(z)} \cdot \Phi\right)\right] \end{array} \right\} =$$

$$(47)\ = 1 - \Phi \cdot \int_0^d dx \cdot \gamma(x) \cdot \left\{ \begin{array}{c} \alpha_n \cdot \int_x^d dy \cdot E^+(y) \cdot \int_x^y dz \cdot \left(\frac{\text{Vac(z)}}{v_n(z)}\right) \\ + \\ \alpha_p \cdot \int_0^x dy \cdot E^+(y) \cdot \int_y^x dz \cdot \left(\frac{\text{Vac(z)}}{v_p(z)}\right) \end{array} \right\} =$$

$$(48) = 1 - \Phi \cdot \int_0^d dz \cdot \text{Vac}(z) \cdot \begin{Bmatrix} \alpha_n \cdot \dfrac{1}{v_n(z)} \int_z^d dy \cdot E^+(y) \cdot \int_0^z dx \cdot \gamma(x) \\ + \\ \alpha_p \cdot \dfrac{1}{v_p(z)} \int_0^z dy \cdot E^+(y) \cdot \int_z^d dx \cdot \gamma(x) \end{Bmatrix}$$

here, we have adopted the following definitions:

$$(49) \int_0^d dx \cdot \gamma(x) = \int_0^d dy \cdot E^+(y) = 1$$

Figure III-9: CCE degradation of DUS1 induced by 11.25 MeV He ions as function of fluence (top horizontal axis) and of the effective fluence (bottom horizontal axis). The red line represent the linear fit of the data at low fluence.

Linear.opg-linear

Equations (47)-(48) provide the evidence for different roles played by the two carriers. To simplify, let us consider a vacancy profile localized at x=x0, i.e. $V(x)=V_0\cdot\delta(x-x_0)$. If the generation profile extinguishes at a depth x<x0, i.e. $\gamma(x)= \theta(x_0-x)$, where θ is the Heaviside step function [W6], it is apparent that only electrons, travelling from 0 to d, cross the damaged region and might suffer recombination. On the contrary, recombination/trapping of holes moving in the opposite direction, towards the front electrode and crossing the low damaged layer corresponding to the tail of the vacancy distribution, is negligible because they do not cross the highly damaged region. This simple consideration provides the basis of the experimental protocol described in section II, which allows the recombination/trapping of both types of charge carriers (electrons and holes), that contribute to the CCE degradation, to be distinguished [Vittone2016]. Moreover, if shallow PIBs are considered, the generation profile $\gamma(x)$ estinguishes at a very short distance from the surface. In this case (single carrier charge induction),

the hole contribution (the second term in the curly bracket) is negligible and the CCE expression simplify in the following expression:

$$(50)\ \text{CCE} \approx 1 - \Phi \cdot \alpha_n \cdot \int_0^d dz \cdot \frac{\text{Vac(z)}}{v_n(z)} \cdot \varphi^+(z) = 1 - \alpha_n \cdot \Phi^*$$

The nested triple integrals in eq. (45) collapse into a single integral, which involves both the drift velocity of the majority carriers ($v_n(z)$), the vacancy profile (Vac(z)) and the electrostatics of the device through Gunn's weighting potential $\varphi^+(z)$. Under the assumption of very shallow PIBs, the CCE degradation as function of the DIB fluence follows a linear trend.

The term Φ^* in eq. (50) is the effective DIB fluence:

$$(51)\ \Phi^* = \Phi \cdot \int_0^d dz \cdot \frac{\text{Vac(z)}}{v_n(z)} \cdot \varphi^+(z)$$

The slope of the linear fit of the experimental data plotted as function of Φ^* provides the capture coefficient α_n (see Figure III-9).

III.vi.c Case C. The displacement damage dose

In the case of low level of damage, eq. (48) correlates this model with the approach based on the *"displacement damage dose"* proposed by Messenger et al. [Messenger1999], as described in [Vittone2016].

Actually, adopting the following assumption:

Assumption XI: the constant vacancy profile up to a depth R<d:

$$\text{Vac(x)} = \theta(R - x) \cdot \frac{V_T}{R},$$

where θ is the Heaviside step function [W6] and V_T is the total number of vacancies, i.e. Vac(x) is the constant average value of the vacancy profile, the linear degradation of CCE can be expressed as follows:

$$(52)\ \text{CCE} = 1 - \Phi \cdot \frac{V_T}{R} \cdot \int_0^d dz \cdot \left\{ \begin{array}{c} \alpha_n \cdot \frac{1}{v_n(z)} \int_z^d dy \cdot E^+(y) \cdot \int_0^z dx \cdot \gamma(x) \\ + \\ \alpha_p \cdot \frac{1}{v_p(z)} \int_0^z dy \cdot E^+(y) \cdot \int_z^d dx \cdot \gamma(x) \end{array} \right\}$$

This expression can be connected to the phenomenological concept of "displacement damage dose" D_d proposed by Messenger et al. [Messenger1999,2005, Summers1995]. The displacement damage dose is defined as the displacement damage energy deposition per unit mass of material and can be calculated as the product of the particle fluence and the respective non-ionizing energy loss (NIEL) of the particle. The NIEL value is an estimate of the rate of energy loss due to atomic displacements as the particle traverses a material. In the framework of the NIEL theory, the CCE decreases with the accumulated displacement damage dose (D_d) through the following simple expression:

$$(53)\ CCE = 1 - K_{ed} \cdot D_d$$

where K_{ed} is the equivalent damage factor defining the rate of linear decrease. The units of D_d are typically $eV \cdot cm^2 \cdot g^{-1}$.

The displacement damage dose D_d is defined as follows [Messenger1999]:

$$(54)\, D_d = \left(\frac{M}{\rho_M} \cdot \frac{V_{Tot}}{R} \right) \cdot \Phi$$

where ρ_M is the mass density of the irradiated material (2.32 g·cm^{-3} in silicon) and M is the average energy necessary to produce a vacancy (see List of Symbols in section VII).

The displacement damage dose can be calculated from SRIM simulations, considering the following expression:

$$(55)\, M = \left(\frac{T_d}{0.4} + 2 \right)$$

Where 2 is added to allow for binding energy loss that SRIM assigns to each vacancy and T_d is the threshold energy for atomic displacement. In silicon, considering a typical value of T_d=21 eV [Corbett1965], M=54.5 eV.

By comparing eq. (53) and eq. (48), through the definition (54), we obtain the following analytical expression for the equivalent damage factor:

$$(56)\, K_{ed} = \frac{\rho}{M} \cdot \int_0^d dz \cdot \left\{ \begin{array}{c} \alpha_n \cdot \frac{1}{v_n(z)} \int_z^d dy \cdot E^+(y) \cdot \int_0^z dx \cdot \gamma(x) \\ + \\ \alpha_p \cdot \frac{1}{v_p(z)} \int_0^z dy \cdot E^+(y) \cdot \int_z^d dx \cdot \gamma(x) \end{array} \right\}$$

This expression explicitly shows the dependence of the equivalent damage factor K_{ed} on:

    a) the electrostatics of the device due to the presence of the Gunn's field E^+,

    b) the carrier transport due to the presence of the drift velocities $v_{n,p}$

    c) the recombination features due to the presence of the capture coefficients $\alpha_{n,p}$

    d) the ion probe ionization profiles due to the presence of normalized generation profile γ

If the experimental conditions (i.e. device polarization and ion probe) are maintained constant as well as the ranges of the damaging ions, under Assumptions VIII-X, the NIEL approach can effectively correlate the CCE degradation of an electronic device induced by different radiation sources or energies, as demonstrated in [Pastuovic2011,2013]. If one or more of these conditions are not fulfilled, the complete expression given by eq. (35) has to be used.

IV. THE PROTOCOL FOR THE ANALYSIS OF THE CCE DEGRADATION DATA

Data analysis of the CCE degradation curves, as illustrated in Figure II-18, is aimed to extract the capture coefficients $\alpha_{n,p}$, which can be considered qualifiers for assessing the relative radiation hardness of semiconductors. The evaluation of these parameters is performed by fitting the experimental data with equation (36) derived from the general model. In general, it requires the numerical solution of the differential equations (38) or their semi-analytical solution given by eq. (45) if **Assumption VIII** is met.

The highly non-linear nature of these equations and the relevant integrals, prevents any analytical approach of the fitting procedure and the following methodology can be adopted.

The capture coefficients can be evaluated by the method of least squares [Brandt1978], which of all statistical methods is the one most widely used in practical problems. It consists in the minimization, with respect to the unknown parameters α_n, α_p, of the matrix M of the sum of the square of the residuals normalized by the uncertainty $\sigma(i)$ of the i-th measurement:

$$(57) \quad M\left(\alpha_n, \alpha_p\right) = \sum_{i=1}^{N} \left[\frac{CCE_{exper}(i) - CCE_{model}(i)}{\sigma(i)} \right]^2$$

i.e. the sum of the squares of the difference between the experimental data and the values predicted by the model. CCE_{exper} is the CCE data extracted from the N regions (typically 9) irradiated at different fluences (see Figure II-13), $\sigma(i)$ is the uncertainty from the peak fitting of the CCE spectra shown in Figure II-13 and CCE_{model} is the theoretical CCE evaluated from eq. (36).

The function $M(\alpha_n, \alpha_p)$ can be interpreted geometrically, since it defines a hypersurface in a three dimensional space, spanned by the parameters α_n and α_p. The function $M(\alpha_n, \alpha_p)$ can be evaluated systematically using a lattice of points over the region of the parameter (α_n, α_p) plane and searching for the point, identified by the coordinates (α_n, α_p), which yields the smallest value of M.

Although this rough method can potentially lead to local minima, it was used because

        a) it is easy to implement in spite of the complex non-linear CCE expression in eq. (36)
        b) it is possible to combine multiple fitting routines.

Moreover, the physical meaning of the fitting parameters (α_n, α_p) can help to identify absolute minima and therefore the parameters, which provide the best fit of the experimental data, as discussed later.

To effectively implement this minimization strategy, it is opportune to start from a first rough estimate of (α_n, α_p) in order to limit the parameter space. For example, it can be recommended to use the parameter relevant to majority carriers (electrons for DUS1) obtained by using shallow PIBs as described in Figure III-9. In this specific case, the hole contribution can be neglected and M is a function of only α_n, leading, under **ASSUMPTION X**, to a traditional linear fit. In general, it is recommended to extract starting value of the parameters (defined in eq. (33)) from the capture cross sections of defects and of the k-factor (of the order of unity) available in literature [Pastuovic2011, 2013, Vittone2016]. This systematic scanning in the parameter space to find the minimum of M is both a time and a computational resource consuming process.

It is worthwhile noticing that the $\alpha_{n,p}$ parameters are fluence scaling factors separately entering the equations relevant to electrons and holes, respectively

Therefore, it is possible to optimize the minimization algorithm to calculate CCE_{model}, adopting the following approach:

        a) The solution of equations (36) at different DIB fluences, is calculated separately for electrons ($CCE^n_{model}(\alpha^{Max}_n \cdot \Phi)$) and holes ($CCE^p_{model}(\alpha^{Max}_p \cdot \Phi)$) using the highest values of the parameters (α^{Max}_n and α^{Max}_p), which define the boundary of the parameter space.

        b) For any coordinate of the lattice point over the region of the parameter (α_n, α_p) plane, CCE^n_{model} and CCE^p_{model} are calculated, at different DIB fluence, by separately interpolating the $CCE^n_{model}(\alpha^{Max}_n \cdot \Phi)$ and $CCE^p_{model}(\alpha^{Max}_p \cdot \Phi)$ curves.

As an example, let us consider the case of DUS1 irradiated with (DIB=) 11.25 MeV He ions; the damage is probed with (PIB=) 1.4 MeV He ions (this is the case already discussed in III.vi.a   Case B. low level of damage).

Figure IV-1 shows the $CCE^n_{model}(\alpha^{Max}_n \cdot \Phi)$ and $CCE^p_{model}(\alpha^{Max}_p \cdot \Phi)$, calculated by numerically solving equations (36), using ($\alpha^{Max}_n = \alpha^{Max}_p = 12000$ μm^3/s). As expected, being the PIB very shallow (range about 5 μm), the hole contribution to the CCE is negligible (0.015) and the hole sensitivity to the much deeper damage induced by DIB is negligible. Actually, since the generation curve is shallower than the damage profile, majority carriers (electrons) drift towards the anode (located at x=320 μm) and cross the highly damaged region located at the vacancy peak, where the recombination probability is the highest (see Figure III-5). On the other hand, minority carriers (holes) drift towards the cathode (x=0). Since their trajectories develop along the tail of the vacancy profile, the traps induced by radiation damage very marginally influence their lifetime.
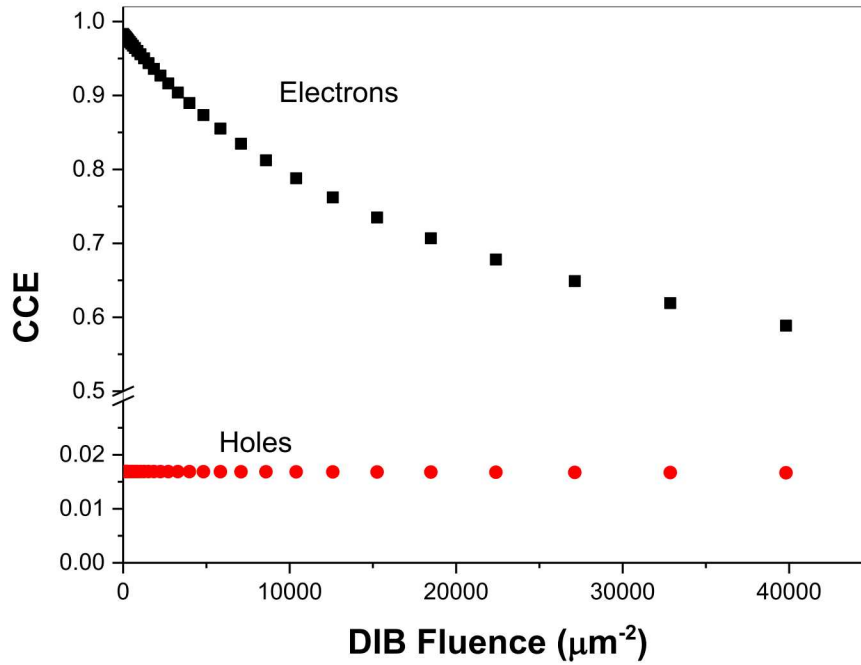
Figure IV-1: CCE degradation curves of electrons (CCE$^n_{model}$) and holes (CCE$^p_{model}$) of DUS1. DIB=11.25 MeV He ions, PIB=1.4 MeV He ions, Applied bias voltage = 50 V, $\alpha^{n,p}$=12000 μm^3/s.

FinalFit.opj[TECDOC]gnp1

The $CCE^n_{model}(\alpha^{Max}_n \cdot \Phi)$ curves in Figure IV-2 have been calculated from the interpolation of the $CCE^n_{model}(\alpha^{Max}_n \cdot \Phi)$ at the experimental values of fluences. By comparing these curves with the experimental data, it is apparent that for α_n = 1680 μm^3/s the theoretical curve fits well the experimental data. This is clearly shown in Figure IV-3, which reports the behaviour of the M function vs. α_n. The minimum of the squared sum of residuals falls to α_n = 1680 μm^3/s.
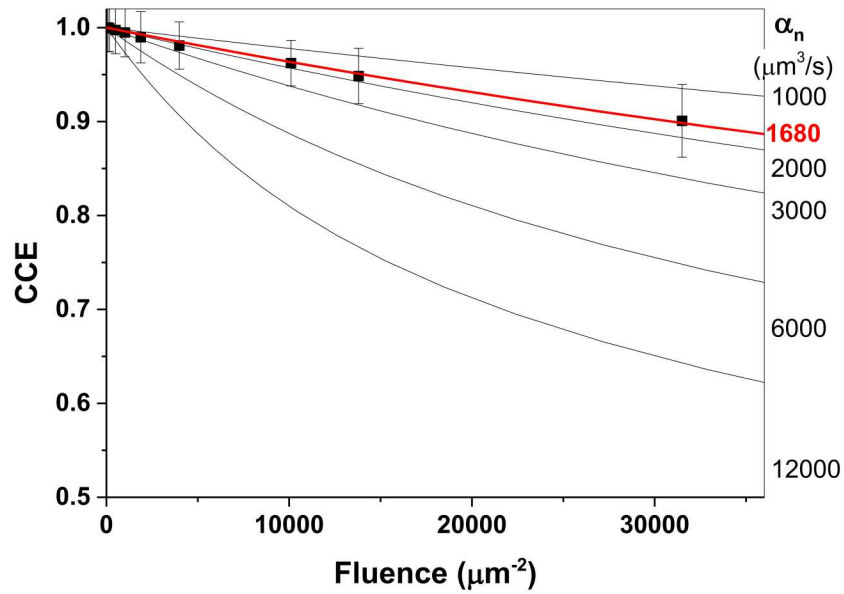
Figure IV-2: CCE^n_{model} for different values of α_n as function of the DIB fluences; continuous lines. Markers: experimental CCE data; PIB=1.4 MeV He; V_{bias}= 50 V.

FinalFit.opj[TECDOC]diffalphan
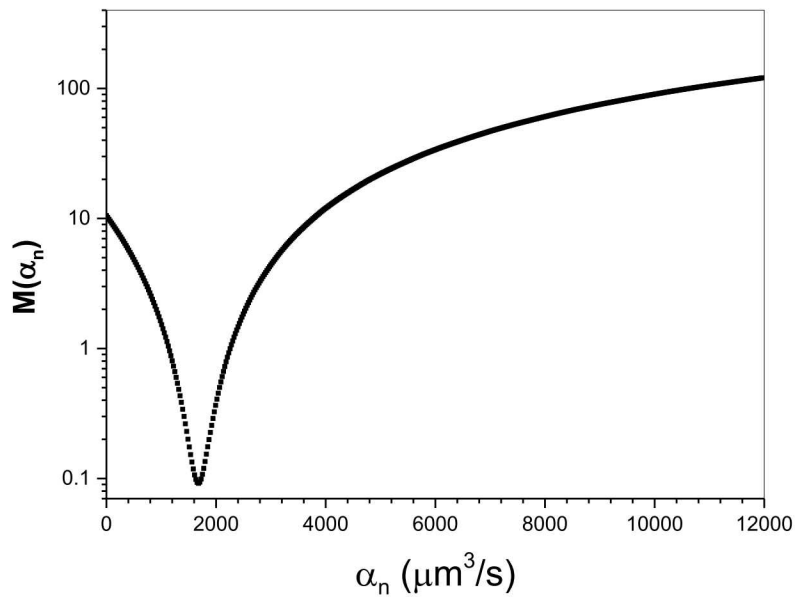
Figure IV-3: Squared sum of residuals as function of different values of α_n

FinalFit.opj[TECDOC]residuals
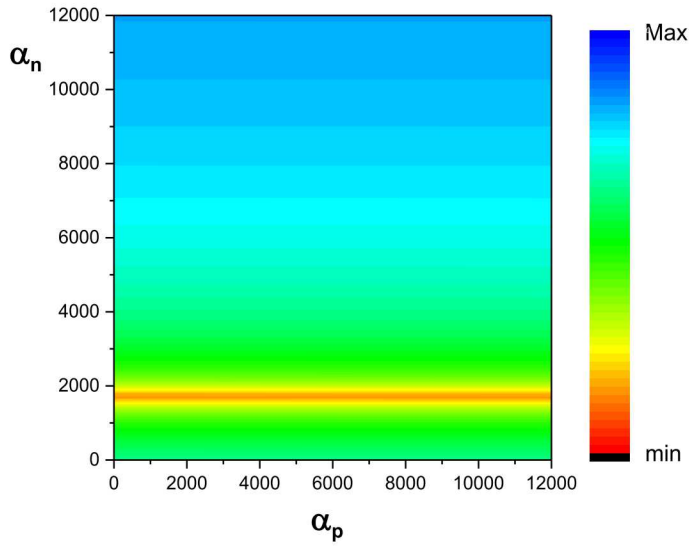
Figure IV-4: M(α_n, α_p) contour plot; DIB=11.25 MeV He ions, PIB=1.4 MeV He ions, Applied bias voltage = 50 V,

COMSOL/FinalFit.opj[Calculus]gexample1

A similar procedure can be extended to two dimensions, considering the function M in the (α_n, α_p) parametric space. The hypersurface M can then be represented by a contour-plot as shown in Figure IV-4.

Again, the M hypersurface shows minima corresponding to α_n=1680 μm^3/s, independently from the α_p values, since the minima locus lies along a line parallel to the horizontal axis.

In the case of more penetrating PIBs, both carriers play a role in the degradation of CCE. For example, let us consider the experiment carried out on DUS1 to analyse the CCE degradation induced
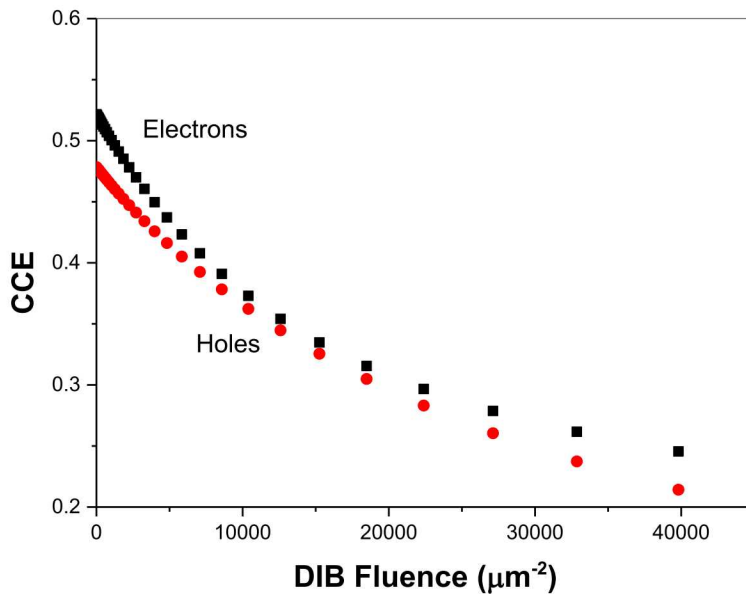
Figure IV-5: CCE degradation curves of electrons (CCE$^n_{model}$) and holes (CCE$^p_{model}$) of DUS1. DIB=11.25 MeV He ions, PIB=11.25 MeV He ions, Applied bias voltage = 50 V, $\alpha_{n,p}$=12000 μm^3/s.

FinalFit.opj[TECDOC]gnp2

by (DIB=11.25 MeV He ions) and measured using the same ions (PIB=DIB). In this case, the contributions to the CCE degradation of electrons and holes is shown in Figure IV-5 assuming α_n=α_p=12000 μm^3/s.
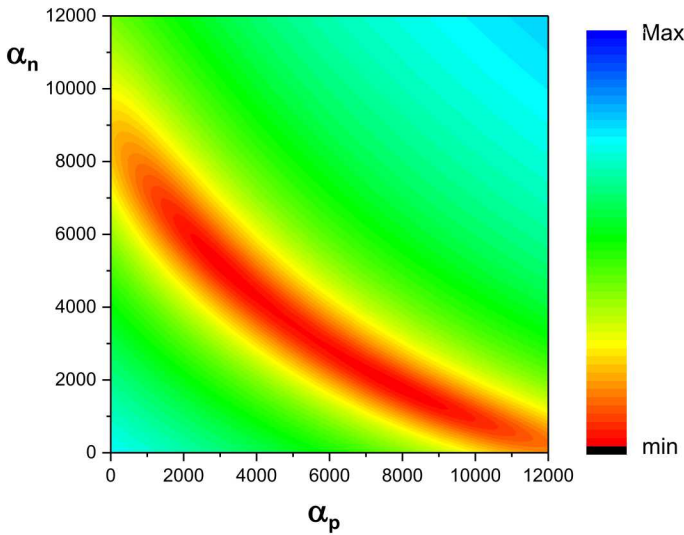
Figure IV-6: M(α_n,α_p) contour plot; DIB=11.25 MeV He ions, PIB=11.25 MeV He ions, Applied bias voltage = 50 V .

COMSOL/FinalFit.opj[Calculus]gexample2

Figure IV-6 shows the contour plot of the M hypersurface. It is apparent that the minima locus crosses the whole parameter space and is not parallel to the horizontal or vertical axis; this fact indicates that the best fit of the experimental data is given by a combination of both the majority and minority carrier contributions. In this specific case, the minimum of the M function is obtained for α_n=1680 μm^3/s and α_p=7920 μm^3/s, which define a theoretical CCE curve, which fits well the experimental data (Figure IV-7).

However, it is worth noticing that the minima locus is almost flat, as shown in the three-dimensional plot of the M hypersurface, i.e. the sum of the squared residuals does not remarkably vary within this hyperbolic-like minima-locus (Figure IV-8).

Obviously, the two measurements, carried out with different PIBs, should be consistent. Therefore, we have combined the two M functions, relevant to the two PIBs, in order to extract the capture coefficients (α_n, α_p), which minimize the combined squared sum of residuals, i.e.

$$(58)\ M=M(PIB=1.4\ MeV\ He) + M(PIB=11.25\ MeV\ He)$$

From the graphical point of view, this operation corresponds to the overlapping of the two contour plots shown in Figure IV-4 and Figure IV-6 as shown in Figure IV-9. The intersection of the two minima-loci identify a unique minimum, which is located at α_n=1560 μm^3/s and α_p=8160 μm^3/s. These values, determine the simultaneous best fit of the CCE degradation curves relevant at the two PIBs (see Figure IV-10).

The same procedure can then be extended to other conditions; for example, using PIB=2.3 MeV H at 50 V of applied bias voltage, the M contour plot and the relevant curve fitting the experimental data are shown in Figure IV-11. The final fitting procedure performed with three different PIBs on the experimental CCE degradation data of DUS1 polarized at 50 V are shown in Figure IV-12 The best fitting curves have been calculated from the model using the following parameters: α_n=1440 μm^3/s, α_p=7740 μm^3/s. The theoretical curves resulting from the model, fit well the experimental data for low values of DIB fluence.
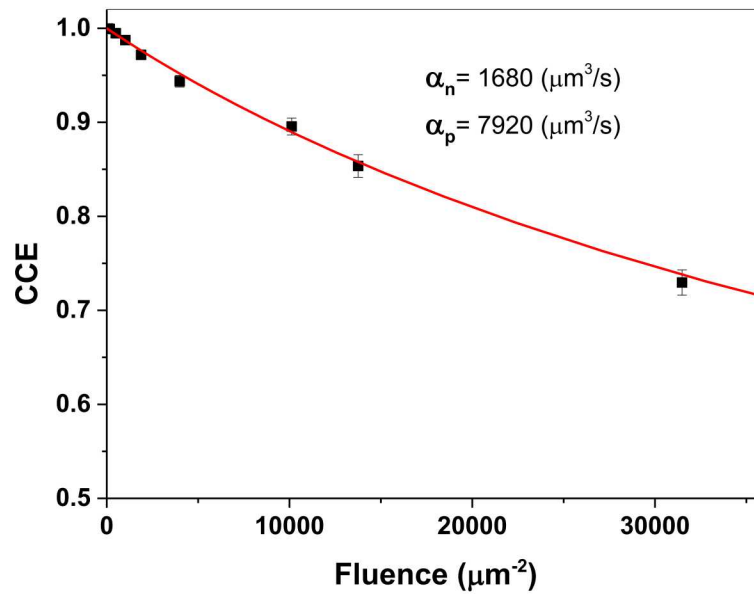
Figure IV-7: best fit (α_n=1680 μm^3/s, α_p=7920 μm^3/s, continuous line) of the data (markers) for the experiment carried out on DUS1 using the conditions detailed in Figure IV-5.

FinalFit.opj[Calculus]gFit1
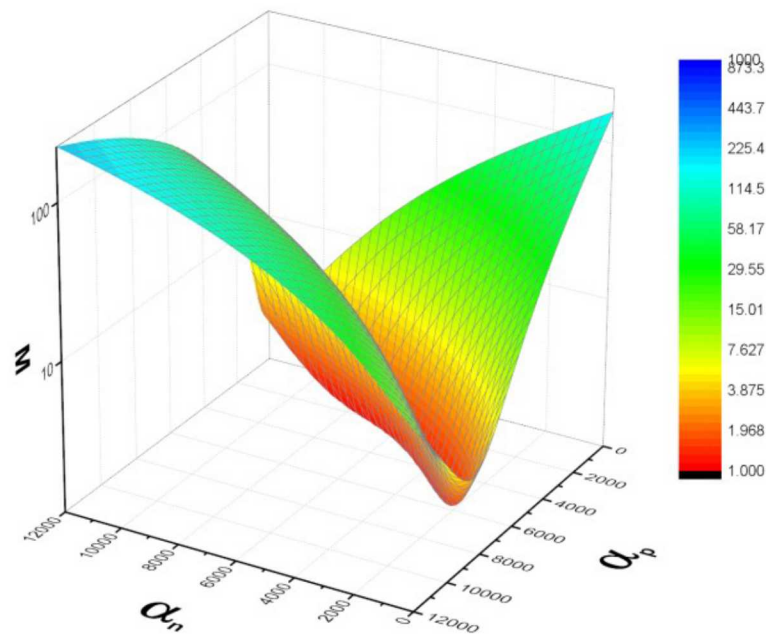
Figure IV-8: three dimensional color fill map of the M hyper-surface shown in Figure IV-6.

FinalFit.opj[Calculus]g3D

The last point, at the highest fluence slightly deviates from the theoretical prediction.

The corresponding fluence (in this case $\Phi = 3 \cdot 10^4$ µm^{-2}) indicates the validity limit of the model, in particular with respect to **Assumption VII**.

The procedure can be extended to other applied bias potentials. Figure IV-13 shows the results of the above described procedure applied to the CCE degradation data measured at an applied bias voltage of 100 V.

Finally, Figure IV-14 summarizes the whole analysis. The residual maps are shown for all the experimental conditions (PIBs and bias voltages). The map in the centre is the residual map given by the convolution of all the lateral maps.

The capture coefficients are extracted from the minimum of the M function given from the combination of the squared residuals calculated for the measurements at bias voltages of V=50 V and 100 V (see Annex). These capture coefficients are used to calculate, through eqs. (36) or (45), the theoretical CCE degradation curves, which well fit the experimental data acquired in any experimental condition (Figure IV-15).

The best fit is given at the following values: α_n=1600 µm^3/s and α_p=8200 µm^3/s; the solid lines are the best fits obtained by the abovementioned procedures considering different PIBs and different bias voltages.

IV.i Error Budget

The evaluation of the measurement uncertainty is required to complete the analysis. The uncertainty can be determined from the calculation of the error matrix Err, which is the inversion of the Hessian (H) of the M function. The Hessian matrix is the second derivative matrix of the M function with respect to the free parameters α_n and α_p evaluated at the best parameter values (the M function minimum). The diagonal elements of the error matrix are the squares of the individual parameter errors, including the effects of correlations with the other parameters.

$$(59)\, \mathrm{H}\big(\alpha_n, \alpha_p\big) = \begin{pmatrix} \dfrac{\partial^2 \mathrm{M}}{\partial \alpha_n^2} & \dfrac{\partial^2 \mathrm{M}}{\partial \alpha_n\, \partial \alpha_p} \\ \dfrac{\partial^2 \mathrm{M}}{\partial \alpha_n\, \partial \alpha_p} & \dfrac{\partial^2 \mathrm{M}}{\partial \alpha_p^2} \end{pmatrix}; \; \mathrm{Err}\big(\alpha_n, \alpha_p\big) = \mathrm{H}^{-1}\big(\alpha_n, \alpha_p\big)$$

The inverse of the error matrix, the second derivative matrix or Hessian, has as diagonal elements the second partial derivatives with respect to one parameter at a time. These diagonal elements are not therefore coupled to any other parameters, but when the matrix is inverted, the diagonal elements of the inverse contain contributions from all the elements of the second derivative matrix, which is "where the correlations come from" [W11]..
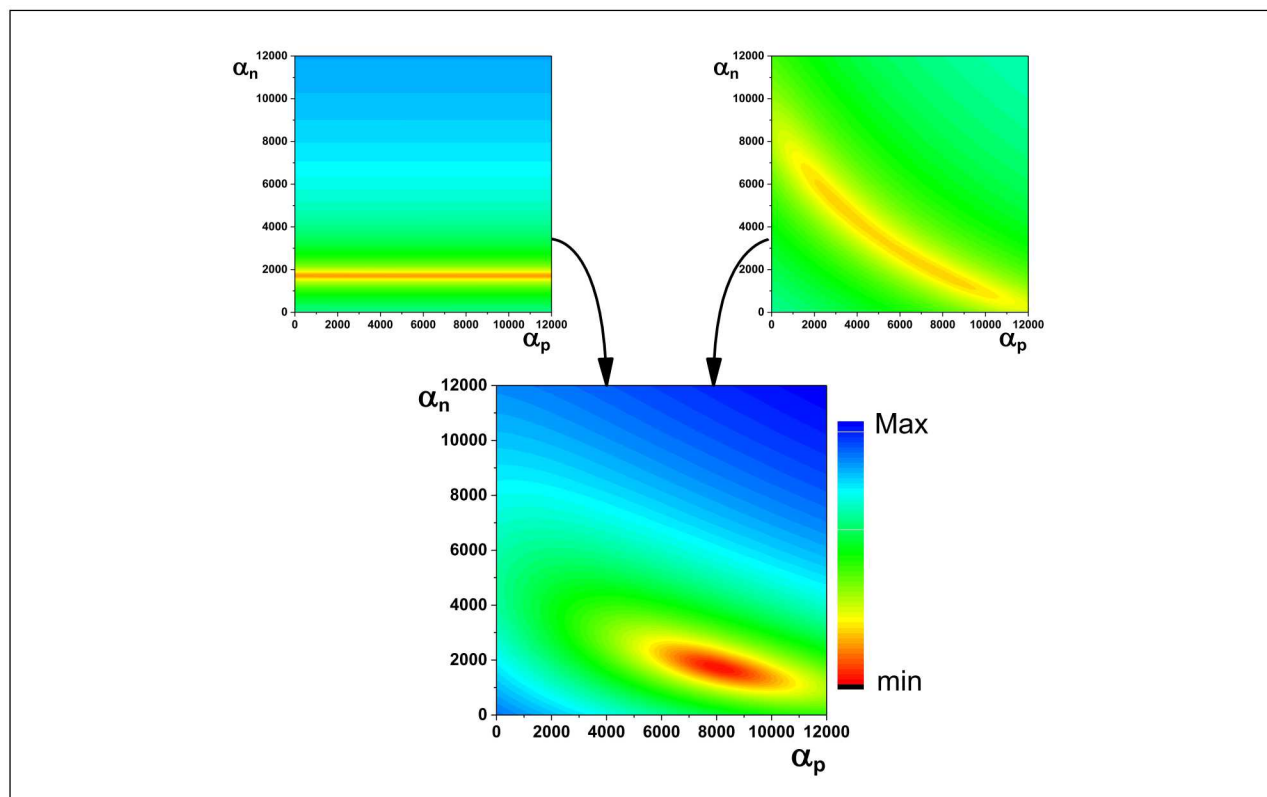
Figure IV-9: contour plot of the M hypersurface defined by eq. (58)

FinalFit.opj[Calculus]gMRES
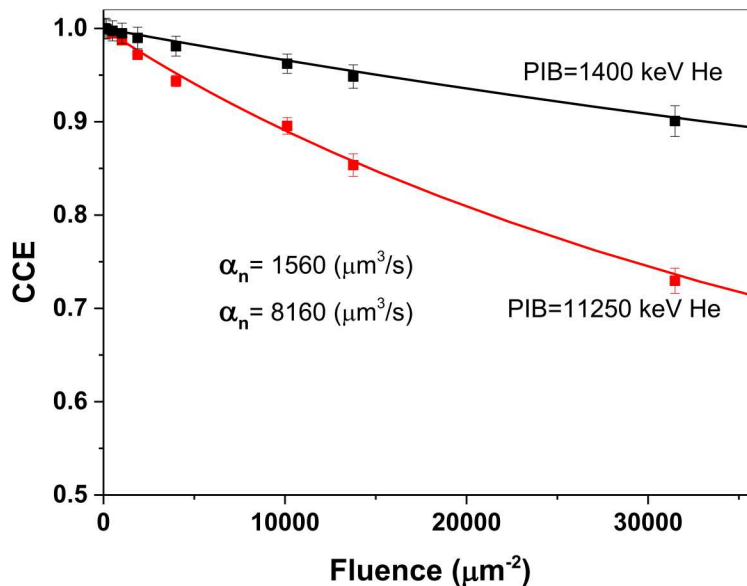
Figure IV-10: CCE degradation curves for two different PIBs. Continuous lines calculated using α_n=1560 μm^3/s, α_p=8160 μm^3/s. Markers: experimental data
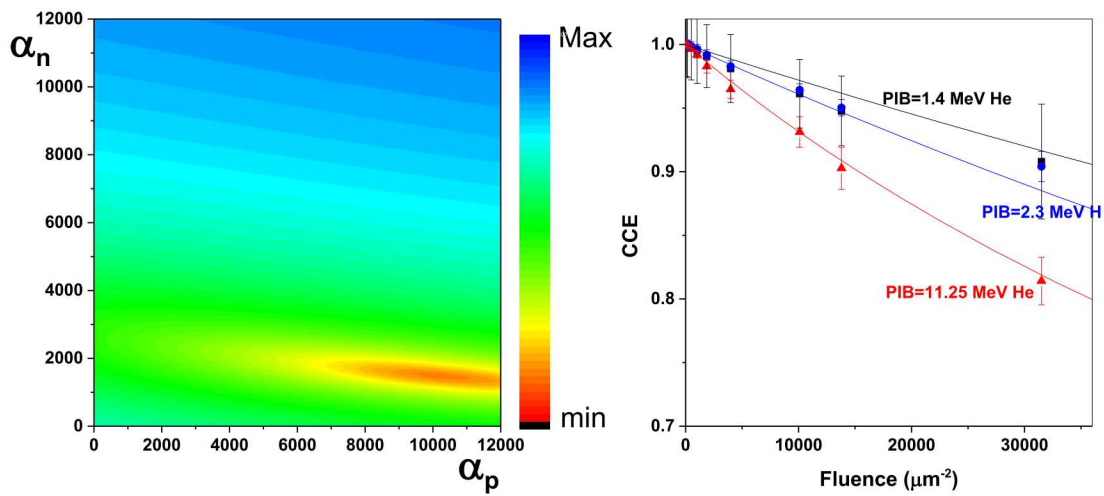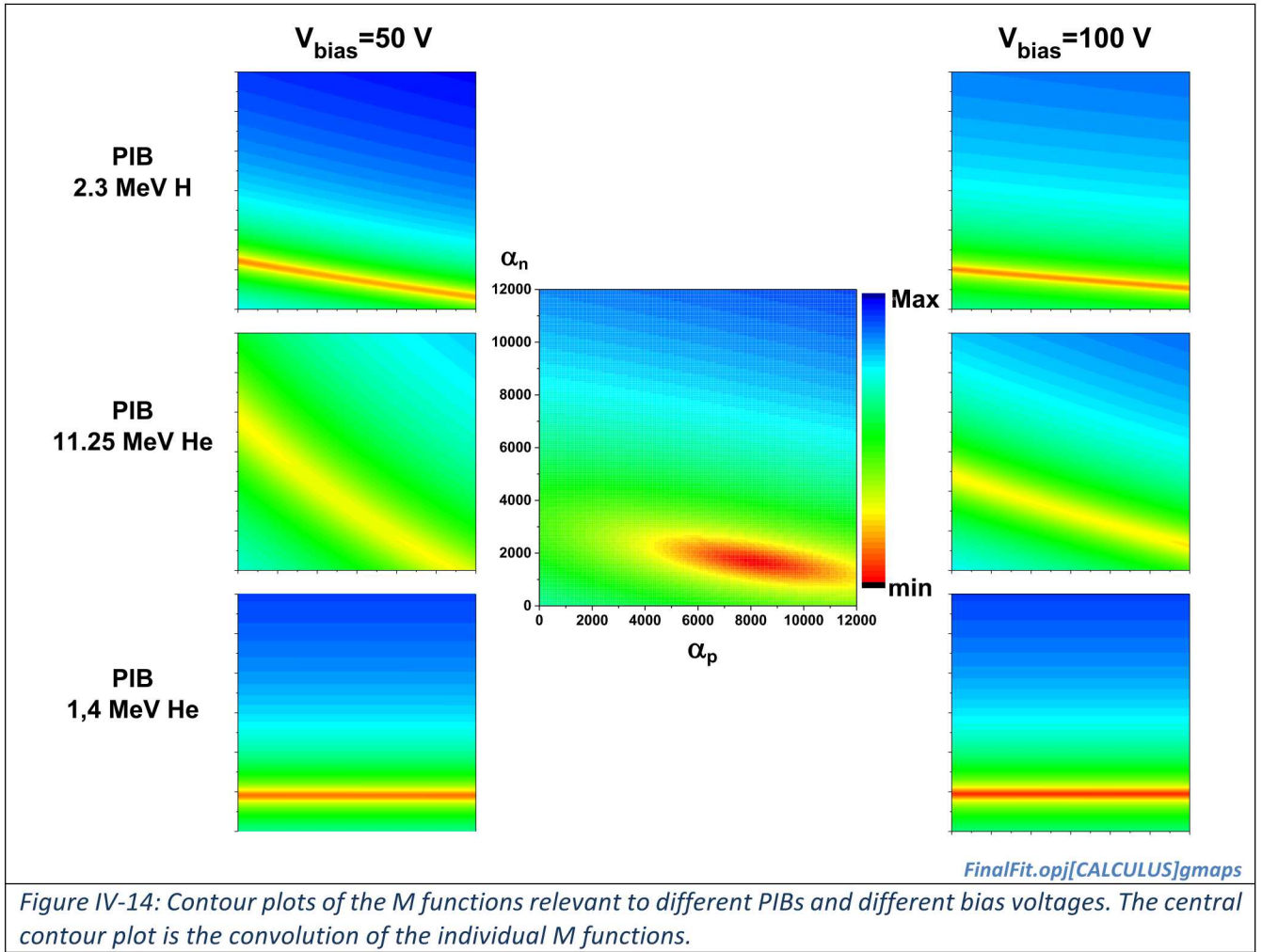
FinalFit.opj[TECDOC]gFit2
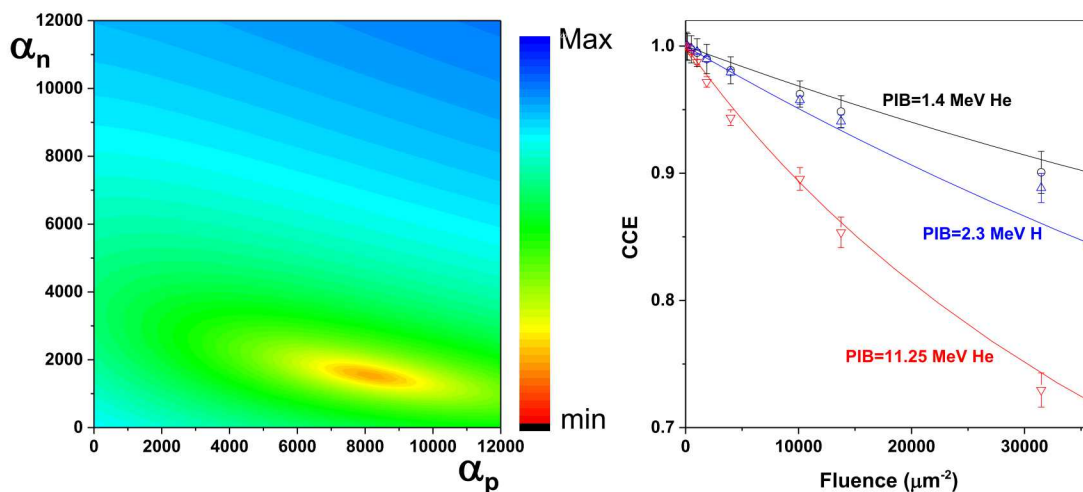
Figure IV-11: Contour plot of the M function (left) and best fitting curves (continuous lines, α_n=1440 μm^3/s, α_p=8040 μm^3/s) of the experimental data (markers), relevant to different PIBs; CCE degradation study of DUS1 polarized at 50 V.

FinalFit.opj[CALCULUS]example5
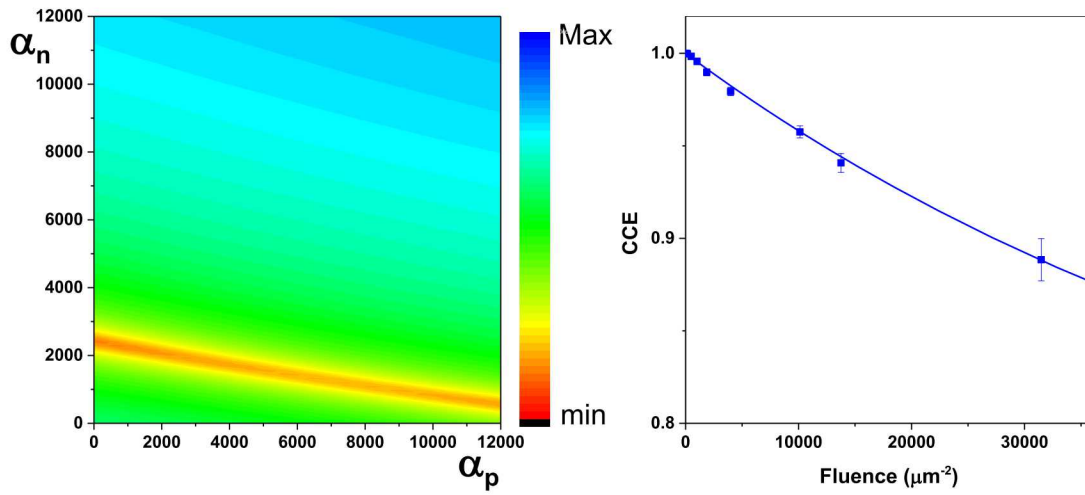
Figure IV-12: (left) Contour plot of the M function; (right) best fit (continuous line) of the experimental data (markers). PIB=2.3 MeV H, DIB=11.25 MeV He, Bias voltage = 50 V; αn=2280 µm3/s.

FinalFit.opj[Calculus]example4

Figure IV-13: Contour plot of the M function (left) and best fitting curves (continuous lines, α_n=1320 µm^3/s, α_p=10440 µm^3/s) of the experimental data (markers), relevant to different PIBs; CCE degradation study of DUS1 polarized at 100 V.

FinalFit.opj[CALCULUS]example6

Figure IV-14: Contour plots of the M functions relevant to different PIBs and different bias voltages. The central contour plot is the convolution of the individual M functions.

The Hessian and the Err matrices in the case of study are the following:

$$(60)\ H\big(\alpha_n, \alpha_p\big) = \begin{pmatrix} 9.59743 \cdot 10^{-5} & 1.1864 \cdot 10^{-5} \\ 1.1864 \cdot 10^{-5} & 2.52317 \cdot 10^{-6} \end{pmatrix};$$

$$(61)\ Err\big(\alpha_n, \alpha_p\big) = \begin{pmatrix} 24440 & -114163 \\ -114163 & 929612 \end{pmatrix};$$

Leading to the following final measurements of the two parameters:

$$(62)\ \begin{aligned} \alpha_n &= (1600 \pm 160)\mu m^3/s \\ \alpha_p &= (8200 \pm 960)\mu m^3/s \end{aligned}$$

The correlation coefficient is given by

$$(63)\ corr = \frac{Err_{12}}{\sqrt{Err_{11} \cdot Err_{22}}} = -0.758$$
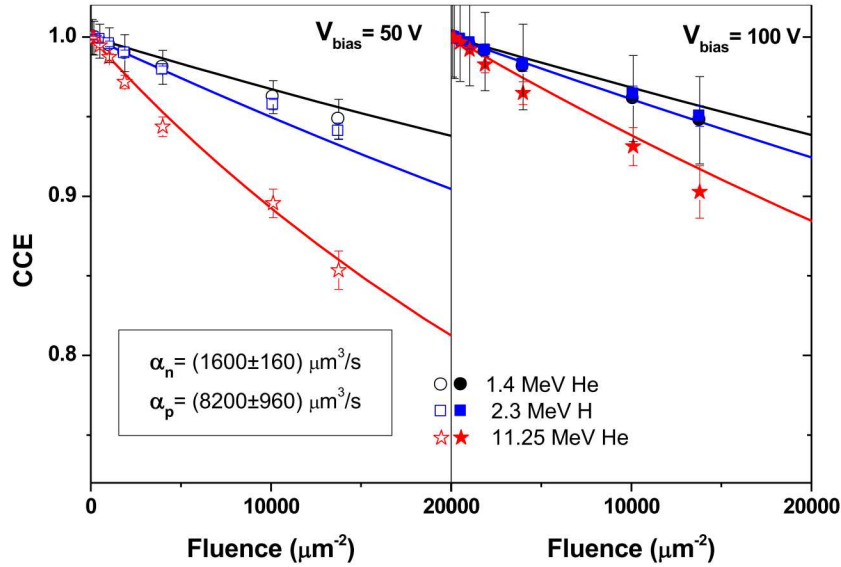
Figure IV-15: final evaluation of the capture coefficient α_n and α_p evaluated by merging the analysis carried out at 100 V (filled markers) and 50 V (open markers) with different PIBs and limited to fluences < $2\cdot10^{12}$ ions/cm^2.

FinalFit-Zoom.opj[TECDOC]gfit6

Short discussion about the meaning of the correlation coefficient is following. The model adopted to interpret the CCE degradation is based on the assumption that the induced charge is given by the independent contributions of electrons and holes (eq. (35)), therefore, (α_n, α_p) which are assumed to be not correlated (i.e. the correlation coefficients should be null). However, the final expression of the fitting curve (e.g. eq. (38) or (47)) involves both the contributions of the carriers, which have common terms given by the normalized generation profile γ (eq. (37)) and the vacancy distribution entering in the integral and in the expression of the lifetime (eqs. (30) - (33)), respectively. Therefore, the final general expression (eq. (38)) naturally correlates the two contributions. As an example, in the case of shallow PIBs (e.g. see Figure IV-4) there is no correlation between α_n and α_p because the generation profile γ makes negligible the contribution of minority carriers, whereas in the case of highly penetrating PIBs (Figure IV-6) both the carriers play a role and the residual map clearly show a correlation. In principle, if an additional experiment could be carried out using shallow PIBs incident on the back electrode, only the minority carrier contribute to CCE degradation, generating a residual map similar to that represented in Figure IV-4, but rotated by 90°. In this case, by combining the two orthogonal residual maps (one given mainly by the contribution of electrons, the other by the contribution of holes) the resulting minima locus will be an axis symmetrical ellipsis (i.e. with a null correlation coefficient). If PIBs of different ranges always irradiate the frontal electrode, as in the examples reported here, tilted ellipses (i.e. non-null correlation coefficients) are unavoidable.

V.   CONCLUSIONS

The F11016 IAEA Coordinated Research Project, involving 14 institutes from 13 member states and running from Dec. 2011 to Nov. 2015, was aimed to promote the utilization of ion accelerators for studying and modelling of radiation induced defects in semiconductors and insulators. One of the expected outcomes of this CRP was to develop a methodology, accessible to any laboratory equipped with ion accelerators and standard electronics for detection of ionizing particles, to measure and interpret the charge collection efficiency degradation in semiconductors provoked by displacement damage effects induced by ion irradiation.

This report details both the experimental and the theoretical aspects of this methodology. It describes all the phases of an experiment carried out on a commercial silicon photodiode, which is commonly used within the ion beam community, as a low-cost particle detector for certain applications not requiring the highest energy resolution provided by the highest spectroscopic grade silicon detectors.

The experimental protocol is based on the use of energetic accelerated ions in the MeV energy range, which play a dual role: (1) as damaging agents to generate defects in active semiconductor material of the electronic device (in our case a diode) and (2) as probes to measure the effect of low level radiation damage on the CCE, as the main feature defining the electronic response of tested/irradiated semiconductor devices. The low level damage is assumed to be an accumulation of simple point defects (vacancies or interstitials or their complexes with atoms present in the crystal lattice) created in ion cascades without any transformation of formed traps due to weakly overlapping subsequently formed cascades during the total irradiation procedure. The total defect (or trap) concentration should be lower than the initial doping concentration in order not to perturb the effective doping profile. The focused ion microbeams and IBIC technique are required in both phases of the experiment including i) the creation of patterned partly damaged areas covering the large range of implantation fluences and ii) the sensing of the deterioration of CCE due to created damage). Ions with different energy and mass provide agents and probes whose end of range can be tuned to the regions of interest which vary with the specific operating conditions of these devices. Another advantage of this methodology for assessment/evaluation of the radiation hardness in semiconductor materials is that the increase of dark current affecting device features is negligible, due to the smallness of the total damaged region compared to the whole active volume of the device. This is an important factor, which allows IBIC to be employed as the main characterization technique. Actually, IBIC technique (including Time Resolved IBIC [Breese2007] and HIQTS [Kada2015]) is the most suitable ion beam analysis technique for functional analysis of electronic materials, has solid theoretical foundations and can be easily implemented to any nuclear microprobe facility due to its operational simplicity.

The general model developed during the CRP integrates the Shockley-Read-Hall recombination model (section III.v   Modeling of radiation induced recombination mechanism) into the Shockley-Ramo-Gunn theory (section III.iii   Semiconductor device modelling: induced charge.). The model relies on the generation of recombination centres as the only effect induced by atomic displacements resulting from the interaction of the incoming ion and the atomic lattice. The resulting carrier lifetimes are connected to the ion fluence through eqs. (29) and (30), which entails a trap distribution proportional to the distribution of vacancies created initially by the radiation. Moreover, it is assumed that transport properties (i.e. carrier mobilities) and the effective doping concentration (and then the electric field) are not affected by ion irradiation (**Assumption V**).

The above-mentioned requirements define the condition of "low level of damage" we adopted in this work and the interpretative model can be effectively used only in this regime as well as in fully depletion conditions, i.e. when ionizing tracks of both PIBs and DIBs lie within the depletion region (**Assumption VIII**) .

The formulation of the model is general, and can in principle be adopted also in a case of partially depleted devices characterised with the limited depletion region and the neutral region in the bulk semiconductor material. In this case, an analytical general solution as reported in eq. (45) is no more available, but solutions of eqs. (38) can be calculated numerically. Therefore, the model can be extended also to cases of study in which the depletion region is shallower than the probing and damaging ion range. However, this case is not treated in this document, because it relies on more complex instrumentation and theoretical methods, (see [Vizkelethy2013] for a case when the damage is affecting the diffusion regime only). Actually, the mechanism of charge induction ascribable to diffusion of minority carriers is generally much slower than the drift component. This fact is the cause of ballistic deficit effects [Knoll2010], which can lead to a variable fraction of signal to be lost, if the amplifier shaping time is comparable with the rise time of the signal emerging from the preamplifier, and which can be mitigated using gated integrators, not often available in laboratory. Moreover, the rigorous modelling of the experiment requires the numerical solution of the time-dependent adjoint equations [Vittone2003], which is well beyond the scope of this report.

The methodology adopted to fit the experimental data with the theoretical curves proved to be effective to evaluate the two fitting parameters, namely the capture coefficients $\alpha_{n,p}$ (33), which provide the key parameters for the characterization of the effects of radiation damage in semiconductors. Actually, they depend on 1) the capture cross sections $\sigma_{n,p}$, which identify the nature of the recombination centres and 2) the factor $k_{n,p}$, which is the proportionality factor connecting the active recombination centres with the concentration of Frenkel pairs introduced as primary point defects. Moreover, if the intrinsic capture cross sections $\sigma_{n,p}$ are available, resulting from Deep Level Transient Spectroscopy (DLTS) [Lang1974] or similar techniques based on scanning ion beams [Kada2015, Laird1999], the $k_{n,p}$ factors can be evaluated, which represent the average number of active defects (carrier recombination centre) generated by a single vacancy.

For the case of study described in this report, assuming the $k_{n,p}$ factors independent on the type of the incoming particles [Leroy2007] and carrier thermal velocities values of v_n^{th}=2.05·10^7 cm/s and v_n^{th}=1.69·10^7 cm/s [Laird1999] the $k_{n,p}·\sigma_{n,p}$ products derived from eqs. (33) and (62) are $k_n·\sigma_n$ = 7.8·10^{-17}cm^2 and $k_p·\sigma_p$ = 4.8·10^{-16}cm^2 for electrons and holes, respectively. If a single acceptor state of divacancy is assumed to be the most abundant electronically active defect in the high purity and low doped n-type silicon created by ion irradiation [Pastuović2011], the capture cross sections are σ_n=5·10^{-15} cm^{-2} and σ_p=5·10^{-14} cm^{-2} [Vines2009], for electrons and holes, respectively. Therefore the relevant k-terms are k_n≈1.6·10^{-2} and k_p≈1.0·10^{-2}, i.e. about 60 and 100 radiation induced defects are required to form 1 stable electron and hole recombination centre, respectively.

However, as highlighted in [Vittone2016], these results are strongly dependent on the evaluation of the absolute vacancy profiles Vac(x). The commonly used SRIM [W5] software or more elaborated tools as MARLOWE [Robinson1974] are based on approximate algorithms (e.g. the Binary Collision Approximation), where the estimated vacancy profile is usually overestimated (i.e. the k·σ products underestimated).

However, these drawbacks do not invalidate the methodology. If we assume that SRIM provides realistic but un-normalized vacancy and ionization profiles, the capture coefficients extracted from the fitting procedure can be considered reference values, which can be used to compare the radiation hardness of different semiconductor materials or devices and to envisage the corresponding CCE degradation for any ion irradiation and polarization condition. An exhaustive connection of these parameters with the nature and the number of stable radiation induced defects require the use of more elaborate computational tools and experimental techniques and is beyond the scope of this report.

Actually, this document is intended as guidance to attain reliable measurements of the degradation of the CCE or any other electronic property of semiconductor devices, induced by displacement damage effects. The proposed methodology overcome the limits inherent in the commonly used NIEL approach, which can be inferred from a more general model in the case of constant damage profile, and contribute toward a standardized quantification of radiation hardness of semiconductor materials.

VI.   ACRONYMS

BCA	Binary Collision Approximation
CCE	Charge Collection Efficiency
CV	Capacitance-Voltage characterization
DIB	Damaging Ion Beam
DUS	Device under study
FP	Frenkel pairs
IBA	Ion Beam Analysis
IBIC	Ion Beam Induced Charge
NRA	Nuclear Reaction Analysis
PIB	Probing Ion Beam
PIXE	Particle Induced X-ray Emission
RBS	Rutherford Backscattering spectroscopy
SR	Spreading Resistance profiling technique
SRIM	Stopping Range of Ions in Matter (simulation tool [W5])
STIM	Scanning Transmission Ion Microscopy
TEM	Transmission Electron Microscopy

VII. LIST OF SYMBOLS

Symbol	Description	Symbol	Description
A	Area of the electrodes	M	average defect production energy deposited through atomic displacement [Messenger1999]
$\alpha_{n,p} = k_{n,p} \cdot \sigma_{n,p} \cdot v_{n,p}^{th}$	Electron (n) and hole (p) capture coefficient	$\mu_{n,p}$	Electron (n) and hole (p) mobility
C	capacitance	n_0	Thermal equilibrium electron density
CCE	Charge collection efficiency	n	Electron concentration
d	Length of the device	n^+	Adjoint electron concentration
D_d	Displacement damage dose	n_i	Intrinsic carrier concentration (in silicon $n_i = 1.5 \cdot 10^{-2}$ μm^{-3})
$\dfrac{dE_I}{dx}$	Specific ionization energy loss	N	Number of irradiated region (typically 9) at differenf fluences (see Figure II-13)
$D_{n,p} = k_B \cdot T \cdot \mu_{n,p}$	Electron (n) and hole (p) diffusivity	N_A	Ionized acceptor concentration
$\varepsilon = \varepsilon_r \cdot \varepsilon_0$	Permittivity	N_D	Ionized donor concentration
ε_r	Dielectric constant (or permittivity) : (in silicon 11.68)	N^T	Density of recombination centers
ε_0	Free space permittivity ($\approx 8,85$ pF/m)	p_0	Thermal equilibrium hole density
ε_{np}	Average energy dissipated by ionization radiation per electron-hole pair generation.	p	Hole concentration
$E = -\nabla\varphi$	Electric Field	p^+	Adjoint hole concentration
$E^+ = \dfrac{\partial E}{\partial V}$	Gunn's weighting Field	q	Elementary charge ($\approx 1,6 \cdot 10^{-19}$ C)
E_I	Ion energy	Q	Induced charge at the sensing electrode

$f_n = \Phi - \ln\left(\dfrac{n}{n_i}\right)$	Electron normalized quasi Fermi level	$\rho = q \cdot (N_D - N_A + p - n)$	Charge density
$f_n^+ = \dfrac{\partial f_n}{\partial V}$	Gunn's electron normalized quasi Fermi level	ρ_M	mass density
$f_p = \Phi + \ln\left(\dfrac{p}{n_i}\right)$	Hole normalized quasi Fermi level	R	Range of ions
$f_p^+ = \dfrac{\partial f_p}{\partial V}$	Gunn's hole normalized quasi Fermi level	$R_{n,p}$	Electron (n) and hole (p) recombination term in the continuity equation
φ	Electrostatic potential	$\sigma_{n,p}$	Electron (n) and hole (p) capture cross section
$\varphi^+ = \dfrac{\partial \varphi}{\partial V}$	Gunn's weighting potential	T	Temperature
$\varphi_N = \dfrac{q}{k_B \cdot T}\varphi = \dfrac{\varphi}{V_{th}}$	Normalized potential	$\tau_{n,p}$	Electron (n) and hole (p) lifetime
Φ	Ion fluence	$\tau_{0,n,p}$	Thermal equilibrium electron (n) and hole (p) lifetime
$\gamma = \dfrac{1}{E_I}\dfrac{dE_I}{dx}$	Normalized generation profile	V	Applied bias voltage
$\Gamma = \varepsilon_{np}\dfrac{dE_I}{dx}$	Electron-hole pairs generation profile	V_{bi}	Built-in potential
$G_{n,p}$	Electron (n) and hole (p) generation term in the continuity equation	$v_n = -\mu_n \cdot E$	Electron drift velocity
$G^+_n = v_n \cdot E^+$	Electron adjoint generation term	$v_p = +\mu_p \cdot E$	Electron drift velocity
$G^+_p = v_p \cdot E^+$	Hole adjoint generation term	Vac	Vacancy profile
$J_n = -q \cdot (v_n \cdot E \cdot n - D_n \cdot \nabla n)$	Electron current density	V_{Tot}	Total number of vacancies
$J_p = q \cdot (v_p \cdot E \cdot p - D_p \cdot \nabla p)$	Hole current density	$V_{th} = \dfrac{k_B \cdot T}{q}$	"Thermal potential" (at room temperature $\approx$ 26 mV)
k_B	Boltzmann constant ($\approx 1.38 \cdot 10^{-23}$ J/K)	$v_{n,p}^{th}$	Electron (n) and hole (p) thermal velocities

$k_{n,p}$	average number of active defects (carrier recombination center) generated by a single vacancy	w	Extension of the depletion layer
K_{ed}	Equivalent damage factor [Messenger1999]	$\Omega=[0,d]$	Integration domain of the continuity and Poisson's equations

VIII. ASSUMPTIONS

Assumption I (pag. 24):   Steady State Conditions

Assumption II (pag. 24):   Uni-dimensional domain

Assumption III (pag.24):   Polarization conditions

Assumption IV (pag.24):   Ohmic contacts

Assumption V (pag. 26):   The semiconductor operates in quasi steady-state mode. The excess charge produced by radiation interactions does not significantly perturb the field within the detector.

Assumption VI (pag. 26):   Linearization of the generation-recombination terms.

Assumption VII (pag. 32):   Shockley-Read-Hall model, see eq. (30)

Assumption VIII (pag. 35):   Fully depletion conditions

Assumption IX (pag. 36):   The pristine diode has 100% collection efficiency.

Assumption X (pag. 38):   Very Low level of damage: DIB fluence range in which the CCE degradation follows a linear trend

Assumption XI (pag. 40):   Constant vacancy profile.

IX. LIST OF FIGURES

X. LIST OF TABLES

XI. BIBLIOGRAPHY

[ASTM2006]   ASTM, F1892-06 Standard Guide for ionizing radiation (total dose) effects testing of semiconductor devices, ASTM Standards, ASTM International (http://www.astm.org), 2006.

[ASTM2007]   ASTM, E1854-07 Standard Practice for Ensuring Test Consistency in Neutron-Induced Displacement Damage of Electronic Parts, ASTM Standards, ASTM International (http://www.astm.org), 2007.

[Barbero2015]   N. Barbero, J. Forneris, V. Grilj, M. Jakšić, J. Räisänen, A. Simon, N. Skukan, E. Vittone, Degradation of the charge collection efficiency of an n-type Fz silicon diode subjected to MeV proton irradiation, Nucl. Instruments Methods Phys. Res. Sect. B Beam Interact. with Mater. Atoms. 348 (2015) 260–264. doi:10.1016/j.nimb.2014.11.019.

[Barrett1995]   H.H. Barrett, J.D. Eslkn, H.. Barber, Charge transport in arrays of semiconductor gamma ray detectors.pdf, (1995) 156–159.

[Bertolini1968] G. Bertolini, A. Coche, "Semiconductor Detectors", North-Holland, Amsterdam, 1968.

[Bogovac2009]   M. Bogovac, M. Jaksic, D. Wegrzynek, A. Markowicz, "Digital pulse processor for ion beam microprobe imaging", Nucl. Instruments Methods Phys. Res. Sect. B Beam Interact. with Mater. Atoms. 267 (2009) 2073–2076. doi:10.1016/j.nimb.2009.03.033.

[Brandt1978]   S: Brandt, "Statistical and computational methods in data analysis", 3rd edition, North Holland, Amsterdam 1978.

[Breese1993a]   M. B. H. Breese, "A theory of ion beam induced charge collection," J. Appl. Phys., vol. 74, no. 6, pp. 3789–3799, 1993.

[Breese1993b]   M. B. H. Breese, G. W. Grime, and F. Watt, "Study of nuclear microprobe beam halo using IBIC," Nucl. Instruments Methods Phys. Res. Sect. B Beam Interact. with Mater. Atoms, vol. 77, no. 1–4, pp. 243–246, 1993.

[Breese1996]   M. B. H. Breese, "A review of ion beam induced charge microscopy for integrated circuit analysis," Mater. Sci. Eng. 1, vol. B42, pp. 67–76, 1996.

[Breese1996a]   M.B.H. Breese, D.N. Jamieson, P. J.C. King, "Materials Analysis using a Nuclear Microprobe", John Wiley Sons, Inc. , 1996, ISBN 0-471-10608-9

[Breese2007]   M. B. H. Breese, E. Vittone, G. Vizkelethy, and P. J. Sellin, "A review of ion beam induced charge microscopy," Nucl. Instruments Methods Phys. Res. Sect. B Beam Interact. with Mater. Atoms, vol. 264, no. 2, pp. 345–360, 2007.

[Chih1991]   Chih-Tang Sah, "Fundamentals of Solid-State Electronics", World Scientific, Singapore 1991.

[COMSOL]   COMSOL: Multiphysics Modeling and Simulation, ver. 3.5. www.comsol.com.

[Corbett1965]   J.W. Corbett, G.D. Watkins, "Production of divacancies and vacancies by electron irradiation of silicon", Phys. Rev. 138 (1965). doi:10.1103/PhysRev.138.A555.

[CRP2016]   ''Papers arising from IAEA Coordinated Research Project ''Utilization of ion accelerators for studying and modelling of radiation induced defects in semiconductors and insulators'' (F11016)'', E. Vittone, M. Breese, A. Simon (Editors), Nuclear Instruments and Methods in Physics Research B 372 (2016) 127

[Doyle2000]   B.L. Doyle, G. Vizkelethy, and D.S. Walsh, "Ion beam induced charge collection (IBICC) studies of cadmium zinc telluride (CZT) radiation detectors." Nucl. Instruments Methods Phys. Res. Sect. B Beam Interact. with Mater. Atoms, vol. **161**: 457-461, (2000)

[Forneris2014] J. Forneris, M. Jaksic´, Z. Pastuovic´, E. Vittone, "A Monte Carlo software for the 1-dimensional simulation of IBIC experiments", Nucl. Instruments Methods Phys. Res. Sect. B Beam Interact. with Mater. Atoms, vol. 332 257-260(2014).

[Grilj2013]   V. Grilj, Natko Skukan, Milko Jaksic, Ettore Vittone, Technical Report of IAEA CRP F11016 on "Utilization of ion accelerators for studying and modeling of radiation induced defects in semiconductors and insulators" (22 april 2013).

[Grilj2016]   V. Grilj, N. Skukan, M. Jakšić, M. Pomorski, W. Kada, T. Kamiya, T. Ohshima, "The evaluation of radiation damage parameter for CVD diamond", Nucl. Instruments Methods Phys. Res. Sect. B Beam Interact. with Mater. Atoms., 372, 161-164 (2016)

[Groove1967]   A. S. Grove, "Physics and technology of semiconductor devices", Wiley, 1967, ISBN: 978-0-471-32998-5.

[Gunn1964]   J.B. Gunn, A general expression for electrostatic induction and its application to semiconductor devices, Solid State Electron (1964) 739–742.

[Jakob2011]   A. M. Jakob, D. Spemann, R. Thies, J. Barzola-Quiquia, J. Vogt, T. Butz, A characterisation of electronic properties of alkaline texturized polycrystalline silicon solar cells using IBIC, Nucl. Instruments Methods Phys. Res. Sect. B Beam Interact. with Mater. Atoms. 269 (2011) 2345–2349. doi:10.1016/j.nimb.2011.02.040.

[Kada2015]   W. Kada, Y. Kambayashi, N. Iwamoto, S. Onoda, T. Makino, M. Koka, T. Kamiya, N. Hoshino, H. Tsuchida, K. Kojima, O. Hanaizumi, T. Ohshima, "Development of diagnostic method for deep levels in semiconductors using charge induced by heavy ion microbeams", Nucl. Instruments Methods Phys. Res. Sect. B Beam Interact. with Mater. Atoms. 348 (2015) 240–245, http://dx.doi.org/10.1016/j.nimb.2014.12.054.

[Knoll2010]   G.F. Knoll, "Radiation Detection and Measurement", John Wiley & Sons Inc; 4th Ed. (2010), ISBN: 978-0470131480.

[Laird1999]   J.S. Laird, R.A. Bardos. C. Jagadish, D.N. Jamieson, G.J.F. Legge, Scanning ion deep level transient spectroscopy, Nucl. Instruments Methods Phys. Res. Sect. B Beam Interact. with Mater. Atoms. 158 (1999) 464–469, doi: 10.1016/S0168-583X(99)00329-8.

[Lang1974]   D.V. Lang, "Deep-level transient spectroscopy: a new method to characterize traps in semiconductors, J. Appl. Phys. 45 (1974) 3023–3032.

[Leroy2007]   C. Leroy, P.G. Rancoita, Particle interaction and displacement damage in silicon devices operated in radiation environments, Rep. Prog. Phys, 70 (2007), 493-625.

[LoGiudice2005] A. Lo Giudice, F. Fizzotti, C. Manfredotti, E. Vittone, F. Nava, "Average energy dissipated by mega-electron-volt hydrogen and helium ions per electron-hole pair generation in 4H-SiC", Applied Physics Letters 87, 222105 (2005).

[LoGiudice2006]   A. Lo Giudice, Y. Garino, C. Manfredotti, V. Rigato, E. Vittone "Angle resolved IBIC analysis of 4H-SiC Schottky diodes", Nuclear Instruments and Methods in Physics Research B 249 (2006) 213–216.

[Lopez2016]   J. Garcia Lopez, M. C. Jimenez-Ramos, M. Rodriguez-Ramos, J. Ceballos, F. Linez, J.Raisanen, "Comparative study by IBIC of Si and SiC diodes irradiated with high energy protons" Nucl. Instr. Meth. B 372 (2016) 143–150.

[Manfredotti2003] C. Manfredotti, F. Fizzotti, A. Lo Giudice, M. Jaksic, Z. Pastuovic, C. Paolini, P. Olivero, and E. Vittone, "Time-resolved ion beam-induced charge collection measurement of minority carrier lifetime in semiconductor power devices by using Gunn's theorem," Mater. Sci. Eng. B Solid-State Mater. Adv. Technol., vol. 102, no. 1–3, pp. 193–197, 2003.

[Martini1975]   M. Martini, T.W.Raudorf, W.R. Stott, J.C. Waddington, "Comparitive Ionization Energies for Protons, Deuterons and Alpha Particles in High Purity Germanium and Si(Li) Nuclear Radiation Detectors,", IEEE Transactions on Nuclear Science, 22, (1) (1975), 145-148. doi: 10.1109/TNS.1975.4327632

[Messenger1999] S. R. Messenger, E. a. Burke, G. P. Summers, M. a. Xapsos, R. J. Walters, E. M. Jackson, and B. D. Weaver, "Non Ionizing Energy Loss (NIEL) for Heavy Ions," IEEE Trans. Nucl. Sci., vol. 46, no. 9, pp. 1595–1602, 1999.

[Messenger2005] S.R. Messenger, E. Burke, R.J. Walters, J.H. Warner, G.P. Summers, "Using SRIM to calculate the relative damage coefficients for solar cells", Prog. Photovoltaics Res. Appl. 13 (2005) 115–123. doi:10.1002/pip.608.

[Moll2003]   M. Moll, "Development of radiation hard sensors for very high luminosity colliders-CERN-RD50 project", Nuclear Instruments and Methods in Physics Research A 511 (2003) 97-105.

[Pastuović2009] Z. Pastuović, M. Jakšić,G. Kalinka, M. Novak, A. Simon, "Deterioration of electrical and spectroscopic properties of a detector grade silicon photodiode exposed to focused ion beam irradiation", IEEE Trans. Nucl. Sci., vol. 56, pp. 2457-2464, 2009.

[Pastuović2011] Z. Pastuović, E. Vittone, I. Capan, and M. Jakšić, "Probability of divacancy trap production in silicon diodes exposed to focused ion beam irradiation," Appl. Phys. Lett., vol. 98, no. 9, pp. 2–4, 2011.

[Pastuović2013] Z. Pastuović, M. Jaksic, and E. Vittone, "Ion Beam Induced Charge analysis of radiation damage in silicon," MICRO- Nanotechnol. SENSORS, Syst. Appl. V, Proc. SPIE, vol. 8725, no. 1, p. 87251A, 2013.

[Pastuovic2015] Z. Pastuovic´, I. Capan, D. Cohen, J. Forneris, N. Iwamoto, T. Ohshima, R. Siegele, N. Hoshino, H. Tsuchida, "Radiation hardness of n-type SiC Schottky barrier diodes irradiated with MeV He ion microbeam", Nucl. Instruments Methods Phys. Res. Sect. B-Beam Interact. with Mater. Atoms. 348, 233–239 (2015)

[Pommé2015]   S. Pommé, B. Caro Marroyo, "Improved peak shape fitting in alpha spectra," Applied Radiation and Isotopes 96 (2015) 148–153.

[Prettyman1999a] T. H. Prettyman, "Method for mapping charge pulses in semiconductor radiation detectors," Nucl. Instruments Methods Phys. Res. Sect. A Accel. Spectrometers, Detect. Assoc. Equip., vol. 422, no. 1–3, pp. 232–237, 1999.

[Prettyman1999b] T. H. Prettyman, "Theoretical framework for mapping pulse shapes in semiconductor radiation detectors," Nucl. Instruments Methods Phys. Res. Sect. A Accel. Spectrometers, Detect. Assoc. Equip., vol. 428, no. 1, pp. 72–80, 1999.

[Ramo1938] S. Ramo, Currents-Induced-by-Electron-Motion, Proc. Of I.R.R. (1938) 584–585.

[Robinson1974] M.T. Robinson, I.M. Torrens, "Computer simulation of atomic-displacement cascades in solids in the binary-collision approximation", Phys. Rev. B 9 (1974), 5008–5024.

[Scharfetter1969] D.L. Scharfetter, H.K. Gummel, "Large Signal Analysis of a Silicon Read Diode Oscillator", IEEE Trans. Electron. Devices ED-16, 64-77, 1969.

[Schroder1990] D.K. Schroder, "Semiconductor Material and Device Characterization", John Wiley & Sons, Inc., New York, 1990, ISBN 0-471-51104-8

[Schwank2013] J. R. Schwank, M. R. Shaneyfelt, P. E. Dodd, "Radiation Hardness Assurance Testing of Microelectronic Devices and Integrated Circuits: Radiation Environments, Physical Mechanisms, and Foundations for Hardness Assurance", IEEE Transactions on Nuclear Science , 60, 2074-2100 (2013).

[Selberherr1984] S. Selbehrherr, "Analysis and Simulation of Semiconductor Devices", Springer_Verlag, Wien 1984, ISBN 978-3-7091-8752-4.

[Shockley1938] W. Shockley, Currents to conductors induced by a moving point charge.pdf, Journal of Applied Physics, (1938) 635–636.

[Shockley1952] W. Shockley and W. T. Read, "Statistics of the Recombination of Holes and Electrons," Phys. Rev., vol. 87, no. 46, pp. 835–842, 1952.

[Seitz1954] F. Seitz, "Color centers in Alkali Halide crystals II", Rev. Mod. Phys. 26, 7 (1954)

[Simon2005] A. Simon, G. Kalinka, Investigation of charge collection in a silicon PIN photodiode, Nucl. Instruments Methods Phys. Res. Sect. B-Beam Interact. with Mater. Atoms. 231 (2005) 507–512. doi:10.1016/j.nimb.2005.01.108.

[Spemann2011] D. Spemann, T. Reinert, J. Vogt, T. Andrea, N. Barapatre, R. Feder, A.M. Jakob, N. Liebing, C. Meinecke, F. Menzel, M. Rothermel, T. Butz, Materials analysis and modification at LIPSION – Present state and future developments, Nucl. Inst. Methods Phys. Res. B. 269 (2011) 2175–2179. doi:10.1016/j.nimb.2011.02.054.

[Stoller2013] R. E. Stoller, M. B. Toloczko, G. S. Was, a. G. Certain, S. Dwaraknath, and F. a. Garner, "On the use of SRIM for computing radiation damage exposure," Nucl. Instruments Methods Phys. Res. Sect. B Beam Interact. with Mater. Atoms, vol. 310, pp. 75–80, 2013.

[Summers1995] G.P. Summers, E. a. Burke, M. a. Xapsos, Displacement Damage Analogs to Ionizing Radiation Effects, Radiat. Meas. 24 (1995) 1–8.

[Vines2009] L. Vines, E.V. Monakhov, J. Jensen, A.Y. Kuznetsov, B.G. Svensson, "Effect of spatial defect distribution on the electrical behavior of prominent vacancy point defects in swift-ion

implanted Si", Phys. Rev. B – Condens. Matter Mater. Phys. 79 (2009) 1–9, http://dx.doi.org/10.1103/PhysRevB.79.075206.

[Vittone2003]   C. Manfredotti, F. Fizzotti, A. Lo Giudice, M. Jaksic, Z. Pastuovic, C. Paolini, P. Olivero, and E. Vittone, "Time-resolved ion beam-induced charge collection measurement of minority carrier lifetime in semiconductor power devices by using Gunn's theorem," Mater. Sci. Eng. B Solid-State Mater. Adv. Technol., vol. 102, no. 1–3, pp. 193–197, 2003.

[Vittone2004]   E. Vittone, "Theory of ion beam induced charge measurement in semiconductor devices based on the Gunn's theorem," Nucl. Instruments Methods Phys. Res. Sect. B Beam Interact. with Mater. Atoms, vol. 219–220, no. 1–4, pp. 1043–1050, 2004.

[Vittone2005]   E. Vittone, V. Rigato, P. Olivero, F. Nava, C. Manfredotti, A. Lo Giudice, Y. Garino, and F. Fizzotti, "Temperature dependent IBIC study of 4H-SiC Schottky diodes," Nucl. Instruments Methods Phys. Res. Sect. B Beam Interact. with Mater. Atoms, vol. 231, no. 1–4, pp. 491–496, 2005.

[Vittone2008]   E. Vittone, Z. Pastuović, P. Olivero, C. Manfredotti, M. Jaksic, A. Lo Giudice, F. Fizzotti, and E. Colombo, "Semiconductor characterization by scanning ion beam induced charge (IBIC) microscopy," Nucl. Instruments Methods Phys. Res. Sect. B Beam Interact. with Mater. Atoms, vol. 266, no. 8, pp. 1312–1318, 2008.

[Vittone2013]   E. Vittone, Semiconductor Characterization by Scanning Ion Beam Induced Charge (IBIC) Microscopy, ISRN Mater. Sci. 2013 (2013) 637608-.

[Vittone2016]   E. Vittone, Z. Pastuović, M. B. H. Breese, J. Garcia Lopez, M. Jaksic, J. Raisanen, R. Siegele, A. Simon, and G. Vizkelethy, "Charge collection efficiency degradation induced by MeV ions in semiconductor devices: Model and experiment," Nucl. Instruments Methods Phys. Res. Sect. B Beam Interact. with Mater. Atoms, vol. 372, pp. 128–142, 2016.

[Vizkelethy2009]   G. Vizkelethy, "Simulation of Ion Beam Induced Current in Radiation Detectors and Microelectronic Devices", SANDIA REPORT SAND2009-6759, October 2009
http://prod.sandia.gov/techlib/access-control.cgi/2009/096759.pdf

[Vizkelethy2011]   G. Vizkelethy, "Simulation of ion beam induced current in radiation detectors and microelectronic devices," Nucl. Instruments Methods Phys. Res. Sect. B Beam Interact. with Mater. Atoms, vol. 269, no. 20, pp. 2330–2335, 2011.

[Vizkelethy2013]   G. Vizkelethy, R. M. Fleming, and E. Bielejec, "Investigation of ion beam induced radiation damage in Si PN diodes," Nucl. Instruments Methods Phys. Res. Sect. B Beam Interact. with Mater. Atoms, vol. 306, pp. 176–180, 2013.

[Vizkelethy2016]   G. Vizkelethy, Contribution of the Sandia National Laboratory to the final report of CRP F11016

[Ziegler2010]   J. F. Ziegler, M. D. Ziegler, and J. P. Biersack, "SRIM - The stopping and range of ions in matter (2010)," Nucl. Instruments Methods Phys. Res. Sect. B Beam Interact. with Mater. Atoms, vol. 268, no. 11–12, pp. 1818–1823, 2010.

XII. WEBLIOGRAPHY

[W1]   Data sheet of the DUS1:
        http://www.hamamatsu.com/resources/pdf/ssd/s1223_series_kpin1050e.pdf

[W2]   ORTEC: Preamplifier introduction: http://www.ortec-online.com/download/Preamplifier-Introduction.pdf

[W3]   Hamamatsu, Solid State Division, Technical information SD-37: Characteristic and use of charge amplifier https://www.hamamatsu.com/resources/pdf/ssd/charge_amp_kacc9001e.pdf

[W4]   AMPTEK A250 preamplifier: http://amptek.com/products/a250-charge-sensitive-preamplifier/

[W5]   SRIM website: http://www.srim.org/

[W6]   NIST: Digital Library of Mathematical Functions: http://dlmf.nist.gov/

[W7]   ORTEC 572 Amplifier http://www.ortec-online.com/products/electronics/amplifiers/572a

[W8]   J. Forneris: "IBIC Simulation tool", http://www.solid.unito.it/RICERCA/IBA/IST.html

[W9]   CERN-RD50 "Radiation Hard Semiconductor Devices for Very High Luminosity Colliders",
        https://rd50.web.cern.ch/rd50/

[W10]   May Fawaz-Huber: "New Methodology Paves Way for Predicting the Lifetime of Electronic Devices Exposed to Radiation", https://www.iaea.org/newscenter/news/new-methodology-paves-way-for-predicting-the-lifetime-of-electronic-devices-exposed-to-radiation

[W11]   F. James, "Minuit, Function Minimization and Error Analysis", Computer and Networks division, CERN Geneva, Switzerland, http://inspirehep.net/record/1258343?ln=it

XIII. LIST OF CONTRIBUTORS

Zeljko PASTUOVIC, Rainer SIEGELE

Centre for Accelerator Science, Australian Nuclear Science and Technology Organization (ANSTO), Australia

Gyorgy VIZKELETHY

Sandia National Laboratories, Department of Ion-Solid Interactions, Albuquerque, USA

Sandia National Laboratories is a multi-mission laboratory managed and operated by National Technology and Engineering Solutions of Sandia, LLC., a wholly owned subsidiary of Honeywell International, Inc., for the U.S. Department of Energy's National Nuclear Security Administration under contract DE-NA0003525

Milko JAKSIC, Veljko GRILJ, Natko SKUKAN

Ruder Boskovic Institute, Zagreb, Croatia

Javier GARCIA LOPEZ, Carmen JIMENEZ RAMOS

Centro Nacional de Aceleradores, University of Sevilla, Spain

Ettore VITTONE

Physics Department of the University of Torino, Italy